Electronic structure and magnetic properties of strongly correlated materials: Development of a DFT + DMFT method

Dissertation

zur Erlangung des Doktorgrades

des Fachbereiches Physik
an der Fakultät für Mathematik, Informatik
und Naturwissenschaften
der Universität Hamburg

vorgelegt von

Oleg Kristanovski

Hamburg
2018

Gutachter der Dissertation:	Prof. Dr. Alexander Lichtenstein PD. Dr. Alexander Chudnovskiy
Zusammensetzung der Prüfungskommission:	Prof. Dr. Alexander Lichtenstein Prof. Dr. Michael Potthoff Prof. Dr. Daniela Pfannkuche Prof. Dr. Nils Huse PD. Dr. Alexander Chudnovskiy
Vorsitzende der Prüfungskommission:	Prof. Dr. Daniela Pfannkuche
Datum der Disputation:	12.12.2018
Vorsitzender Fach-Promotionsausschusses PHYSIK:	Prof. Dr. Michael Potthoff
Leiter des Fachbereichs PHYSIK:	Prof. Dr. Wolfgang Hansen
Dekan der Fakultät MIN:	Prof. Dr. Heinrich Graener

Kurzfassung

Diese Arbeit widmet sich einer theoretischen Untersuchung von Systemen mit stark korrelierten Elektronen mit Hilfe einer Methode, die dazu dient, eine ab initio Beschreibung unter der Berücksichtigung von Vielteilcheneffekte zu realisieren. Die Verbindung DFT + DMFT wurde in einer ladungsselbstkonsistenten Weise realisiert. Als Erstes untersuchen wir die Auswirkung der dynamischen Korrelationen auf die Energie- und Phasenstabilität von Fe_3Al, als auch auf die komplizierte Energielückenöffnung von der Fe_2VAl - Verbindung. Eine ladungsselbstkonsistente Version von DFT + DMFT ist wichtig, um die korrelierte Ladungsdichte und magnetische Energie richtig zu bekommen, damit eine bessere Charakterisierung und ein besseres Verständnis der Phasenstabilität von bcc - basiertem $DO_3 - Fe_3Al$ zu erreichen. Die errechnete DFT + DMFT - Spaltgröße und ihre Temperaturempfindlichkeit stimmen hervorragend mit den experimentellen Ergebnissen für Fe_2VAl überein.

In dieser Arbeit präsentieren wir auch eine detaillierte Vielteilchenuntersuchung der Wirkung von Sauerstoffleerstellen in Rutil - TiO_2, sowohl im unteren als auch im höheren Konzentrationsbereich.

Die verwendete Methode ist nicht trivial, insbesondere Probleme bestehen, die Doppelzählung vom Korrelationseffekten zu vermeiden. Die bereits im DFT - Hamilton - Operator enthaltenen Teile der Coulomb - Wechselwirkung (Hartree- and Austauschkorrelationsterme) müssen in dem DFT + DMFT - Schema approximativ korrigiert werden. Diese Doppelzählungskorrektur ergibt sich aus einer

sphärisch symmetrischen Behandlung. Der DFT - Teil der Hartree - und der Austauschkorrelationsenergien bleiben zusammen mit den nichtsphärischen Beiträgen in dem DFT + DMFT - Energiefunktional erhalten. Wir haben die Methode entwickelt, so dass diese nicht - sphärische Doppelzählung in DFT + DMFT ausgeschlossen werden können. Die dargestellte Methode wird für die Berechnung der Gesamtenergie und strukturellen Optimierung des Supraleiters LaFeAsO angewendet.

Abschließend motiviert durch eine neue Art des Tunnelmechanismus untersuchen wir die Temperatur- und Magnetfeldabhängigkeit der Magnonenspektren innerhalb der selbstkonsistenten Spinwellentheorie.

—

Abstract

This thesis is devoted to a theoretical investigation of systems containing strongly correlated electrons using a methodology for an ab initio description taking into account many - body effects. The combination DFT + DMFT was developed in a charge self - consistent manner. In the first part we study the impact of dynamical correlations on the energetics and phase stability of Fe_3Al, and on the intricate gap opening in Fe_2VAl. The charge self - consistency obtains special importance for the calculation of the correlated charge density and the magnetic energy to achieve a better characterization and understanding of the phase stability of bcc - based $DO_3 - Fe_3Al$. The DFT + DMFT gap size and its sensitivity to temperature are in excellent agreement with experimental results for Fe_2VAl compound.

We also present a detailed many - body study of the effect of oxygen vacancies in rutile - TiO_2, both in the lower and in the higher concentration range.

The presented method is nontrivial; problems exsist to avoid double - counting of correlation effects. The parts of the Coulomb interaction already contained in the DFT - Hamiltonian have to be corrected approximative in the DFT + DMFT scheme. This double - counting correction results from a spherically symmetric treatment, but the DFT part of the Hartree and the exchange - correlation energies remain accounted together with the nonspherical contributions into the DFT + DMFT energy functional. We developed the method so that the nonspherical contributions of the double - counting could be re-

moved in the DFT+ DMFT total - energy charge self - consistent calculations. The presented method was applied for the calculation of the total energy and structural optimization of the superconductor LaFeAsO.

Finally, motivated by the new type of tunneling mechanism in recent experiments, we test the temperature and magnetic field dependence of the magnon spectra within the self - consistent spin - wave theory.

—

Contents

One

Preface

The subject of the work is devoted to a theoretical study of electronic structure and magnetism of real systems exhibiting electronic correlation effects using DFT - based methods. Physical systems with strong correlations correspond to ensemble of the valence electrons, which cannot be described as independent particles. There are a lot of important materials with strong interactions between the particles, and these interactions play a crucial role in determining the properties of such systems. Strongly correlated real materials are represented by solid state systems containing atoms with open d- or f- shells. A lot of observed effects are characteristic for considered systems. The most famous of these is the high - temperature superconductivity in cuprates [BM86]. Most of the modern magnetic materials have strong electronic correlations, since the presence of an uncompensated magnetic moment in them is due to the incomplete filling of the valence shell in the transition metals. It is thus of interest to many fields of science to understand the fundamental forces and interactions governing the behavior of such systems. The magnetic and electronic properties tend to be complicated to describe theoretically. The density functional theory (DFT) is the most successful and prominent approach to compute the electronic structure of matter. The density functional theory regards the electron density as the central variable, instead of the many - body wavefunction. DFT could reproduce to an astounding accuracy the electronic properties of weakly correlated systems, such as simple metals, semiconductors, or band insulating materials,

but not applicable to systems with strongly electronic correlations. DFT cannot describe the physical behavior of such systems, which is caused by the localization of electrons. There are a lot of examples of transition metal systems like NiO, that are experimentally an insulator, but is predicted to be a metal by DFT. Electronic correlations are not only relevant for strongly correlated oxides but do matter also for intermetallic compounds like Fe - Al, which are hard to describe in conventional DFT, as shown in various relevant publications. With a new combination of the local density approximation and dynamical mean field theory (LDA + DMFT) one now tries to investigate more rigorously the effects of correlations. We use DFT to parametrize a Hubbard Hamiltonian and solve it with DMFT (details in section 2). In chapter 3 we perform a realistic many - body study based on DFT + DMFT in a charge self - consistent manner. We show the important impact of many - body effects on the electronic structure in two intermetallic systems, namely Fe_3Al and Fe_2VAl. An enhanced representation of the correlated charge density and the magnetic energy was achieved, so that the phase stability of bcc - based $DO_3 - Fe_3Al$ could be better characterized and understood. For the realization of the Heusler compound Fe_2VAl one of the Fe sublattice was substitute with V. Conventional DFT based on LDA/GGA characterize Fe_2VAl as a non - magnetic semimetallic [SM98, WP98]. Improving on the exchange part in DFT, Fe_2VAl becomes a semiconductor. The size of this gap varies wildly in size depending on which functional and which admixture parameter is used. For Fe_2VAl we found a strongly renormalized pseudogap, which size and its sensitivity to temperature are in excellent agreement with experimental results for this compound.

The rutile - based TiO_2 and the Ti_3O_5 magneli phase will be studied in chapter 4. We go beyond conventional DFT/DFT + U studies to investigate the physics of oxygen vacancies in rutile - based TiO_2. This sheds new light on the electron states in this compound and provides excellent agreement with experiment, e.g. concerning the deep - level positioning. In addition, we also address the correlation physics of the related Magneli phase, to our knowledge the first examination

with DFT + DMFT methods. The work is an important contribution to the research on transition - metal oxides. Rendering it obvious that also band - insulating oxides, and here first from the rutile - structure group, are potential candidates for strong correlation physics. This pushes the limits of materials science research in favor of first - principles many - body methods.

By combining the DFT with the DMFT, there are problems with extracting a suitable correlated subspace from the DFT calculation, and also to avoid double counting of correlation effects. In chapter 5 we developed a sheme to avoid a problem of nonspherical double - counting in DFT + DMFT. Using this scheme calculations of the total energy and structural optimization of the pnictide superconductor LaFeAsO were performed. The results are compared to a recently proposed "exact" double - counting formulation. We have shown that both the double - counting free schemes give the similar results.

Finally we report a new type of tunneling mechanism in van der Waals heterostructures by demonstrating that electrons in our device tunnel between graphene layers via the emission of magnons in the $CrBr_3$ barrier. The electron tunneling has been investigated experimentally and theoretically. We show the computed density of magnon states in $CrBr_3$, on the basis of experimentally determined exchange parameters. Announced inelastic neutron scattering investigations of magnons in $CrBr_3$ are in a good agreement with calculated results.

Two

Theoretical framework

2.1 DFT+DMFT for strongly correlated real Materials

We begin with the description of the DFT+DMFT approach [APK+97a,LK98] that will be used to investigate correlated real materials. It will be noted that the full many - body Hamiltonian describes the interacting electrons in the external potential comprised of an ionic lattice and their interactions. This many - body Hamiltonian is calculated using the following formula

$$H = \sum_{\sigma} \int \mathrm{d}\mathbf{r}\, \hat{\psi}^{+}_{\sigma}(\mathbf{r})[-\frac{1}{2}\Delta + V_{\mathrm{ext}}(\mathbf{r}) - \mu]\hat{\psi}_{\sigma}(\mathbf{r}) + \frac{1}{2}\sum_{\sigma\sigma'} \int d\mathbf{r} \int d\mathbf{r}')\, \hat{\psi}^{+}_{\sigma}(\mathbf{r}')\hat{\psi}^{+}_{\sigma'}(\mathbf{r}')U(\mathbf{r}-\mathbf{r}')\hat{\psi}_{\sigma}(\mathbf{r}')\hat{\psi}_{\sigma'}(\mathbf{r}), \qquad (2.1)$$

where, $V_{\mathrm{ext}}(\mathbf{r})$ is the external ionic potential and μ the chemical potential, and the electrons interact via the Coulomb law: $U(\mathbf{r}-\mathbf{r}') = 1/|\mathbf{r}-\mathbf{r}'|$. The natural atomic units are used, where $\hbar = e = m = 1$.

The electronic system is described by the the density functional theory (DFT). DFT is one of the most successful methods for the characterization of the electronic properties of weakly correlated systems. The main idea of DFT is that the full electronic density is the

basic quantity in describing the ground - state of an interacting system of fermions. The ground - state total energy of the ineracting electron system is a functional of electronic density. The ground - state determination of the electronic many - body system is based on the minimization of the total - energy functional with respect to this quantity. The Hohenberg - Kohn (HK) theorems prove the existence of such functional. Kohn - Sham equations are a particullary implementation of this theorems in order to calculate physical properties of different systems. In these equations, there is an effective potential which contains different terms. In the KS potential, the whole many - body effects are incorporated into a functional of density, known as the exchange - correlation functional. We briefly present the most important equations and approximations that are used in DFT. We start with the Hamiltonian of the system of interacting electrons that is subject to an external potential

$$\hat{H} = \hat{T} + \hat{V}_{ee} + \hat{V}_{ext}, \tag{2.2}$$

where $\hat{T}$ is the kinetic energy, $\hat{V}_{ee}$ is the electron - electron interaction, and $\hat{V}_{ext}$ is the external potential.

Hohenberg and Kohn [HK64] suggested that in the ground state of the system the only the electronic - density of the ground state is necessary. It can be also connected to the external potential acting on the interacting system. This idea leads to two theorems. In short, the first theorem says that the external potential is uniquely determined by the ground - state electron - density $\rho_0(\boldsymbol{r})$. Thus, we can now rewrite the ground - state total energy as functional of $\rho(\mathbf{r})$

$$\begin{aligned} E[\rho(\mathbf{r})] &= T[\rho(\mathbf{r})] + V_{ee}[\rho(\mathbf{r})] + V_{ext}[\rho(\mathbf{r})] \\ &= F[\rho(\mathbf{r})] + \int d\mathbf{r}\nu_{ext}(\mathbf{r})\rho(\mathbf{r}). \end{aligned} \tag{2.3}$$

Here, the universal functional $F[\rho(\mathbf{r})]$ contains the kinetic and potential contribution of electrons.

The second HK theorem gives the energy variation principle to find the ground - state. $E[\rho(\mathbf{r})]$ reaches its minimal value of the ground state energy when $\rho = \rho_0$. It means that the ground - state energy is obtained when the ground - state electron - density is introduced into the energy functional. It should be found the minimum of the following functional,

$$E[\rho(\mathbf{r})] - \mu\bigg(\int \rho(\mathbf{r})d\mathbf{r} - N_e\bigg), \tag{2.4}$$

where μ is the Lagrange multiplier, and N_e is the total number of electrons. The variational principle is given by

$$\frac{\delta E[\rho(\mathbf{r})]}{\delta\rho(\mathbf{r})} = \frac{\delta F[\rho(\mathbf{r})]}{\delta\rho(\mathbf{r})} + \nu_{ext}(\mathbf{r}) = \mu \tag{2.5}$$

The many - body problem is reduced to finding a functional energy in terms of the electron - density, and solving the corresponding variational problem. Kohn and Sham provided the practically determination of the ground state density. The Kohn - Sham [KS65] approach replaced the interacting many - body system with a related but fictitious non - interacting electron system. The simplified system can be solved more easily. We can write the equation for this system as

$$[-\frac{1}{2}\nabla^2_{\mathbf{r}} + V_{KS}(\mathbf{r})]\phi_i(\mathbf{r}) = \epsilon_i\phi_i(\mathbf{r}), \tag{2.6}$$

where $V_{KS}(\mathbf{r})$ is the Kohn - Sham potential. The density can be calculated as

$$\rho(\mathbf{r}) = \sum_{i=1}^{N} |\phi(\mathbf{r})|^2. \tag{2.7}$$

The kinetic energy for the system of a non - ineracting electron gas can be evaluated as

$$T_s[\rho(\mathbf{r})] = \sum_{i=1}^{N} \int d\mathbf{r}\phi_i^*(\mathbf{r})[-\frac{1}{2}\nabla^2_{\mathbf{r}}]\phi_i(\mathbf{r}). \tag{2.8}$$

The total energy functional for this system is

$$E[\rho(\mathbf{r})] = T_s[\rho(\mathbf{r})] + \int d\mathbf{r} V_{KS}(\mathbf{r})\rho(\mathbf{r}). \tag{2.9}$$

The evaluable kinetic energy of the auxiliary system and the kinetic energy of the interacting system are different. Therefore, we introduce an exchange - correlation term

$$E_{XC}[\rho(\mathbf{r})] = (T[\rho(\mathbf{r})] - T_s[\rho(\mathbf{r})]) + (< \hat{V}_{ee} > - E_H[\rho(\mathbf{r})]), \tag{2.10}$$

which contains the kinetic energy difference and the general electron - electron interaction reduced by the classical electron repulsion, the Hartree energy. If we apply now the variational principle to the following energy functional

$$E[\rho(\mathbf{r})] = T_s[\rho(\mathbf{r})] + E_H[\rho(\mathbf{r})] + \int d\mathbf{r} \nu_{ext}(\mathbf{r})\rho(\mathbf{r}) + E_{XC}[\rho(\mathbf{r})], \tag{2.11}$$

we get the following:

$$\frac{\delta T_s[\rho(\mathbf{r})]}{\delta\rho(\mathbf{r})} + \nu_{ext}(\mathbf{r}) + \frac{1}{2}\int\int d\mathbf{r}' \frac{\rho(\mathbf{r}')}{|\mathbf{r} - \mathbf{r}'|} + V_{XC}(\mathbf{r}) = \mu, \tag{2.12}$$

in which $V_{XC}(\mathbf{r})=\frac{\delta E_{XC}[\rho(\mathbf{r})]}{\delta\rho(\mathbf{r})}$ is the exchange - correlation potential. Similar we can find

$$\frac{\delta T_s[\rho(\mathbf{r})]}{\delta\rho(\mathbf{r})} + V_{KS}(\mathbf{r}) = \mu. \tag{2.13}$$

If we compare both, equation (2.12) and equation (2.13), we get for the Kohn - Sham potential

$$V_{KS}(\mathbf{r}) = \nu_{ext}(\mathbf{r}) + V_H(\mathbf{r}) + V_{XC}(\mathbf{r}). \tag{2.14}$$

Now we can rewrite equation (2.6) as

$$[-\frac{1}{2}\nabla^2_{\mathbf{r}} + \nu_{ext}(\mathbf{r}) + V_H(\mathbf{r}) + V_{XC}(\mathbf{r})]\phi_i(\mathbf{r}) = \epsilon_i\phi_i(\mathbf{r}) \tag{2.15}$$

This is exactly the Kohn - Sham equation.

In particular, many applications use successfully the local - density approximation (LDA). The LDA used exact QMC results for interacting homogeneous electron gas (HEG) [CA80] to express exchange - correlation energy E_{XC} via ϵ_{XC} of HEG:

$$E_{XC}[\rho] = \int d^3\mathbf{r}\rho(\mathbf{r})\epsilon_{XC}[\rho(\mathbf{r})], \tag{2.16}$$

and finally:

$$V_{XC}(\mathbf{r}) = \frac{\delta E_{XC}}{\delta\rho(\mathbf{r})}. \tag{2.17}$$

As shown above, from the Hohenberg - Kohn theorems follows that the Kohn - Sham potential bases on the electronic density itself, and after a self - consistent solution of the Schrödinger equation, the band dispersions $\varepsilon_n(\mathbf{k})$ appear. The most important problem is, how the inerface between DFT and the Hubbard model looks like. A suitable correlated subspace C starting from the complete Hilbert space of Bloch Kohn - Sham band states should be extracted. The Kohn - Sham Hamilton operator has to be expressed in a suitable basis set. From the Bloch Green's function $G_n^{\mathrm{B}}(\mathbf{k}, i\omega) = [i\omega - \varepsilon_n(\mathbf{k})]^{-1}$ one obtains the local Green's function using the projectors onto localized Wannier states related to the correlated material sites,

$$\begin{aligned} G_{\alpha\beta}(i\omega) &= \sum_{\mathbf{k}n} \mathcal{P}_{\alpha n}(\mathbf{k}) G_n^{\mathrm{B}}(\mathbf{k}, i\omega) \mathcal{P}^{+}_{\beta n}(\mathbf{k}) \\ &= [i\omega - \varepsilon - \Delta(i\omega)]^{-1}_{\alpha\beta}, \end{aligned} \tag{2.18}$$

where, α,β are spin - orbital indices, [α=(m,σ)], $\varepsilon_{\alpha\beta}$ is the on - site crystal - field matrix, and $\Delta_{\alpha\beta}(i\omega)$ the hybridization function. Both are defined on the correlated local orbitals and indexed by Greek labels. The choice of a localized basis set for realistic systems is in principle arbitrary and depended on the basis of the DFT code (i.e. maximally localized Wannier functions for "Wien2k" [BSM$^+$01], and projections onto localised orbitals for "Mixed - basis pseudopotential" (MBPP) [MELFed]). In the context of DFT + DMFT many

choices of a localized basis have been developed, like linear muffin - tin orbitals (LMTO) [APK+97b, LK98, SKA01], N - th order muffin - tin orbitals (NMTO) [PBP+04], Wannier functions constructed by a projection onto a subset of Bloch wave functions [AKK+05, KRPS02], maximally localized Wannier functions [LGP+06] or projection onto local orbitals in the full - potential linear augmented plane - wave (FLAPW) method [APV+09, ALG+08].

In the next sections we will present two basis sets that are used in this work.

Written in Grassmann variables c_α, c_α^*, the action for the resulting multi - orbital Anderson impurity model (AIM) on the imaginary - time axis is given by

$$\begin{aligned}\mathcal{S} &= \mathcal{S}_{\text{loc}} + \mathcal{S}_{\text{hyb}} \\ &= \int_0^\beta \mathrm{d}\tau H_{\text{loc}}(\tau) + \int_0^\beta \mathrm{d}\tau \int_0^\beta \mathrm{d}\tau' \sum_{\alpha\beta} c_\alpha^*(\tau)\Delta_{\alpha\beta}(\tau-\tau')c_\beta(\tau')\end{aligned} \tag{2.19}$$

$$H_{\text{loc}} = \sum_{\alpha\beta} \varepsilon_{\alpha\beta} c_\alpha^* c_\beta + \frac{1}{2}\sum_{\alpha\beta\gamma\delta} U_{\alpha\beta\gamma\delta} c_\alpha^* c_\beta^* c_\delta c_\gamma. \tag{2.20}$$

The most used formalism for an *ab - initio* determination of the Coulomb interaction parameters is the constrained random phase approximation (cRPA) [imcmcieifbuFB11] which considers that the effective interaction between the correlated electrons is the bare interaction screened by all the non - correlated electrons. The cRPA is part of the so - called GW approximation [vSKF06] introduced first by Hedin [Hed65] which treats the self - energy term in a diagrammatic expansion of the Hubbard model approximately in a self - consistent way. The name "GW" comes from the Green's function (G) and the screened interaction line (W).

For the solution of an AIM a many - body quantum Monte-Carlo (QMC) calculation can be performed, for which an efficient implementation of the continuous time hybridization expansion (CTHYB)

algorithm [Gul08] within the TRIQS/CTHYB collaboration [PFA+15, SKFP16] has been established. It corresponds to the DMFT without self - consistency, and refers to the situation of a correlated adatom embedded in a bath of non - interacting electrons, i.e. a surface system. To describe a bulk material, the AIM is used in a self - consistency loop. Let us have a look at the particular steps:

1. Having determined the DFT Hamiltonian $H^{\mathrm{DFT}}(\mathbf{k})$, we start the iteration with calculating the local Green's function in the Wannier basis by

$$G^{loc}_{mm'\sigma\sigma'}(i\omega_n) = \frac{1}{N_{\mathbf{k}}} \sum_{\mathbf{k}} \left[\frac{1}{(i\omega_n + \mu)\mathbb{I} - H^{\mathrm{DFT}}_{\mathbf{k}} + H^{\mathrm{DC}} - \Sigma(i\omega_n)} \right]^{\sigma\sigma'}_{mm'} \tag{2.21}$$

   Here, the sum runs over the $N_{\mathbf{k}}$ points first Brillouin zone, $H^{DFT}_{\mathbf{k}}$ is the DFT Hamiltonian, in the general form expressed as

$$H^{\mathrm{DFT}}_{\mathbf{k}} = \sum_{ij,mn} \sum_{\sigma\sigma'} t^{ij}_{m\sigma,n\sigma'} \hat{c}^{+}_{im\sigma} \hat{c}_{jn\sigma'} = \sum_{\mathbf{k},mn} \sum_{\sigma\sigma'} \epsilon_{m\sigma,n\sigma'}(\mathbf{k}) \hat{c}^{+}_{\mathbf{k}m\sigma} \hat{c}_{\mathbf{k}n\sigma'}, \tag{2.22}$$

   and the H^{DC} is the double - counting correction which subtracts from the DFT Hamiltonian the Coulomb effects already contained in $H^{\mathrm{DFT}}(\mathbf{k})$. The self - energy $\Sigma(i\omega_n)$, which is $\mathbf{k}$-independent in the DMFT approximation and set to zero in the first iteration.

2. Calculate the bath Green's function $\mathcal{G}(i\omega_n)$ from the local Dyson equation

$$(\mathcal{G}_0^{-1})^{\sigma\sigma'}_{mm'}(i\omega_n) = (G^{-1}_{loc})^{\sigma\sigma'}_{mm'}(i\omega_n) + \Sigma^{\sigma\sigma'}_{mm'}(i\omega_n). \tag{2.23}$$

3. Solve the effective impurity problem given by

$$\mathcal{S} = -\int_0^\beta d\tau \int_0^\beta d\tau' \sum_{mm'} \sum_{\sigma\sigma'} c^*_{m\sigma}(\tau)[\mathcal{G}_0^{-1}(\tau-\tau')]^{\sigma\sigma'}_{mm'} c_{m'\sigma'}(\tau') + \frac{1}{2}\int_0^\beta \mathrm{d}\tau \sum_{\substack{mm'\\m''m'''}} \sum_{\sigma\sigma'} U_{mm'm''m'''}\, c^*_{m\sigma}(\tau) c^*_{m'\sigma'}(\tau) c_{m'''\sigma'}(\tau) c_{m''\sigma}(\tau). \tag{2.24}$$

i. e. calculate its one - particle Green's function $G(i\omega_n)$. The action here corresponds to the one in Eq. equation (2.19).

4. Using the Dyson equation once again, obtain a new local self - energy $\Sigma(i\omega_n)$ from the just calculated Green's function $G(i\omega_n)$ and the bath Green's function $\mathcal{G}(i\omega_n)$. Continue with step 1 using the new self - energy.

These steps are iterated until self - consistency in the Green's function or the self - energy is reached. The self - consistency loop in the DFT + DMFT approach can be extended to include the electronic charge density $\rho(\mathbf{r})$. In such a charge self - consistent calculation, only one or a few iterations are performed per DMFT calculation. Then, the resulting charge density $\rho(\mathbf{r})$ is used as a starting point for a new DFT calculation, performing only one or a few of iterations to obtain a new DFT Hamiltonian, which serves as starting point for a new DMFT calculation. Those steps are iterated until self - consistency in both the self - energy and the charge density are reached. In practice, however, most applications of the DFT + DMFT method, so far, are restricted to calculations obtaining self - consistency only in the self - energy. An implementation of the full charge self - consistency is realized within TRIQS/DFT Tools which provides an interface between several DFT codes and the TRIQS/CTHYB code [APS+16].

Full charge self - consistency

As mentioned above, the self - consistency loop in the DFT + DMFT approach can be extended to include the electronic charge density $\rho(\mathbf{r})$. The charge - consistency is especially important for total energy calculations because the modified charge and one - electron potentials due to correlations will also effect the electron - nuclei and exchange - correlation energy, that also contribute to the total DFT + DMFT energy.

Here we will briefly describe this scheme in a standard way, following the outline of Ref. [APS+16, PABG07]. For further details of the implementation in specific basis set used in this work we refer to Ref. [Gri13].

For the charge density from a post - processing DMFT calculation we can write the DFT + DMFT density matrix for all bands ν,ν' in the energy window $\mathcal{W}$ for projection on the local orbitals as

$$N_{\nu\nu'}^{(\boldsymbol{k})} = \lim_{\tau \to 0^-} \frac{1}{\beta} \sum_{i\omega_n} G_{\nu\nu'}(\mathbf{k}, \mathbf{i}\omega_\mathbf{n}) e^{-i\omega_n \tau}. \tag{2.25}$$

In real space the full charge density matrix including additionally the bands outside the energy window $\mathcal{W}$ is given by

$$\rho^{DMFT}(\mathbf{r}) = \rho^{OW}(\mathbf{r}) + \sum_{\mathbf{k},\nu\nu'} < \mathbf{r}|\Psi_{\mathbf{k}\nu} > N_{\nu\nu'}^{(\boldsymbol{k})} < \Psi_{\mathbf{k}\nu'}|\mathbf{r} > . \tag{2.26}$$

Here, $\rho^{OW}(\mathbf{r})$ (OW=outside window) is the contribution of the states outside the window $\mathcal{W}$. Depending on the basis of the DFT code, one inserts the expansion of the Bloch wave function $< \mathbf{r}|\Psi_{\mathbf{k}\nu} >$ into Eq. 2.26 to obtain an expression for the charge density in the corresponding basis.

The representation of the total energy functional in the Bloch basis, in which the kinetic Hamilton operator consists of the diagonal matrix

of Kohn - Sham energy eigenvalues $\epsilon_{\boldsymbol{k}}$, can be written as [Gri13]

$$\begin{aligned} E^{DFT+DMFT} &= \sum_{\boldsymbol{k}} \sum_{\nu\nu'} \epsilon_{\boldsymbol{k}\nu} \delta_{\nu\nu'} n^B_{\boldsymbol{k}\nu\nu'} \\ &- \int d^3r (V_{KS}(\boldsymbol{r}) - \nu_{ext}(\boldsymbol{r})) \rho^{DMFT}(\boldsymbol{r}) \\ &+ E_H[\rho^{DMFT}(\boldsymbol{r})] + E_{XC}[\rho^{DMFT}(\boldsymbol{r})] \\ &+ < \hat{H}^{int} > - E_{dc}, \end{aligned} \tag{2.27}$$

where the first four terms are the estimation of the standard DFT functional at the self - consistently determined charge density. In a practical implementation, the total energy of the charge self - consistent DFT + DMFT reads [Gri13, PABG07, DMC+09],

$$\begin{aligned} E^{DFT+DMFT} &= E^{DFT}[\rho^{DMFT}(\boldsymbol{r})] \\ &+ \sum_{\boldsymbol{k}} \sum_{\nu} \epsilon_{\boldsymbol{k}\nu} \Delta N^{(\boldsymbol{k})}_{\nu\nu} + \langle \hat{H}_{int} \rangle - E_{dc} \, . \end{aligned} \tag{2.28}$$

where E^{DFT} is a standard DFT functional acting on the DMFT charge density ρ^{DMFT}, $\epsilon_{\boldsymbol{k}\nu}$ are the Kohn - Sham (KS) energy eigenvalues, $\Delta N^{(\boldsymbol{k})}$ is the KS occupation matrix correction due to the DMFT self - energy [LGP+06]. $< \hat{H}^{int} >$ is an expectation value of the Coulomb vertex, using the Galitskii - Migdal formula [GM58] it can be written as (in [FW71] is the complete derivation)

$$< \hat{H}^{int} > = \frac{1}{2} \sum_{n} Tr[\Sigma^{imp}_n(i\omega_n) \cdot G^{imp}_n(i\omega_n)]. \tag{2.29}$$

The other equivalent formulation thereof in Bloch space is possible because the trace operator is invariant under cyclic permutations, even for matrices that are not quadratic. It can be written as

$$
\begin{aligned}
< \hat{H}^{int} > &= \frac{1}{2} \sum_{\mathbf{k}n} Tr[\Sigma_n^{imp}(i\omega_n) \cdot \mathcal{P}_n(\mathbf{k}) G_n^{\mathrm{B}}(\mathbf{k}, i\omega) \mathcal{P}_n^{+}(\mathbf{k})] \\
&= \frac{1}{2} \sum_{\mathbf{k}n} Tr[\mathcal{P}_n^{+}(\mathbf{k}) \Sigma_n^{imp}(i\omega_n) \mathcal{P}_n(\mathbf{k}) \cdot G_n^{\mathrm{B}}(\mathbf{k}, i\omega)] \\
&= \frac{1}{2} \sum_{\mathbf{k}n} Tr[\Sigma_n^{\mathrm{B}}(i\omega_n) \cdot G_n^{\mathrm{B}}(\mathbf{k}, i\omega)] \qquad (2.30)
\end{aligned}
$$

In addition to the Galitskii - Migdal formula, there are other techniques for estimating this expectation value. Particularly in the quantum Monte - Carlo technique,which is used in this work, one can measure expectation values of operators directly in the Monte - Carlo process.

Finally, E_{dc} marks the double - counting correction. Eq. 2.28 assumes the use of the Bloch basis in which the kinetic energy operator is diagonal in a basis of the Kohn - Sham eigenstates.

2.2 Projections onto localised orbitals

The method of projection onto local orbitals as proposed by Amadon et al. [ALG+08] is based on the projection of the Bloch wave functions and the Green's function from the Bloch basis onto localized functions $|\chi_{\mathbf{T}m} >$ in the "correlated subspace" at the lattice vector $\mathbf{T}$, or the Bloch transform $|\chi_{\mathbf{k}m} >$ thereof. The index m is a atomic index. But if we express the Hamilton operator in the basis $|B_{\mathbf{k}\alpha} >$, where α is a spin - orbital index, then the main quantity of DMFT (local Green's function) could be rewritten as follows [LGP+06]

$$G^{loc}_{mm'}(i\omega_n) = \sum_{\mathbf{k}} \sum_{\alpha\beta} < \chi_{\mathbf{k}m}|B_{\mathbf{k}\alpha} >< B_{\mathbf{k}\beta}|\chi_{\mathbf{k}m'} > \cdot \left([(i\omega_n + \mu)\mathbb{I} - H^{kin}(\mathbf{k}) - \Delta\Sigma(\mathbf{k}, i\omega_n)]^{-1} \right)_{\alpha\beta}. \quad (2.31)$$

Here, $\Delta\Sigma(\mathbf{k}, i\omega_n)$ can be unfolded from the impurity self energy $\Sigma^{imp}(i\omega_n)$ as follows:

$$\Delta\Sigma_{\alpha\beta}(\mathbf{k}, i\omega_n) = \sum_{mm'} < B_{\mathbf{k}\alpha}|\chi_{\mathbf{k}m} > \left[\Sigma^{imp}_{mm'}(i\omega_n) - \Sigma^{dc}_{mm'} \right] < \chi_{\mathbf{k}m'}|B_{\mathbf{k}\beta} >, \quad (2.32)$$

where Σ^{dc} is the double - counting correction, which we will discusse in detail in the next section. In this projection scheme, the choice of a subset $\mathcal{W}$ of the original Bloch wave functions $|\psi_{n\mathbf{k}} >$ leads to the fact that the kinetic part of the Hamiltonian operator becomes diagonal:

$$H^{kin}_{\nu\nu'}(\mathbf{k}) = \epsilon_{\mathbf{k}\nu}\delta_{\nu\nu'}. \quad (2.33)$$

Here, $\epsilon_{\mathbf{k}\nu}$ are the Kohn - Sham energy eigenvalues. As mentioned above, $|\chi_{\mathbf{k}m} >$ define the basis of the "correlated subspace". We can determine elements of the projection matrix that occur in equation (2.31) as follows:

$$\begin{aligned} \tilde{P}_{m\nu}(\mathbf{k}) &=< \chi_{\mathbf{k}m}|\psi_{\mathbf{k}\nu} > \\ \tilde{P}^*_{\nu m}(\mathbf{k}) &=< \psi_{\mathbf{k}\nu}|\chi_{\mathbf{k}m} > \end{aligned} \quad (2.34)$$

This matrix is not quadratic because the correlated subspace is generally smaller than the subspace $\mathcal{W}$ of Bloch bands. Only if the system has well separated low - energy bands, the size of the correlated subspace and the subspace of Bloch bands can be the same.

The localized orbitals can be written in terms of the Bloch functions as

$$|\chi_{\mathbf{k}m}>=\sum_{\nu}<\psi_{\mathbf{k}\nu}|\chi_{\mathbf{k}m}>|\psi_{\mathbf{k}\nu}>. \tag{2.35}$$

If we use now the projection matrices equation (2.34), the functions in equation (2.35) can be rewritten as

$$|\tilde{\chi}_{\mathbf{k}m}>=\sum_{\nu\in\mathcal{W}}<\tilde{P}^{*}_{\nu m}(\mathbf{k})|\psi_{\mathbf{k}\nu}>=\sum_{\nu\in\mathcal{W}}<\psi_{\mathbf{k}\nu}|\chi_{\mathbf{k}m}>|\psi_{\mathbf{k}\nu}>. \tag{2.36}$$

This functions are not normalized, but we can define the overlap marix as

$$O_{mm'}(\mathbf{k})=<\tilde{\chi}_{\mathbf{k}m}|\tilde{\chi}_{\mathbf{k}m'}>=\sum_{\nu\in\mathcal{W}}\tilde{P}_{m\nu}(\mathbf{k})\tilde{P}^{*}_{\nu m}(\mathbf{k}). \tag{2.37}$$

The orthanormalization of local orbitals to true wannier functions are then obtained by

$$\phi_{\mathbf{k}m}=\sum_{m'}[O(\mathbf{k})]^{-\frac{1}{2}}_{m'm}|\tilde{\chi}_{\mathbf{k}m'}>, \tag{2.38}$$

and correspondingly the normalized projection matrices

$$\begin{aligned} P_{m\nu}(\mathbf{k})&=\sum_{m'}[O(\mathbf{k})]^{-\frac{1}{2}}_{mm'}\tilde{P}_{m'\nu}(\mathbf{k})\\ P^{*}_{\nu m}(\mathbf{k})&=\sum_{m'}[O(\mathbf{k})]^{-\frac{1}{2}}_{m'm}\tilde{P}_{\nu m'}(\mathbf{k}) \end{aligned} \tag{2.39}$$

Because of the orthonormalization, one can find the unitarity relation

$$\left(P(\mathbf{k})\cdot P^{+}(\mathbf{k})\right)_{mm'}=\sum_{\nu}P_{m\nu}(\mathbf{k})\cdot P^{*}_{\nu m'}(\mathbf{k})=\delta_{mm'}. \tag{2.40}$$

The implementation of equation (2.40) is not valid because $P^{+}(\mathbf{k})$ is generally not quadratic:

$$P(\mathbf{k}) \cdot P^{+}(\mathbf{k}) \neq \mathbb{I}. \tag{2.41}$$

In the case when the subspace of Bloch bands is equally large as the correlated subspace, the projection matrices are unitary. If we insert equation (2.39) into equation (2.31), the local Green's function, projected onto the local orbitals, is given by

$$G^{loc}_{mm'}(i\omega_n) = \sum_{\mathbf{k}} \sum_{\nu\nu'} P_{m\nu}(\mathbf{k}) \cdot G^{B}_{\nu\nu'}(\mathbf{k}, i\omega_n) \cdot P^{*}_{\nu' m'}(\mathbf{k}), \tag{2.42}$$

with the corresponding Bloch Green's function, given by

$$G^{B}_{\nu\nu'}(\mathbf{k}, i\omega_n) = \left(\left[(i\omega_n + \mu)\mathbb{I} - \epsilon_{\mathbf{k}} - \Delta\Sigma^{B}(\mathbf{k}, i\omega_n) \right]^{-1} \right)_{\nu\nu'}, \tag{2.43}$$

and the corresponding Bloch self - energy, calculated from the impurity self - energy of DMFT, defined as

$$\Delta\Sigma^{B}_{\nu\nu'}(\mathbf{k}, i\omega_n) = \sum_{mm'} P^{*}_{\nu m}(\mathbf{k}) \left[\Sigma^{imp}_{mm'}(i\omega_n) - \Sigma^{dc}_{mm'} \right] P_{m'\nu'}(\mathbf{k}) \tag{2.44}$$

If the projection matrices are quadratic, they have an inverse matrix. Thus, the local Green's function of equation (2.42) can be written in the following form:

$$\begin{aligned} G^{loc}(i\omega_n) &= \sum_{\mathbf{k}} \left(P^{+}(\mathbf{k}) \right)^{-1} \cdot G^{B}(\mathbf{k}, i\omega_n) \cdot \left(P(\mathbf{k}) \right)^{-1} \\ &= \sum_{\mathbf{k}} \left(P(\mathbf{k}) \left[(i\omega_n + \mu)\mathbb{I} - \epsilon_{\mathbf{k}} - \Delta\Sigma^{B}(\mathbf{k}, i\omega_n) \right] P^{+}(\mathbf{k}) \right)^{-1} \\ &= \sum_{\mathbf{k}} \left[(i\omega_n + \mu)\mathbb{I} - P(\mathbf{k})\epsilon_{\mathbf{k}} P^{+}(\mathbf{k}) - \Sigma^{imp}(\mathbf{k}, i\omega_n) + \Sigma^{dc} \right]^{-1}. \end{aligned} \tag{2.45}$$

For the quadratic case $P(\mathbf{k})\epsilon_{\mathbf{k}} P^{+}(\mathbf{k})$ assume the role of $H^{kin}(\mathbf{k})$.

2.3 Maximally Localised Wannier Functions

This section will briefly introduce the method of maximally localised wannier functions as proposed by Marzari and Vanderbilt [MV97]. The practically implementation is good described in [MYL+08]. Wannier functions are defined as the Fourier transform of the Bloch functions (output if DFT), given by

$$\phi_\nu(\mathbf{r}-\mathbf{R}) = \frac{V}{(2\pi)^3}\int d\mathbf{k}\psi_{\nu\mathbf{k}}(\mathbf{r})e^{-i\mathbf{kR}}, \tag{2.46}$$

where V is the unit cell volume in real space, and the integral is over the Brillouin zone (BZ). The Bloch wave functions result from the sum of the lattice periodic part $u_{\nu\mathbf{k}}(\mathbf{r})$. We can rewrite them as follows:

$$\psi_{\nu\mathbf{k}}(\mathbf{r}) = u_{\nu\mathbf{k}}(\mathbf{r})\cdot e^{-i\mathbf{kr}}. \tag{2.47}$$

Since functions $u_{\nu\mathbf{k}}(\mathbf{r})$ are not uniquely defined, there is still the freedom in the choice of the phase factor of the Bloch orbitals. It transforms to the freedom of performing a unitary rotation in the multi - band case:

$$u_{\nu\mathbf{k}}(\mathbf{r}) \longmapsto \sum_{\nu'} U_{\nu\nu'}(\mathbf{k})\cdot u_{\nu'\mathbf{k}}(\mathbf{r}). \tag{2.48}$$

Marzari and Vanderbilt suggested for the optimal (maximal) localization of the resulting the use of the arbitrary k - dependent unitary matrix $U_{\nu\nu'}(\mathbf{k})$. They defined the localization or "spread" functional Ω [FB60], which is the sum of the quadtratic spreads of the wannier probability distributions:

$$\Omega = \sum_\nu [< r^2 >_\nu - < r >_\nu^2], \tag{2.49}$$

where $< r^2 >_\nu$ is the expectation value of the squered position operator r^2 in the ν - th wannier function, and $< r >_\nu^2$ is the expectation value of the position operator. The minimisation of this functional is carried

out using the minimisation algorithm with smallest descents, which is described in detail in [MV97].

This construction scheme is valid only if the numbers of constructed wannier functions and input Bloch functions are not different. To do this, it is required that a certain isolated set of Bloch bands can construct a correlated subspace of the appropriate size.

2.4 Coulomb interaction tensor

In the following, we will consider important properties of the Coulomb interaction tensor (U - matrix). First we go back to the many - body Hamiltonian introduced in the previous section. The general form of the Coulomb interaction term can be written as

$$\hat{H}_U = \frac{1}{2}\sum_{ijkl}\sum_{mnpq}\sum_{\sigma\sigma'} U^{ijkl}_{mnpq}\hat{c}^{\dagger}_{im\sigma}\hat{c}^{\dagger}_{jn\sigma'}\hat{c}_{lq\sigma'}\hat{c}_{kp\sigma}, \tag{2.50}$$

for all bands that were considered in the energy window with the interaction parameters

$$U^{ijkl}_{mnpq} = \int \mathrm{d}(\mathbf{r},\mathbf{r}')\,\phi^*_{m\sigma}(\mathbf{r}-\mathbf{R_i})\phi^*_{n\sigma'}(\mathbf{r}'-\mathbf{R_j})\frac{1}{|\mathbf{r}-\mathbf{r}'|}\phi_{q\sigma'}(\mathbf{r}'-\mathbf{R_l})\phi_{p\sigma}(\mathbf{r}-\mathbf{R_k}), \tag{2.51}$$

where $\phi_{m\sigma}(\mathbf{r}-\mathbf{R_i})$ is a basis set of localized Wannier functions centered at each atomic sit $\mathbf{R_i}$. We assume that the intersite Coulomb interactions could be neglected (i=j=k=l) and the most important Coulomb interactions are among electrons in a single electronic shell(l is fixed). Thus, the Coulomb interaction has the following form

$$\hat{H}_U = \frac{1}{2}\sum_{i}\sum_{mm'm''m'''}\sum_{\sigma\sigma'} U_{mm'm''m'''}\hat{c}^{\dagger}_{im\sigma}\hat{c}^{\dagger}_{im'\sigma'}\hat{c}_{im'''\sigma'}\hat{c}_{im''\sigma'}. \tag{2.52}$$

It is convenient to expand the Coulomb interaction in terms of spherical harmonics as

$$\frac{1}{|\mathbf{r}-\mathbf{r}'|} = \sum_{k=0}^{\infty}\sum_{q=-k}^{k}\frac{4\pi}{2k+1}\frac{r^k_<}{r^{k+1}_>}Y_{kq}(\Theta,\phi)Y^*_{kq}(\Theta',\phi'), \tag{2.53}$$

where $r_>$ ($r_<$) is greater (lesser) of $\mathbf{r}$ and $\mathbf{r}'$.

We use this expansion to rewrite equation (2.51) and get:

$$U_{mm'm''m'''} = \sum_{k=0}^{2l} a_k(mm'm''m''')F^k, \tag{2.54}$$

where the angular and radial integrals are divided, and a_k is the angular part given by

$$a_k(mm'm''m''') = \frac{4\pi}{2k+1}\sum_{q=-k}^{k} < lm|Y_{kq}|lm' >< lm''|Y^*_{kq}|lm''' >, \tag{2.55}$$

and the radial part F^k is the Slater integral

$$F^k = \int dr \int dr'(rr')\frac{r^k_<}{r^{k+1}_>}R^2_{nl}(r)R^2_{nl}(r'). \tag{2.56}$$

All two - index terms could be written in equation (2.52), using the direct $U_{mm'} \equiv U_{mm'mm'}$, and exchange $J_{mm'} \equiv U_{mm'm'm}$ matricies, so the interaction Hamiltonian is expressed

$$\begin{aligned}\hat{H}_U = &\frac{1}{2}\sum_i \sum_{\sigma,m,m'} U_{m,m'}n_{m\sigma}n_{m'-\sigma} + \frac{1}{2}\sum_{\sigma,m\neq m'}(U_{mm'} - J_{mm'})n_{m\sigma}n_{m'\sigma} \\ &+ \sum_i \sum_{m\neq m'} J_{mm'}(\hat{c}^\dagger_{im\uparrow}\hat{c}^\dagger_{im'\downarrow}\hat{c}_{im\downarrow}\hat{c}_{im'\uparrow} + \hat{c}^\dagger_{im\uparrow}\hat{c}^\dagger_{im\downarrow}\hat{c}_{im'\uparrow}\hat{c}_{im'\downarrow}),\end{aligned} \tag{2.57}$$

which contains density - density interactions, spin - flip and pair - hopping terms. We obtain now the Coulomb interaction tensor for the d - orbitals in the real harmonic basis. We define first the Coulomb parameters for a certain value of angular momentum l

$$U = \frac{1}{(2l+1)^2}\sum_{mm'} U_{mm'} = F^0, \tag{2.58}$$

$$(U - J) = \frac{1}{2l(2l+1)}\sum_{mm'}(U_{mm'} - J_{mm'}). \tag{2.59}$$

For the d - orbitals, we can parametrize the Coulomb interactions by only three Slater integrals; F_0,F_2,F_4. The ratio between parameters is almost a constant. Thus, we can parametrize the two - index direct

and exchange matrices for the d shell orbitals. In the basis of the real harmonics as ($|xy>, |yz>$, $|3z^2$ - $r^2>$, $|xz>$, $|x^2$-$y^2>$), we have

$$U_{mm'} = \begin{pmatrix} U_0 & U_1' & U_2' & U_1' & U_3' \\ U_1' & U_0 & U_4' & U_1' & U_1' \\ U_2' & U_4' & U_0 & U_4' & U_2' \\ U_1' & U_1' & U_4' & U_0 & U_1' \\ U_3' & U_1' & U_2' & U_1' & U_0 \end{pmatrix}$$

where $U_i' = U_0$ - $2J_i$ with $U_0 = U + \frac{8}{7} J = F_0 + \frac{8}{7} \frac{F_2+F4}{14}$ and

$$\begin{aligned} J_1 &= \frac{1}{49}\left(3F_2 + \frac{20}{9}F_4\right), \\ J_2 &= 3J_1 - 2\frac{5}{7}\frac{F_2+F_4}{14}, \\ J_3 &= -5J_{J_1} + 6\frac{5}{7}\frac{F_2+F_4}{14}, \\ J_4 &= -3J_1 + 4\frac{5}{7}\frac{F_2+F_4}{14}. \end{aligned}$$

2.5 Double - Counting problem

When combining the density functional theory with dynamical mean - field theory, we encounter a double - counting of correlations that have been included in both DFT and DMFT, treated it by each approach in its own way. The significant part of the electronic correlations already contained in the DFT has to be subtracted from the Hamiltonian by introducing an additional parameter (the double - counting correction). The spectral function was in good agreement with experiments only when the double - counting correction is obtained as an adjustable parameter [KUW$^+$10]. There was no precise identification of the double - counting using DFT implemented in the local - density or generalized - gradient approximations (LDA or GGA).

Nevertheles, different approximation schemes for double - counting were developed. There are two widely used double - counting correction approaches in the literature: first, the around - mean - field correction (AMF) introduced by V. I. Anisimov et al. [AZA91], and second, the fully - localized limit approach by M. Czyzyk and G. Sawatzky [CdzS94]. Both methods have been originally developed for use in the LDA + U approach [AZA91,AAL97].The LDA + U method, explicitly introduces the Hubbard U - kind of interaction between the localized orbitals. The method, similar to the Anderson [And61] or Hubbard models [Hub63], separates the electrons into two sets: delocalized s, p, that are usually well described by the LDA method. The other set is localized d - or f - states, to which the Coulomb repulsion U between electrons in the same shell is added as in the Hartree - Fock approximation [CdzS94]

$$H_{HF} = \frac{1}{2}\sum_{\sigma,m,m'} U_{m,m'} n_{m\sigma} n_{m'\bar{\sigma}} + \frac{1}{2}\sum_{\sigma,m\neq m'} (U_{mm'} - J_{mm'}) n_{m\sigma} n_{m'\sigma}, \quad (2.60)$$

where $U_{mm'}$ and $J_{mm'}$ are the Coulomb - and exchange interaction respectively, and $n_{m\sigma} = c^{\dagger}_{m\sigma}\, c_{m\sigma}$ are occupation number operators.

The DFT + U total energy functional may be written in the form:

$$E_{DFT+U} = E_{DFT}[n_\uparrow, n_\downarrow] + E_{HF}[n_{m\sigma}] - E_{DC}. \tag{2.61}$$

The AFM and the FLL approaches are based on the assumption that the double - counting energy can be written as mean - field component of the Hartree - Fock, $E_{DC} = < H_{HF} >$. Using the Wick's theorem [Czy08] for the equation (2.60)

$$< c^\dagger_\alpha c^\dagger_\beta c_\gamma c_\delta > = < c^\dagger_\alpha c_\delta >< c^\dagger_\beta c_\gamma > - < c^\dagger_\alpha c_\gamma >< c^\dagger_\beta c_\delta >, \tag{2.62}$$

and assuming that the non-diagonal terms can be neglected, we get:

$$\begin{aligned} < H_{HF} > = & \frac{1}{2} \sum_{mm'\sigma} U_{mm'}(< n_{m'\bar{\sigma}} >< n_{m\sigma} >) \\ & + \frac{1}{2} \sum_{mm'\sigma, m \neq m'} (U_{mm'} - J_{mm'})(< n_{m'\sigma} >< n_{m\sigma} >). \end{aligned} \tag{2.63}$$

The AMF approach assumes that the LDA corresponds to the mean - field solution. The exchange and correlation effects are rotationally invariant in the LDA potential. The occupation numbers are orbital - independent. So the AMF approximates the included interaction by calculating the difference between the interaction in Hubbard form and their deviations from a mean field value for the occupation number. Thus the spin - occupation numbers can be written as [CdzS94]

$$N_\sigma = \sum_m < n_{m\sigma} >, \tag{2.64}$$

The resulting double - counting expression (with interactions defined in equation (2.58) and equation (2.59)) is given by

$$H^{AMF}_{DC} = UN^2 - \frac{1}{2}\frac{2l}{2l+1}(U - J)\sum_\sigma N^2_\sigma, \tag{2.65}$$

in which N=($N_\uparrow$+$N_\downarrow$) is the total occupation, and N_σ the occupation per spin.

The corresponding double - counting energy has the following formula:

$$E_{DC}^{AMF} = UN_\uparrow N_\downarrow + \frac{1}{2}(N_\uparrow^2 + N_\downarrow^2)\frac{2l}{2l+1}(U-J). \tag{2.66}$$

The idea of the FLL approach is that the energy of the atomic limit is determined on the assumption that the localized d - and f - electrons have almost atomic character (localized orbitals).

The double - counting term is given by [CdzS94]:

$$H_{DC}^{FLL} = \frac{1}{2}UN(N+1) - \frac{1}{2}J\sum_\sigma N_\sigma(N_\sigma - 1), \tag{2.67}$$

where N and N_σ have the same meaning as in the AMF case. The corresponding double - counting energy within this approximation has the following form:

$$E_{DC}^{FLL} = \frac{U}{2}N(N-1) - \frac{J}{2}(N_\uparrow(N_\uparrow - 1) + N_\downarrow(N_\downarrow - 1)). \tag{2.68}$$

These approaches are necessary because the Coulomb interaction of the d - electrons in unknown form is contained in the exchange correlation potential. Therefore, no final statement can be made about which approach leads to better results. Both approaches don't work for all cases. This depends on the kind of materiails. The around mean - field approximation is better suitable for metals or "weakly correlated" systems and the fully - localized limit more suitable for the "strongly correlated" systems.

2.6 Numerical Methods and Algorithms

Impurity Solver

In the DMFT method, the lattice model can be mapped to a quantum impurity Anderson model. Thus, the lattice problem is reduced to effective single impurity problem. Fortunately, impurity models have been of long - standing interest, and few methods have been developed to handle them. The numerical renormalization group (NRG) [BCV01], exact diagonalization (ED) [CK94] , and especially the quantum Monte Carlo (QMC) [GML$^+$11a] methods are of the most important numerical methods. The advantage of this algorithms is that they are "numerically" exact. Nonetheless, the big drawbacks are the large computational requirements of the schemes and the introduced Monte - Carlo noise. In the next Section we will present briefly the hybridization expansion continuous time (CT - Hyb) Quantum Monte Carlo algorithm [WCD$^+$06, WM06, GML$^+$11a] as implemented in the TRIQS code [SKFP16] that was used to obtain "exact" solutions of the Anderson impurity model.

TRIQS/CTHYB

The hybridization - expresion quantum Monte Carlo (CT - Hyb algorithm), implemented in the TRIQS/CTHYB code, has gotten several important improvements and optimization algorithms for the effective treatment of multi - orbital strongly correlated systems. We briefly describe the general method, as well as the automatic partitioning (autopartition) algorithm which divides the local Hilbert space into subspaces, and the realization of the left - leaning red - black tree [SKFP16].

The main idea of CT - QMC start from the splitting the effective action S into two parts, an exactly solvable part S_0 and a not neces-

sarily small part ΔS. The partitition function Z can be found, if the path - integral evaluation will be done in a perturbative way using a power series expansion:

$$Z = \int \mathcal{D}[c^* c] e^{-S_0 - \Delta S} \tag{2.69}$$

$$= \int \mathcal{D}[c^* c] e^{-S_0} \sum_k \frac{(-1)^k}{k!} (\Delta S)^k. \tag{2.70}$$

A possible decomposition can be found already in equation (2.24):

$$\mathcal{S} = -\int_0^\beta d\tau \int_0^\beta d\tau' \sum_\sigma c^*_\sigma(\tau) \mathcal{G}_0^{-1}(\tau - \tau') c_\sigma(\tau') \tag{2.71}$$

$$\Delta S = U \int_0^\beta d\tau n_\uparrow(\tau) n_\downarrow(\tau). \tag{2.72}$$

This is the basic idea of interaction - expansion or "weak - coupling" CT - QMC [RL04]. It induces the following expansion [GML+11a] of the partition function Z (knowing the exact part Z_0):

$$Z = Z_0 \sum_{k=0}^{\infty} \frac{(-U)^k}{k!} \int_0^\beta d\tau_1 \cdots d\tau_k \left(\prod_\sigma det \mathbf{D}^\sigma_\mathbf{k} \right) \tag{2.73}$$

$$(\mathbf{D}^\sigma_\mathbf{k})_{ij} = \mathcal{G}^\sigma_0(\tau_i - \tau_j). \tag{2.74}$$

Some additional tricks are necessary to avoid sign problems. Thus, such an approach leads to small perturbation orders, especially for small interactions U. The hybridization - expression or "strong - coupling" CT - QMC [WCD+06, WM06] does the opposite and is especially effective for large interactions U. This hybridisation - expression idea makes an expansion of the partition function in powers of the hybridization between impurity and bath. The time evolution is done by the local part of the Hamiltonian. In the effective action formalism, this corresponds to the hybridisation function $\Delta(\tau)$ [Hau07]:

$$\Delta S = \int_0^\beta \mathrm{d}\tau \int_0^\beta \mathrm{d}\tau' \sum_{\alpha\beta} c^*_\alpha(\tau)\Delta_{\alpha\beta}(\tau-\tau')c_\beta(\tau'). \tag{2.75}$$

The partition function is given as (similar to the interaction expansion approach) [GML+11a]

$$\begin{aligned} Z = Z_{bath} \sum_k \int d\tau_1 \cdots d\tau_k \sum_{\alpha_1\cdots\alpha_k} \sum_{\alpha'_1\cdots\alpha'_k} Tr_c[T_\tau e^{-\beta \hat{H}_{loc}} \\ \cdot c_{\alpha_k}(\tau_k)c_{\alpha'_k}\cdots c_{\alpha_1}(\tau_1)c_{\alpha'_1}(\tau'_1)] \det \mathbf{M}^{-1} \end{aligned} \tag{2.76}$$

$$(\mathbf{M}^{-1})_{lm} = \Delta_{j_l j_m}(\tau_l - \tau_m). \tag{2.77}$$

Thus, it is the task of the Monte - Carlo algorithm to estimate the integrants. More details can be found here [GML+11a].

If we detaily consider this equations, it is clear that the order of expansion causes the size of the hybridization matrices in the perturbation expansion. We obtain a very large local Hilbert space, i.e., in case of d - orbital systems it has already $2^{10} = 1024$ - dimensions.

The gain factor for calculating the dynamic trace can be obtained by the partition of the local Hilbert space in the form of a diagonal block structure, which agrees with the symmetries of the system under consideration, shown in Fig. 2.1. Then the matrix multiplications in the dynamic trace must be executed only within the subspaces.

The efficiency of calculating the dynamical trace, and therefore also the computantional enhancement, can be improved by presenting it in terms of a tree structure. Storing configurations and paired operator products in the trace in the tree reduces the number of matrix multiplications that must be recalculated after each QMC update because only a small subset of leaves changes. It is shown in Fig. 2.2, where $\mathcal{O}(\log_2(\beta))$ is the tree scaling and $\mathcal{O}(\beta^3)$ is that of the determinants. At low temperatures the calculation of the hybridization determinants dominates over that of the dynamical trace, while at high temperatures it will be the reverse. The average perturbation order $\langle k \rangle$ is approximately proportional to β.

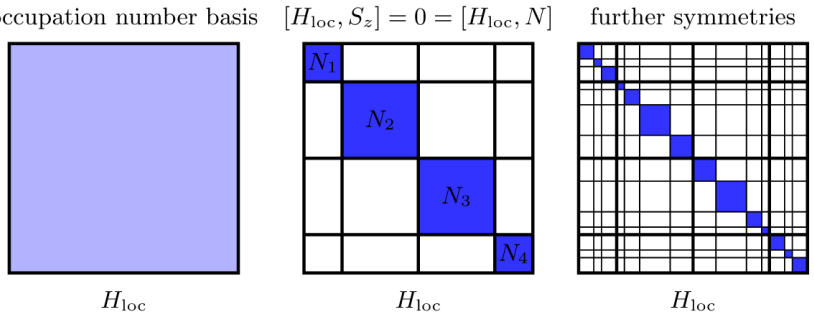

Figure 2.1: Sketch of results of the autopartition algorithm. From Ref. [GML+11b].

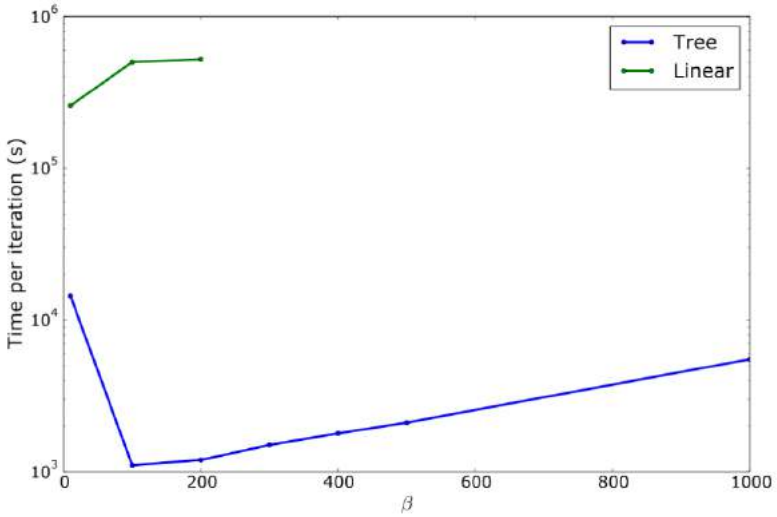

Figure 2.2: Scaling of computational time with inverse temperature β for a representative 5 - orbital system containing three electrons subject to a rotationally invariant full Hamiltonian. The tree algorithm is compared against the linear case where the full trace is recomputed after each QMC update. From Ref. [SKFP16].

2.7 Momentum resolved spectral function - ARPES

In this section we obtain momentum - resolved spectral functions and are thus able to compare our results with recent angular resolved photoemission (ARPES) studies.

(a) Spin - up

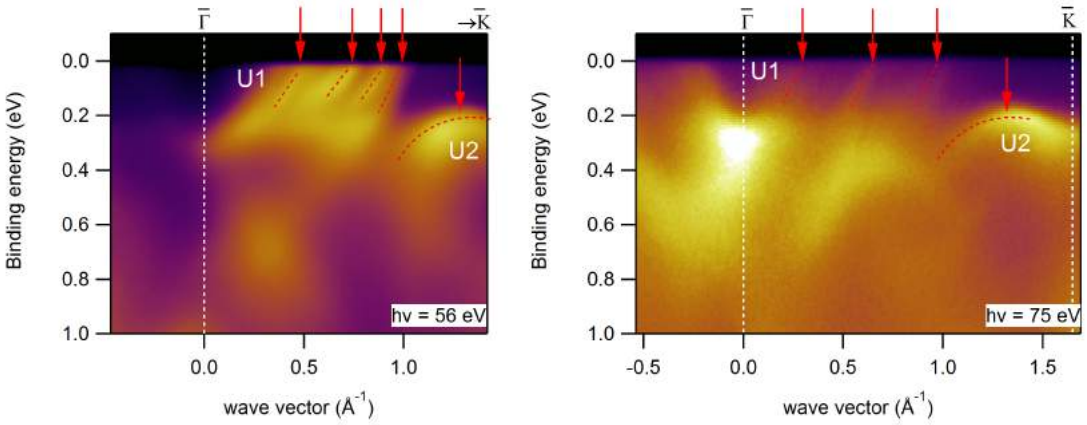

(b) Spin - down

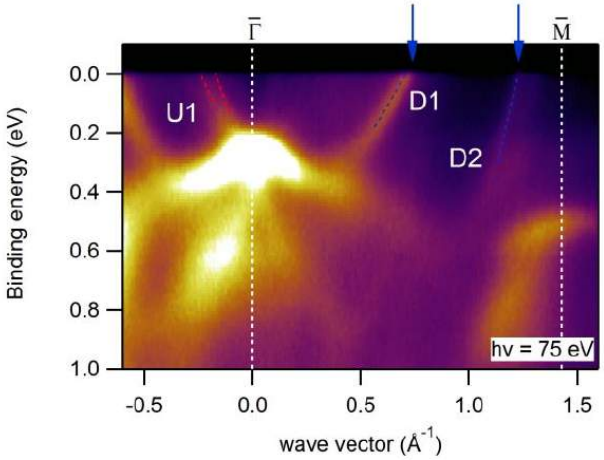

Figure 2.3: Majority and minority states, ARPES spectra on a 15 ML hcp cobalt film along GK and GM directions, respectively

First, we will discuss and describe details of the experimental data. Figure 2.3 shows ARPES spectra taken on a (approximately) 15 ML Co film on W(110) along GK (GM for spin - down) high symmetry direction with two different photon energies. In the proximity of the Fermi level a number of quantized states can be observed, their position does not change with varying the photon energy. Only the relative intensity is modulated due to the matrix element effects. For example, at 56 eV photon energy we can see clearly the nearly linear states in the proximity of the Fermi level at positive wave vector values (we will refer to them as U1 in the following). We evidence some of them by dashed red lines. The same states U1 are much weaker at 75 eV, while one can see better the less dispersive state below 0.2 eV close to the K point (U2 in the following). All these states have majority character according to the spin - resolved data. To perform a better comparison to the calculations we will refer to two parameters: the slope of the U1 state, and the binding energy of the U2 state.

The states that have a minority character according to the spin - resolved data are better seen along the GM direction. We mark them by D1 and D2. The D1 states is overlapping with the majority states, but at this energy and experimental geometry its intensity is selectively enhanced, and the spin - resolved maps provide a clear evidence for its minority character.

We performed DFT + DMFT calculation for 5 ML slab hcp cobalt in order to achive a better agreement between experimental and theoretical data. In all cases U = 3.5 and J = 0.75 eV were applied. The momentum - resolved spectral function was computed from the QMC data as follows:

$$A_i(\mathbf{k},\omega) = -\frac{1}{\pi} Im\big(\omega + \mu - \epsilon_i(\mathbf{k}) - \Sigma_i(\omega)\big)^{-1}, \tag{2.78}$$

which is shown in Fig. 2.4 together with the data of spin - resolved ARPES measurments for 15 ML films.

We can show in Fig. 2.4 an overall good agreement of the observed states: there are several nearly linear states in the proximity of the

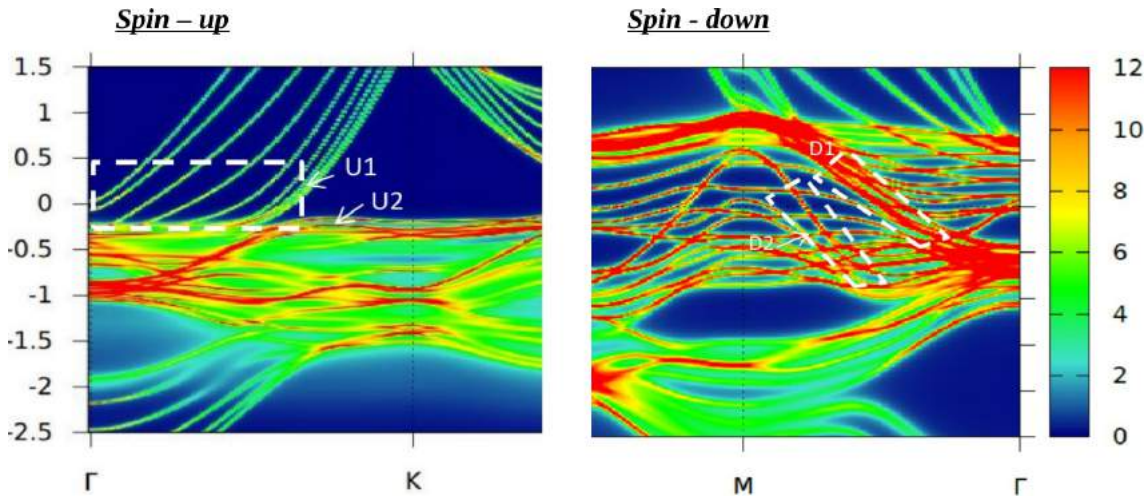

Figure 2.4: Majority (left) and minority (right) states, 5 ML hcp cobalt along GK and GM directions, respectively

Fermi level, similar to U1 and a curved state in the proximity of the K point, similar to the U2. The calculated (but not here presented) DFT bands have a strong disagreement with the experimental spectra in the slope of the U1 states and the binding energy of the U2 state. Including the correlation effects gives the correct values.

The spin - down band structure shows features, which are also in a good agreement with dispersion and binding energy of the D1 and D2 states.

Three

Quantum many - body intermetallics

Fe_3Al - iron based aluminides have been a subject of great interest for years because of their excellent corrosion resistance, specific stiffness, good wear resistance and good processability. Fe_3Al exhibit limited strength and creep resistance at high temperatures and low ductility at ambient temperatures. These alloys undergo a persistent transformation from a DO_3 structure (highly ordered) to a B2 structure (imperfectly ordered) at around 820 K upon heating, thus, resulting in a sharp drop in strength [MDTS91]. Former experimental and theoretical investigations revealed that there is a very complicated phase diagram that shows a complex interaction between metallicity, magnetism, and structure. Although theoretical studies based on first - principles calculations have already studied Fe_3Al [GOPS06], [LFS05], [Col03], [LWE$^+$02], [RD02], [SSJ05], [DRJD02], the correlation between magnetic properties and the stability of these alloys is not well established. Previous authors used LSDA to describe/investigate the electronic, magnetic properties and phase stability of bcc - based DO_3 - Fe_3Al. Former calculations within the framework of the LSDA have shown that the systematics of the formation of magnetic moments on Fe atoms in various transition - metal hosts depend very sensitively on the symmetry of the transition - metal hosts. We now concentrate on the additional influence of electronic correlations beyond LSDA. The DFT + U method, which includes static correlation effects, can handle some of the subtle energetics for a good choice of the local Coulomb - interaction parameters. This scheme is not well defined

for correlated itinerant systems and, normally has to enforce magnetic order to give correct results. The conventional DFT or DFT + U are usually used to describe non - magnetic (NM) or magnetically ordered compounds, but true paramagnetic (PM) states are not available in both methods. In general, Fe - Al compounds are hard to describe in conventional DFT, as shown in various relevant publications, and we here show that the advanced DFT + DMFT approach can improve thereon. In this work we document the important impact of many - body effects on the electronic structure in two prominent intermetallic systems, namely Fe_3Al and Fe_2VAl.

The Heusler compounds [Heu03] were discovered in 1901. They benefit from rising interest because of their high Curie temperature, their high spin polarization, and their low magnetic Gilbert damping. We are interested in the so - called full-Heusler structure $X_{(2)}YZ$ - intermetallics. Here X and Y are transition metals and Z is a main group element, which crystallizes in the cubic L21 structure. Fe_2VAl was first proposed to be a 3d heavy fermion candidate in 1997 by Y.Nishino et.al [NKA$^+$97]. The electrical and magnetic properties of Fe_2VAl vary from metals to semiconductors. They observed a large decrease of resistivity with rising temperature, a moderately coefficient of resistivity clearly distinguished this material from typical metals. On the other hand, a crystalline semiconductor would not have a very distinct Fermi edge because of the low density of states at E_F. Since then, many articles have been published reflecting on the physical properties of this alloy. The physical picture behind these seemingly contradictory physical properties is still not clear. Experiments characterize Fe_2VAl as a semiconductor with narrow gap of 90 - 130meV [KNMA00, NTY$^+$05],100 - 200meV [OKN$^+$00, ISDSAM15], or 210 - 280 meV [LR98] as extracted from transport, optical, and nuclear magnetic resonance (NMR) measurements, respectively. Former theoretical studies based on first - principles calculations have shown that Fe_2VAl is a non - magnetic semimetallic with a low - density pseudogap of 0.1 - 0.2 eV [SM98, WP98], whereas the use of hybrid functionals renders the system semiconducting with a band gap of Δ_g

= 0.34 eV [BG11], and DFT + U calculations revealed a gap of Δ_g = 0.55 eV [DLM11]. In our study we go beyond conventional DFT(+U) to consider the effects of quantum fluctuations and finite temperature. A combination of DFT with DMFT reveals important modifications of the correlated electronic structure. For Fe_2VAl we found a strongly renormalized pseudogap of about 150meV at low temperatures and a mass - enhancement factor of 1.4 for vanadium states. It was identified to correlation - induced changes near the Fermi level. It is shown that the spectral weight at the Fermi level depends strongly on temperature, which leads to metallization with increasing temperature.

Our work is important for the materials science audience, since it renders it clear that electronic correlations are not only relevant for strongly correlated oxides but do matter also for selected intermetallic compounds. The charge self - consistent scheme makes it possible to reveal Fe_3Al formation energies in good agreement with experiment and account for the intricate gap opening in Fe_2VAl. Especially for the Fe - Al system, since bcc-Fe and Fe_3Al are not coherently - well described within DFT + DMFT, this method stands out since LDA(GGA) fails for bcc - Fe(Fe3Al). This should stimulate further reseach on the relevance of many - body effects in intermetallic systems.

Quantum many - body intermetallics: Phase stability of Fe_3Al and small - gap formation in Fe_2VAl

Reprinted with permission from

O. Kristanovski, R. Richter, I. Krivenko, A. I. Lichtenstein, and F. Lechermann

Physical Review B **95**, 045114 (2017).

The reference numbering used in this reprinted article is only valid within this specific article.

Quantum many-body intermetallics: Phase stability of Fe_3Al and small-gap formation in Fe_2VAl

Oleg Kristanovski,[1] Raphael Richter,[2] Igor Krivenko,[1] Alexander I. Lichtenstein,[1] and Frank Lechermann[1,3]
[1]*I. Institut für Theoretische Physik, Universität Hamburg, D-20355 Hamburg, Germany*
[2]*Institut für Technische Thermodynamik, Deutsches Zentrum für Luft- und Raumfahrt, D-70569 Stuttgart*
[3]*Institut für Keramische Hochleistungswerkstoffe, Technische Universität Hamburg-Harburg, D-21073 Hamburg, Germany*
(Received 22 September 2016; published 10 January 2017)

Various intermetallic compounds harbor subtle electronic correlation effects. To elucidate this fact for the Fe-Al system, we perform a realistic many-body investigation based on a combination of density functional theory with dynamical mean-field theory in a charge self-consistent manner. A better characterization and understanding of the phase stability of bcc-based $D0_3$-Fe_3Al through an improved description of the correlated charge density and the magnetic energy is achieved. Upon replacement of one Fe sublattice with V, the Heusler compound Fe_2VAl is realized, known to display bad-metal behavior and increased specific heat. Here we document a charge-gap opening at low temperatures in line with previous experimental work. The gap structure does not match conventional band theory and is reminiscent of (pseudo)gap characteristics in correlated oxides.

DOI: 10.1103/PhysRevB.95.045114

I. INTRODUCTION

The Fe-Al system is well known for its intricate phase diagram, displaying a complex interplay between metallicity, magnetism, and structure. Stoichiometric FeAl poses a longstanding problem regarding its magnetic ground state. While experimentally $B2$-FeAl is characterized as a Curie-Weiss paramagnet [1] with no detectable ordered moment, conflicting results exist in theory [2–5]. On the Al-rich side, the low-symmetry structures $FeAl_2$ and Fe_2Al_5 exhibit spin-glass physics at low temperature [6,7]. On the iron-rich side, in the Fe_3Al composition a bcc-based $D0_3$ crystal structure is stable with well-defined ferromagnetic (FM) order up to $T_c = 713$ K [8]. A further increase of the Fe content transforms the system into a doped bcc Fe (or α) phase, also with FM order below a Curie temperature of 1043 K for pure iron. Albeit unambiguous in nature, both α-Fe and $D0_3$-Fe_3Al appear difficult to be described within conventional density functional theory (DFT) [9–11]. The generalized-gradient approximation (GGA) for the exchange-correlation energy is necessary to detect the FM-bcc-Fe ground state [10]. Intriguingly, the FM-$D0_3$ compound is only stable within the local-density approximation (LDA), while GGA favors the fcc-based $L1_2$ structure in the ferromagnetic state [11].

This lack of a coherent theoretical description of the Fe-rich side of Fe-Al in standard Kohn-Sham DFT asks for extended approaches. The inclusion of static electronic correlation effects via the DFT+Hubbard U method may cope with part of the subtle energetics for a reasonable choice of the local Coulomb-interaction parameters [12]. But that scheme is in principle not well defined for correlated itinerant systems and, in addition, usually needs to enforce magnetic order to deliver proper results. True paramagnetic (PM) states based on fluctuating local moments are neither accessible in conventional DFT nor in DFT+U, which either describes non-magnetic (NM) or magnetically ordered compounds. Within the so-called disordered local moment (DLM) method [13,14] there is the chance to account for a DFT-based orientational mean-field effect of PM-like spins. Yet quantum fluctuations as well as general finite-temperature fluctuations of, e.g., the proper size of the local moments are still missing.

A further facet of the intriguing correlated electronic structure in iron aluminides is revealed when replacing one Fe sublattice in $D0_3$-Fe_3Al with vanadium. This transforms the intermetallic crystal into the Heusler $L2_1$ compound Fe_2VAl. The ordered alloy is paramagnetic down to lowest temperatures and displays bad-metal behavior in transport [15]. It is still a matter of debate if Fe_2VAl is a small-gap ($\sim$0.1–0.3 eV) semiconductor or a semimetal [16,17]. Reminiscent of f-electron systems such as SmB_6 with Kondo-insulating characteristics [18], heavy-fermion physics was originally associated with this $3d$-electron system [15,16]. Though magnetic defects later explained a sizable part of the large specific heat at low temperature, the overall mass enhancement remains substantial [19]. A promising thermoelectric potential due to an enhanced thermopower is associated with Fe_2VAl-based materials [20,21]. Again, a theoretical first-principles assessment is difficult, since, e.g., there are substantial differences concerning the existence of a charge gap Δ and its eventual size. Conventional DFT based on LDA/GGA classifies Fe_2VAl as semimetallic [22,23], whereas the use of hybrid functionals renders the system semiconducting with a band gap of $\Delta_g = 0.34$ eV [24]. A gap of $\Delta_g = 0.55$ eV is revealed from DFT+U calculations [25].

In this paper a first-principles many-body approach is employed to consider the effects of quantum fluctuations and finite temperature on the electronic structure of Fe_3Al and Fe_2VAl beyond conventional DFT(+U). A state-of-the-art combination of density functional theory with dynamical mean-field theory (DMFT) reveals important modifications of the correlated electronic structure. We show that the subtle electronic states rely on many-electron quantum processes, with important consequences for the phase stability and tendencies concerning gap formation. This paves the way towards a coherent modeling and understanding of Fe-Al and signals the general importance of advanced theoretical schemes for intermetallic systems.

II. CRYSTAL STRUCTURES

The crystal structures relevant for this work are displayed in Fig. 1. With bcc Fe and fcc Al as the end members, the

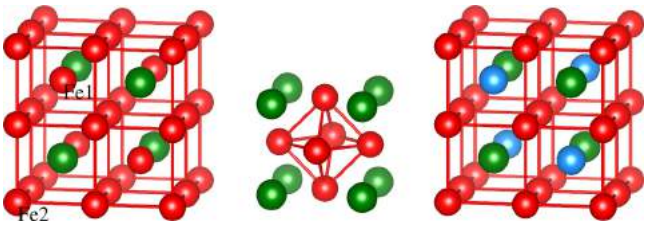

FIG. 1. Relevant crystal structures. From left to right: $D0_3$-Fe_3Al, $L1_2$-Fe_3Al, and $L2_1$-Fe_2VAl. Fe (red/light gray), Al (green/dark), and V (blue/gray).

cubic lattice system also accounts for the dominant ordered phases in Fe-Al. Starting with $B2$-FeAl at stoichiometry, the bcc lattice is the common host for the stable solid phases in the Fe-rich part. Though the $D0_3$ structure is stable in the Fe_3Al phase regime, the fcc-based $L1_2$ structure appears as a relevant competitor. The $D0_3$ unit cell consists of three Fe sites and one Al site, whereby the Fe basis atoms are grouped in two symmetry shells. One Fe site belongs to the Fe1 sublattice and two Fe sites to the Fe2 sublattice. As a bcc structure, each Fe site has eight nearest-neighbor (NN) sites. Whereas the Fe2 atoms have a mixed Fe/Al nearest neighborhood, the Fe1 atom has only Fe nearest neighbors. The experimental lattice constant of fully ordered Fe_3Al reads $a = 5.473$ a.u.

The $L1_2$ structure also consists of three Fe atoms and one Al atom in the primitive unit cell, but all Fe sites are equivalent by symmetry. The 12-atom NN shell of these Fe sites is composed again of both Fe and Al sites.

Finally, in the Heusler $L2_1$-Fe_2VAl compound, the Fe1 sublattice of the $D0_3$ structure is fully replaced with V atoms. The measured lattice constant amounts to $a' = 5.442$ a.u. [15,16].

Note that throughout this work we investigate the stoichiometric compounds, i.e., the defect physics and effects of chemical disorder are not treated.

III. COMPUTATIONAL FRAMEWORK

The charge self-consistent DFT+DMFT methodology [26–28] is put into practice, utilizing a mixed-basis pseudopotential approach [29,30] for the DFT part and the continuous-time quantum Monte Carlo scheme [31,32] from the TRIQS package [33,34] for the DMFT impurity treatment. Exchange correlation in the Kohn-Sham cycle is handled by the GGA functional of Perdew-Burke-Ernzerhof (PBE) [35] form.

The correlated subspace where quantum fluctuations are explicitly accounted for is associated with the transition-metal sites of Fe and V types. Projected local orbitals [36–40] of a $3d$ character are used to extract Wannier-like states based on 22 Kohn-Sham bands, stemming from Fe/V($3d\,4s$) and Al($3s\,3p$) orbitals. Each transition-metal site represents a DMFT impurity problem, which, due to symmetry, amounts to two such ones in $D0_3$-Fe_3Al and Fe_2VAl, while only one symmetry-inequivalent transition-metal site is hosted in $L1_2$-Fe_3Al. A multiorbital Hubbard Hamiltonian of Slater-Kanamori form, parametrized by the Hubbard U and the Hund's exchange J_H, is applied to the respective full five-orbital $3d$ manifold. We overtook the values $U = 3.36$ eV and $J_H = 0.71$ eV for the local Coulomb interactions from Ref. [5], where those are computed for $B2$-FeAl using the constrained random-phase approximation. A double-counting correction of the fully localized form is used in this work. If not stated otherwise, the temperature within the DMFT part is set to $T = 387$ K, i.e., $\beta = 1/T = 30\ \mathrm{eV}^{-1}$. The analytical continuation of the Green's functions on the Matsubara axis $i\omega$ is performed via the maximum-entropy method.

We mainly focus in our DMFT calculations on phases without broken spin symmetry, i.e., paramagnetic states. Albeit $D0_3$-Fe_3Al is ferromagnetic at ambient temperatures, the explicit magnetic-*ordering* energy, as will be shown below, is not of vital importance for our investigation and its conclusions.

IV. RESULTS

A. Fe_3Al

1. *Electronic states*

We first focus in some detail on the electronic states in Fe_3Al. Let us start with the fcc-based $L1_2$ structure, having only one transition-metal sublattice. The close-packed lattice type is an important one in intermetallic systems, e.g., the ordered phases Cu_3Au and Ni_3Al condense in the $L1_2$ structure. Because of the cubic symmetry, here the local Fe($3d$) states in principle split twofold into e_g and t_{2g} states. However, due to the ordering pattern, not all e_g/t_{2g} sublevels may still be degenerate. This is illustrated in Fig. 2, where the obtained Fe($3d$) projected local orbitals are plotted as isosurfaces. The e_g manifold consisting of $\{x^2 - y^2, z^2\}$ is defined by the orbital lobes pointing towards the next-nearest-neighboring (NNN) Fe sites. Since both pointing directions are anisotropic in terms of the respective nearest-neighbor sites, the two e_g are nondegenerate. The t_{2g} manifold consisting of $\{xz, yz, xy\}$ are defined by the orbital lobes pointing to the NN sites. For xz, yz the associated NN sites are exclusively of a Fe type, therefore both orbitals are degenerate. Yet in the case of xy, the associated NN shell consists exclusively of Al sites, thus this t_{2g} orbital has a different, in fact, the lowest effective, crystal-field level.

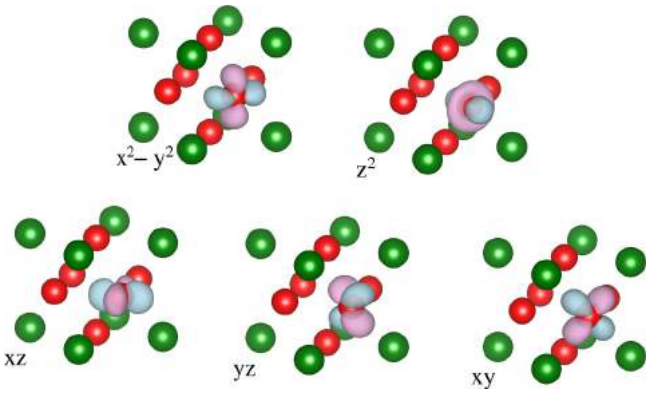

FIG. 2. Projected local Fe($3d$) orbitals in $L1_2$-Fe_3Al. On-site level energies: $\varepsilon_\alpha = \{-624, -699, -843, -843, -998\}$ meV for the effective orbitals $\alpha = \{x^2 - y^2, z^2, xz, yz, xy\}$.

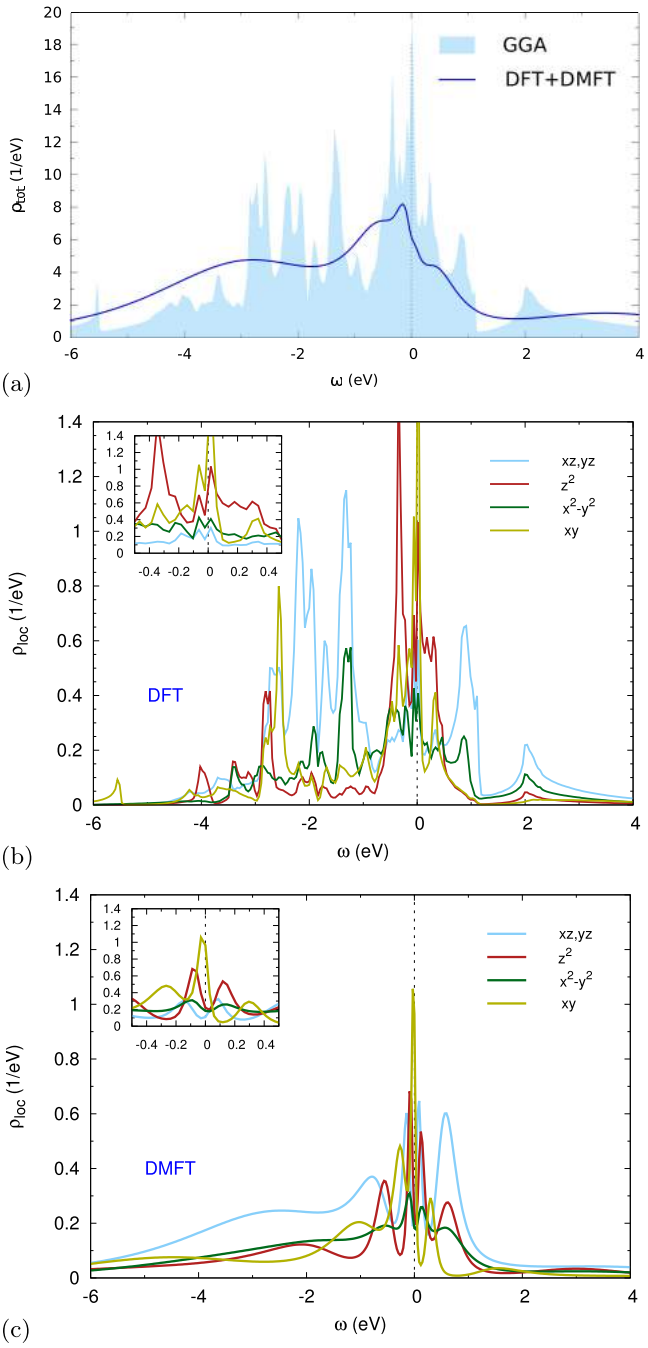

FIG. 3. Spectral functions of $L1_2$-Fe_3Al. (a) Total, (b) local Fe from GGA, and (c) local Fe from DFT+DMFT. Insets in (b) and (c) are low-energy blowups.

Figure 3 compares the integrated spectral functions $\rho(\omega) = \sum_{\mathbf{k}} A(\mathbf{k},\omega)$ of $L1_2$-Fe_3Al within DFT(GGA) and DFT+DMFT. From the broadly itinerant band structure, an effective relevant bandwidth of about 7 eV (ranging from -6 to 1 eV) may be read off. Seemingly, the full Fe($3d$) manifold is crucial to understand the electronic structure in the bonding part and at low energy, since the hybridization between Fe and Al is rather strong in a wide energy range. Close to the Fermi level, the z^2 and xy effective orbitals are most dominant in GGA, while, e.g., the xz/yz part displays a bonding-antibonding signature.

TABLE I. Projected local-orbital occupations in Fe_3Al. The first rows are GGA, and the second rows DFT+DMFT results, respectively.

		e_g		t_{2g}			
		x^2-y^2	z^2	xz	yz	xy	Total
$L1_2$	Fe	1.38	1.34	1.43	1.43	1.58	7.16
		1.55	1.56	1.54	1.54	1.79	7.98
$D0_3$	Fe1	1.45	1.45	1.31	1.31	1.31	6.83
		1.47	1.47	1.54	1.54	1.54	7.56
	Fe2	1.20	1.20	1.59	1.59	1.59	7.17
		1.45	1.45	1.70	1.70	1.70	8.00

For the xy state with a deepest crystal-field level and broad dispersion, the orbital filling is also largest (see Table I). The total local Fe electron count is slightly above seven within GGA. A further strengthening of the xy dominance at low energy occurs in the DFT+DMFT treatment. While the filling of all effective Fe orbitals increases with correlations, here also the occupation of the xy state is enhanced the most by relative means. Overall, a substantial increase in the total effective Fe($3d$) filling close to eight electrons takes place. Note that the site-filling differences between GGA and DFT+DMFT are also due to the respective effective-orbital definitions, as usual in determining local occupations in crystalline solids. First, the projected local orbitals in both calculational schemes are not identical (only the projecting functions are), since via the charge self-consistent loop the Kohn-Sham part (i.e., the bands used for the projection) changes. Second, the resulting orbitals are of a Wannier type, i.e., their spread is substantial and not localized on the site center within a small spherical radius.

Still, correlations may enhance the electron localization on the Fe sites. The correlation strength can be estimated from the quasiparticle (QP) weight $Z \sim 1/m_{\text{eff}}$, computed from the electronic self-energy on the Matusbara axis as

$$Z = \left(1 - \left.\frac{\partial\, \mathrm{Im}\, \Sigma(i\omega)}{\partial\omega}\right|_{\omega\to 0^+}\right)^{-1}. \quad (1)$$

There is no strong orbital variation of the QP weight in the $L1_2$ structure and it amounts to a moderate value of $Z \sim 0.7$.

Though the $D0_3$ structure consists of two different Fe sublattices, the conventional internal degeneracies of the e_g and t_{2g} subshells of Fe($3d$) are fulfilled here. This is due to the fact that the NN environments are either of a pure Fe type or of an equally mixed-isotropic Fe,Al type. As in fcc-based $L1_2$, the e_g orbitals point again towards NN and NNN sites. However, since bcc-based $D0_3$ is not close packed, the t_{2g} orbitals point in between the NN and NNN, i.e., towards the third-nearest-neighbor sites.

The total integrated spectral function of $D0_3$-Fe_3Al is similar to the one of $L1_2$-Fe_3Al [see Fig. 4(a)], but with a more pronounced quasiparticle peak at low energy. The effective relevant bandwidth seems also smaller by about 1 eV in extent. On the local level, the Fe1 spectrum exhibits stronger e_g-t_{2g} discrimination than the Fe2 spectrum. This speaks to

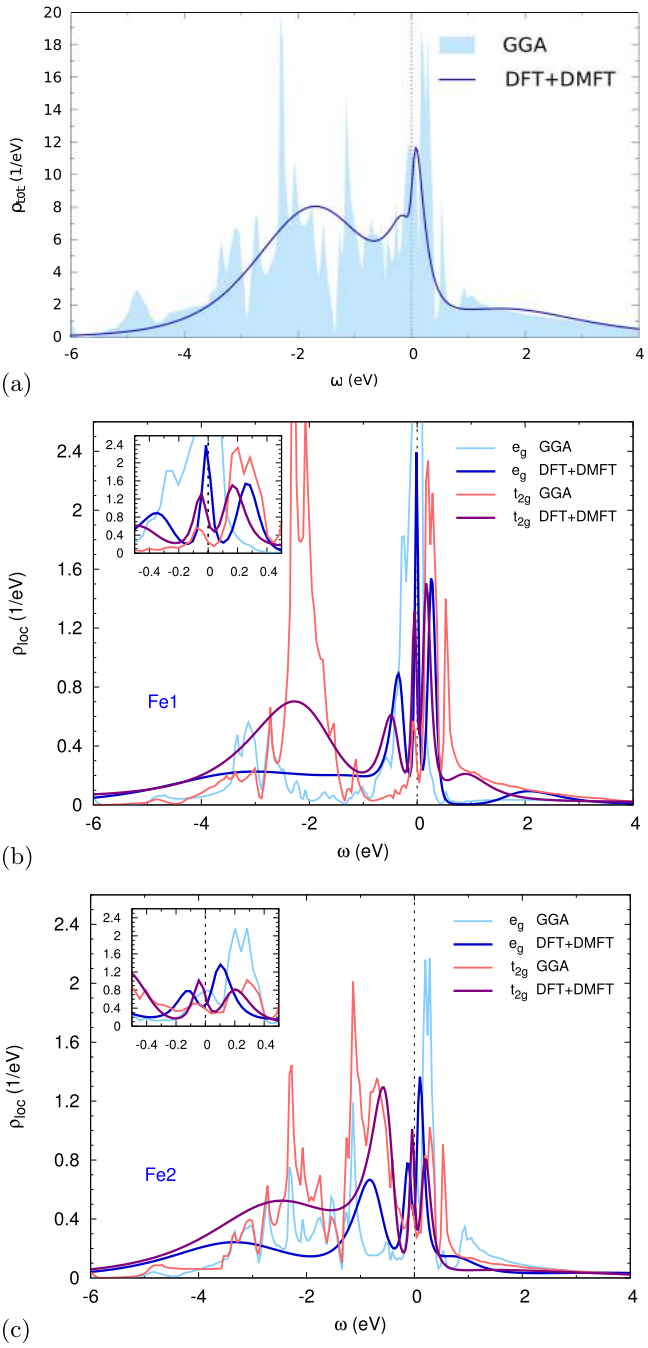

FIG. 4. Spectral functions of $D0_3$-Fe_3Al. (a) Total, (b) local Fe1, and (c) local Fe2. Insets in (b) and (c) are low-energy blowups.

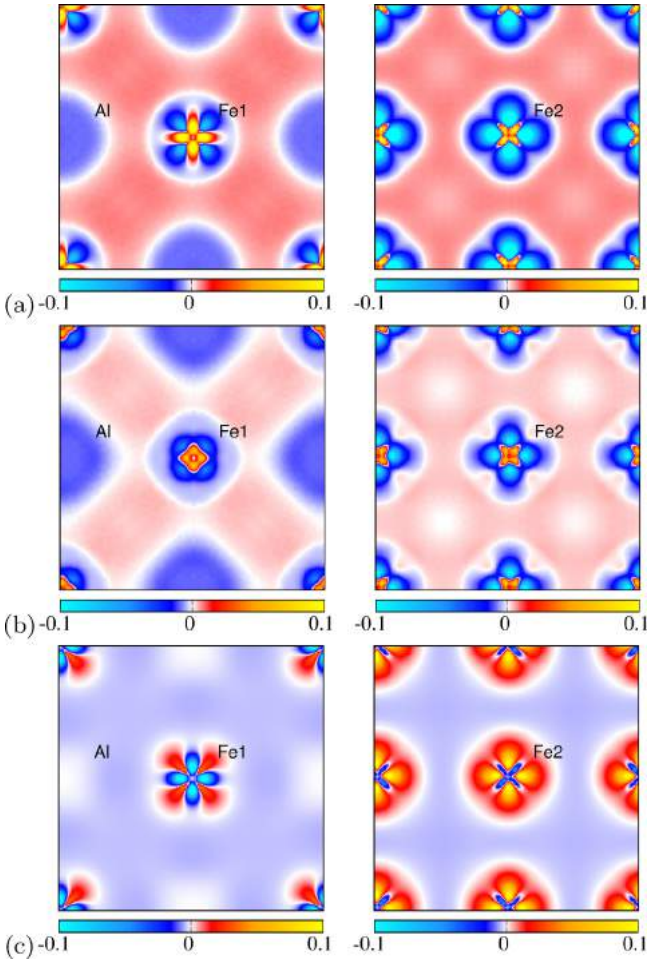

FIG. 5. Relevant charge-density plots in $D0_3$-Fe_3Al around Fe1 (left) and Fe2 (right) with the c axis perpendicular to the plotting plane. (a) GGA bonding charge density (see text). (b) DFT+DMFT bonding charge density. (c) Charge difference $n_{\mathrm{DFT+DMFT}} - n_{\mathrm{GGA}}$.

a more subtle orbital/directional electronic structure around Fe1, whereas Fe2 with its "washed-out" orbital signature looks similar to Fe in the $L1_2$ structure. A strong GGA favoring of e_g character at low energy in the case of Fe1 is weakened in DFT+DMFT, i.e., with correlations there are orbital-balancing tendencies at the Fermi level.

From the electron count, the Fe1(t_{2g}) states become strongly correlation enhanced, while on the other hand, the Fe2(e_g) electrons benefit from a local Coulomb interaction (cf. Table I). In principle, localizing $D0_3$ electrons in effective t_{2g} orbitals is understandable from a charge-repulsion argument due to the orbital direction. Because of the stronger hybridized environment on Fe2 imposed by the nearby Al, the single-site argument is not easily applicable there. Note that the effective e_g filling is leveled out in DFT+DMFT between Fe1 and Fe2. Figure 5 underlines the present findings by inspecting the intra- and intersite charge transfers. The bonding charge density $n^{\mathrm{bond}} \equiv n^{\mathrm{crystal}} - n^{\mathrm{atom}}$ with many-body effects shows, furthermore, a charge depletion in the interstitial bonding region compared to the GGA result. In total, also the Fe sites in the $D0_3$ structure gain $3d$ electrons upon the impact of local Coulomb interactions. While as expected the Fe2 site has a similar filling as the Fe site in $L1_2$, the Fe1 site has a lower electron count by roughly half an electron. Note that the absence of significant Fe filling differences with correlations in the recent work by Galler *et al.* [5] for $B2$-FeAl might be explained by the fact that no charge self-consistent framework was utilized in that study.

Concerning the correlation strength, though the Fe1 site and in general the e_g orbital character has a somewhat lower QP weight, there is neither a striking difference between the two Fe sublattices, nor between the e_g/t_{2g} character. In numbers, an average value of $Z \sim 0.8$ is slightly higher than

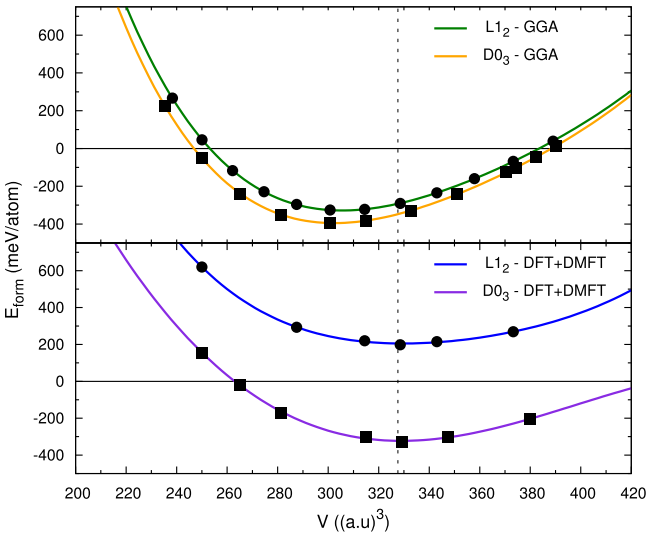

FIG. 6. Comparison of Fe_3Al formation-energy curves for the $D0_3$ and the $L1_2$ structure within NM-GGA and PM-DFT+DMFT. The dashed line marks the experimental equilibrium volume.

for the $L1_2$ structure, marking somewhat weaker correlation effects.

The Fe_3Al compound is not a particularly strongly correlated material, since the ratio of the local Coulomb interaction and the bandwidth is well below unity. In addition, the local Fe occupation ranging between seven and eight electrons is already above the optimal Hund's physics scenario [41–43] of about 5 ± 1 electrons (where, e.g., iron pnictides reside). Still, correlation effects are effective in modifying the charge density and the low-energy character, impacting the bonding properties as well as the charge and spin responses.

2. *Energetics*

We turn now to the structural phase competition between $D0_3$ and $L1_2$, by comparing the formation energy $E_{\rm form}$ per atom with respect to the volume V, i.e.,

$$E^{\rm Fe_3Al}_{{\rm form},m}(V) = E^{\rm Fe_3Al}_{{\rm tot},m}(V) - \tfrac{3}{4}E^{\rm bcc\text{-}Fe}_{{\rm tot},m}(V_{\rm eq}) - \tfrac{1}{4}E^{\rm fcc\text{-}Al}_{{\rm tot},m}(V_{\rm eq}), \quad (2)$$

where $V_{\rm eq}$ marks the respective equilibrium volume of the elemental phase. The additional common index m refers to the fact that each energy is given for the same magnetic state, e.g., NM, PM, or FM. Thus *explicit* magnetic formation/ordering terms do not enter our definition of $E_{\rm form}$. In that respect, the data shown in Fig. 6 are based on NM-GGA and PM-DFT+DMFT calculations. Both numerical schemes designate the $D0_3$ structure correctly as the stable one, with, however, two obvious differences. First, while in the many-body scheme the equilibrium volume is well reproduced, GGA yields a value too small by about 10%. Second, the energy difference $\Delta E^{L1_2}_{D0_3}$ between both structural types is about eight times larger within DFT+DMFT. Furthermore, the bulk modulus B is smaller in the latter scheme.

It was indeed shown in Ref. [11] that the first-principles description of the electronic structure and the phase stability of Fe_3Al is delicate. Upon ferromagnetic order, the $L1_2$ phase is by mistake stabilized in GGA(PBE). In this regard, a detailed data comparison is provided in Table II. While NM-GGA yields the correct qualitative structural hierarchy, the detailed structural data are off the experimental values. On the good side, introducing ferromagnetism on the GGA level brings the lattice constant and bulk modulus close to experiment. However, it not only misleadingly stabilizes the $L1_2$ structure [11], but now strongly underestimates the formation energy. This major difference from the experimental $E^{\rm Fe_3Al}_{\rm form}$ does not appear to be linked solely to the GGA functional, but due to a generally insufficient Kohn-Sham description of the magnetic energy in Fe-Al. Magnetism has been shown to be important for the $D0_3$ alloy ordering in that system [49]. Also in the LDA-based work by Watson and Weinert [50], a value $E^{\rm Fe_3Al}_{\rm form,FM} = -230$ meV/atom was obtained for spin-polarized $D0_3$-Fe_3Al. From the computation of the formation energy of various Fe compounds, the authors there concluded that introducing spin polarization in the Kohn-Sham exchange-correlation functional underestimates the magnetic energy for such alloys.

TABLE II. Comparison of structural data for $D0_3$-Fe_3Al. Formation energy $E_{\rm form}$ (in meV/atom), bulk modulus B (in GPa), lattice constant (in a.u.), and stability against the $L1_2$ structure. The (NM,FM,PM) formation energies are computed using the corresponding (NM,FM,PM) total energy of bcc Fe [cf. Eq. (2)].

	$E_{\rm form}$	B	a	Stable
NM-GGA	-394	218	5.331	✓
FM-GGA	-202	151	5.465	↯
PM-DFT+DMFT	-325	143	5.480	✓
Experiment	-320 ± 20[a]	144[b]	5.473[c]	✓

[a]Reference [44].
[b]Reference [45].
[c]Reference [46].

For comparison, we computed also the formation energy of FM-$D0_3$ within DFT+DMFT. The corresponding value $E^{\rm Fe_3Al}_{\rm form,FM} = -315$ meV/atom differs only slightly from the PM value. Thus the magnetic-ordering energy does not strongly influence the $D0_3$ ordering, when assuming coherent magnetic states. Of course, the *explicit* magnetic-ordering energy $E^{\rm Fe_3Al}_{\rm form,FM} - E^{\rm Fe_3Al}_{\rm form,PM} = -170$ meV/atom is still sizable. Concerning the competition between chemical orderings with PM *or* FM order in the Fe-Al phase diagram, this latter energy is surely relevant. A detailed statistical-mechanics study of this problem is, however, beyond the scope of the present work. For completeness, we provide in Table III the magnetic

TABLE III. Comparison of the Fe magnetic moments in ferromagnetic $D0_3$-Fe_3Al (in μ_B).

	$m_{\rm Fe1}$	$m_{\rm Fe2}$
FM-GGA	2.45	2.12
FM-DFT+DMFT	2.17	1.48
Experiment	2.18,[a] 2.12[b]	1.50,[a] 1.46[b]

[a]Reference [47].
[b]Reference [48].

moments in FM-$D0_3$. While GGA overestimates the local Fe moments, DFT+DMFT once more brings the data in line with experimental findings.

The results of the DFT+DMFT scheme are overall in very good agreement with the available experimental data. Note again that in order to evaluate the formation energy, the bcc Fe problem was of course also treated in DFT+DMFT, respectively, with the same magnetic state m and with identical local Coulomb interactions. Compared to NM-GGA, the less negative E_{form} of the $D0_3$ structure, in better agreement with experiment, matches the reduced bonding strength revealed from the correlated charge densities (cf. Fig. 5). For the case of $L1_2$-Fe_3Al, correlations not only render it much more energetically unfavorable compared to $D0_3$, but its formation energy becomes even positive, marking the compound unstable. This may be explained by the discussed correlation-induced weakening of the xz/yz states with a significant bonding-antibonding nature, compared to the strengthening of the xy and z^2 states. Thus many-body effects beyond conventional DFT do not merely lead to some quantitative changes, but display a *qualitative* effect on the energetics in the Fe-Al system.

The general improvement in the theoretical description of $D0_3$-Fe_3Al underlines not only the importance of electronic correlations, but renders it clear that a faithful description of the paramagnetic state is sufficient to account for the phase-relevant characterization.

B. Fe_2VAl

In the final section, we discuss the electronic structure of the Heusler $L2_1$-Fe_2VAl compound that emerges from $D0_3$-Fe_3Al by replacing the Fe1 sublattice with V atoms.

Figure 7 shows the total and local spectral properties, again by comparing GGA and DFT+DMFT. As in the earlier DFT-based studies [22,23], we find a semimetallic solution in the former Kohn-Sham calculation. A dichotomy is seen by inspecting the transition-metal electron-state characters on the local level. Below the Fermi level the low-energy region is dominated by Fe(t_{2g}) states, while above ε_F there are dominantly V(e_g) states. As expected because of replacing the Fe1 ions, the V site has a more pronounced orbital differentiation. Yet due to the different vanadium valence, the GGA filling is of course only a bit more than half the size of the Fe site.

Note that within DFT+DMFT we utilize the same U and J_H on the Fe and V sites. This choice can be motivated based on the strong intersite hybridizations in the given intermetallic system, leading to a coherent screening that minimizes substantial site differences in the local Coulomb interactions. With correlations, a clear gap structure emerges in the low-energy region, which is only fully realized at lower temperature. A pseudogap signature is obtained at a higher $T = 387$ K. It is notable that the spectral weight is shifted towards the low-energy region to form sharp gap edges. Thus the gap formation is not of obvious single-particle character and has similarities with, e.g., the (pseudo)gap structure in cuprates. Therefore, the insulating state is not of a conventional band-insulating semiconductor type. Measuring the charge gap from the middle of the gap-edge structure, a size $\Delta_g \sim 0.15$ eV is read off at $T = 193$ K. This is in excellent agreement with experimental values for a charge gap in Fe_2VAl [16].

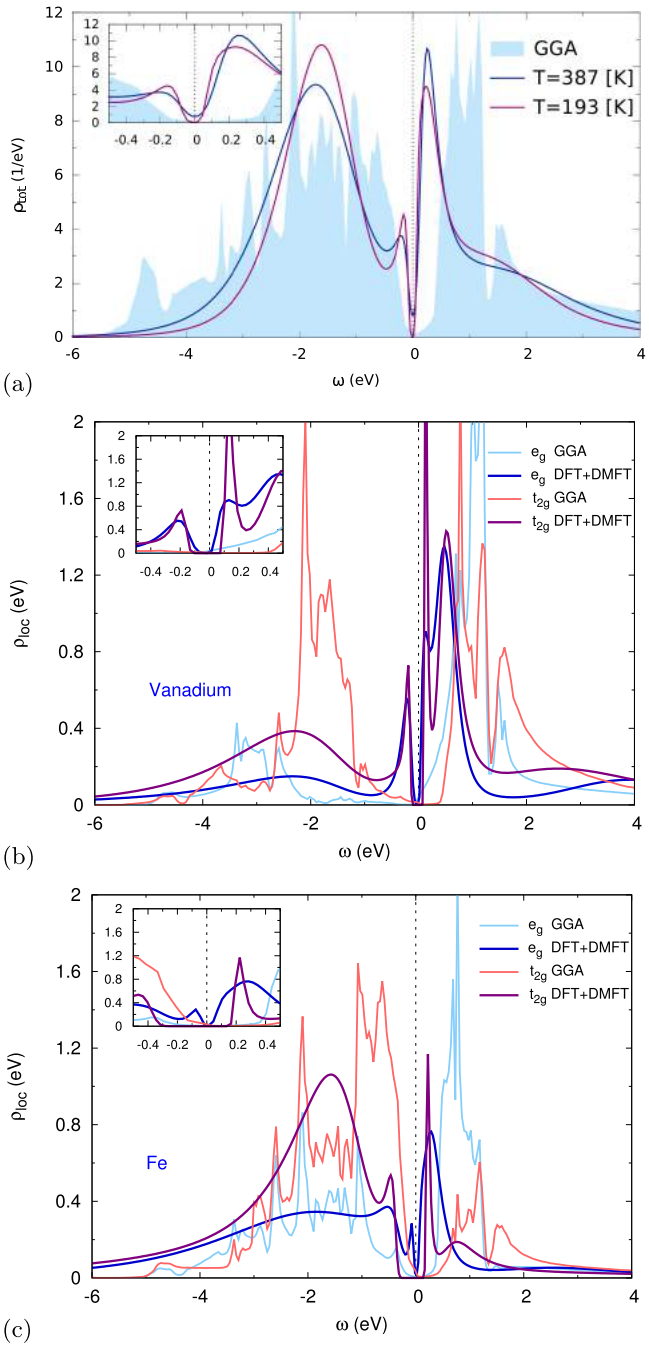

FIG. 7. Spectral function of $L2_1$-Fe_2VAl. Top: Total with DFT+DMFT for two different temperatures. Middle: V local. Bottom: Fe local.

Both transition-metal elements contribute to the intricate gap formation, but the V ion seems to play a more dominant role due to the larger spectral-function enhancement at the gap edges. Moreover, the low-energy spectra with correlations display a more balanced e_g,t_{2g} contribution compared to GGA. This is in line with a nearly orbital-independent local self-energy on the V sites. Therefrom, the correlation strength is enhanced on the latter sites in comparison to the Fe sites,

TABLE IV. Projected local-orbital occupations in Fe_2VAl for $T = 387$ K. The first rows are GGA, and the second rows are DFT+DMFT results, respectively.

		e_g		t_{2g}			
		x^2-y^2	z^2	xz	yz	xy	Total
$L2_1$	V	0.45	0.45	0.97	0.97	0.97	3.81
		0.70	0.70	0.90	0.90	0.90	4.10
	Fe	1.09	1.09	1.65	1.65	1.65	7.13
		1.45	1.45	1.72	1.72	1.72	8.06

yet the vanadium-based QP weight $Z \sim 0.7$ is again moderate. Needless to say, Fe_2VAl is of course no Mott insulator. Still, electronic correlations beyond conventional DFT are at the origin of the gap formation and gap opening. In this context, the different electron fillings of V and Fe are interesting (see Table IV). While the Fe ion unsurprisingly shows a very similar filling characteristic as the Fe2 ion in $D0_3$-Fe_3Al, the V ion already surely differs in the number of valence electrons. With an effective filling close to four electrons, the V site lies one hole below half filling, i.e., in a designated Hund's metal regime [41–43]. The orbital-resolved V occupations align somewhat in DFT+DMFT, however, it seems that the overall correlation strength due to the given sizes of the bandwidth and local Coulomb interactions is still too weak to drive very strong Hund's physics. But unconventional spin fluctuations could nonetheless play a relevant role in the enhanced experimental specific heat [19].

V. CONCLUSIONS

Recently, there have been various investigations that employ realistic DMFT approaches beyond Kohn-Sham DFT($+U$) to elemental iron and its alloy with aluminum. Studies on phase stabilities in the Fe phase diagram [51,52], on the α-Fe phonon spectrum [53], on vacancy formation in α-Fe [54], and on the magnetism in $B2$-FeAl [4,5] were performed. The present work adds a DFT+DMFT examination of the Fe_3Al and Fe_2VAl correlated electronic structure.

We show that although both compounds do not fall in the standard category of strongly correlated systems, more subtle many-body effects are still relevant for a correct description. The energetics and phase stability of Fe_3Al build upon such effects, by providing an improved value for the formation energy with a clear energy separation to the $L1_2$ structure. Note that the charge self-consistent version of the DFT+DMFT framework is important to elucidate such physics. Thereby, not only do local changes on the explicitly correlated lattice sites matter, but the overall charge redistributions including also the interstitial and ligand regions are crucial. On general grounds for cubic intermetallics, the open bcc lattice seems more adequate for correlated (Fe-based) compounds. For systems on a close-packed fcc lattice with sizable local Coulomb interactions, the local correlations become comparatively too strong, weakening important bonding properties. So, fcc-based compounds such as, e.g., Ni_3Al and Cu_3Au either do not display substantial *local* correlation physics or are well described in standard DFT. We want to note that the issue of chemical disorder is surely relevant concerning the phase stabilities close to the Fe_3Al composition of the Fe-Al phase diagram [55]. Treating such additional degrees of freedom together with the correlations encountered here beyond DFT is a formidable task which has to be faced in the future for a detailed thermodynamic understanding of Fe-Al.

The Fe_2VAl compound manifests an intriguing twist to traditional intermetallics, in the sense that the material is derived from the well-known Fe_3Al metal but displays an intricate gap opening reminiscent of (pseudo)gap physics observed in correlated oxides. The DFT+DMFT gap size and its sensitivity to temperature are in excellent agreement with experimental results for this compound. Since also Hund's physics may play a role on the vanadium site, this example shows how easily traditional material physics may be confronted with challenging mechanisms from strongly correlated matter. In a future work, addressing the thermoelectric properties of Fe_2VAl on the basis of the results established here would be highly interesting.

ACKNOWLEDGMENTS

We thank D. Grieger and M. Obermeyer for helpful discussions. This research was supported by DFG-FOR1346. Computations were performed at the University of Hamburg and at the North-German Supercomputing Alliance (HLRN) under Grant No. hhp00026.

[1] K. Miyatani and S. Iida, J. Phys. Soc. Jpn. **25**, 1008 (1968).
[2] B. I. Min, T. Oguchi, H. J. F. Jansen, and A. J. Freeman, J. Magn. Magn. Mater. **54–57**, 1091 (1986).
[3] P. Mohn, C. Persson, P. Blaha, K. Schwarz, P. Novák, and H. Eschrig, Phys. Rev. Lett. **87**, 196401 (2001).
[4] A. G. Petukhov, I. I. Mazin, L. Chioncel, and A. I. Lichtenstein, Phys. Rev. B **67**, 153106 (2003).
[5] A. Galler, C. Taranto, M. Wallerberger, M. Kaltak, G. Kresse, G. Sangiovanni, A. Toschi, and K. Held, Phys. Rev. B **92**, 205132 (2015).
[6] C. S. Lue, Y. Öner, D. G. Naugle, and J. H. Ross, Jr., Phys. Rev. B **63**, 184405 (2001).
[7] Z. Jagličić, S. Vrtnik, M. Feuerbacher, and J. Dolinšek, Phys. Rev. B **83**, 224427 (2011).
[8] M. Fallot, Ann. Phys. (Paris) **6**, 305 (1936).
[9] C. S. Wang, B. M. Klein, and H. Krakauer, Phys. Rev. Lett. **54**, 1852 (1985).
[10] P. Bagno, O. Jepsen, and O. Gunnarsson, Phys. Rev. B **40**, 1997(R) (1989).
[11] F. Lechermann, F. Welsch, C. Elsässer, C. Ederer, M. Fähnle, J. M. Sanchez, and B. Meyer, Phys. Rev. B **65**, 132104 (2002).
[12] F. Lechermann, M. Fähnle, B. Meyer, and C. Elsässer, Phys. Rev. B **69**, 165116 (2004).

[13] B. L. Gyorffy, A. J. Pindor, J. Staunton, G. M. Stocks, and H. Winter, J. Phys. F: Met. Phys. **15**, 1337 (1985).
[14] I. A. Abrikosov, A. V. Ponomareva, P. Steneteg, S. A. Barannikova, and B. Alling, Curr. Opin. Solid State Mater. Sci. **20**, 85 (2015).
[15] Y. Nishino, M. Kato, S. Asano, K. Soda, M. Hayasaki, and U. Mizutani, Phys. Rev. Lett. **79**, 1909 (1997).
[16] C. S. Lue and J. H. Ross, Jr., Phys. Rev. B **58**, 9763 (1998).
[17] H. Okamura, J. Kawahara, T. Nanba, S. Kimura, K. Soda, U. Mizutani, Y. Nishino, M. Kato, I. Shimoyama, H. Miura *et al.*, Phys. Rev. Lett. **84**, 3674 (2000).
[18] J. W. Allen, B. Batlogg, and P. Wachter, Phys. Rev. B **20**, 4807 (1979).
[19] C. S. Lue, J. H. Ross, Jr., C. F. Chang, and H. D. Yang, Phys. Rev. B **60**, R13941(R) (1999).
[20] Y. Nishino, S. Deguchi, and U. Mizutani, Phys. Rev. B **74**, 115115 (2006).
[21] M. Mikami, S. Tanaka, and K. Kobayashi, J. Alloys Compd. **484**, 444 (2009).
[22] D. J. Singh and I. I. Mazin, Phys. Rev. B **57**, 14352 (1998).
[23] R. Weht and W. E. Pickett, Phys. Rev. B **58**, 6855 (1998).
[24] D. I. Bilc and P. Ghosez, Phys. Rev. B **83**, 205204 (2011).
[25] D. Do, M.-S. Lee, and S. D. Mahanti, Phys. Rev. B **84**, 125104 (2011).
[26] S. Y. Savrasov, G. Kotliar, and E. Abrahams, Nature (London) **410**, 793 (2001).
[27] L. V. Pourovskii, B. Amadon, S. Biermann, and A. Georges, Phys. Rev. B **76**, 235101 (2007).
[28] D. Grieger, C. Piefke, O. E. Peil, and F. Lechermann, Phys. Rev. B **86**, 155121 (2012).
[29] S. G. Louie, K. M. Ho, and M. L. Cohen, Phys. Rev. B **19**, 1774 (1979).
[30] B. Meyer, C. Elsässer, F. Lechermann, and M. Fähnle, FORTRAN 90 Program for Mixed-Basis-Pseudopotential Calculations for Crystals (unpublished).
[31] A. N. Rubtsov, V. V. Savkin, and A. I. Lichtenstein, Phys. Rev. B **72**, 035122 (2005).
[32] P. Werner, A. Comanac, L. de' Medici, M. Troyer, and A. J. Millis, Phys. Rev. Lett. **97**, 076405 (2006).
[33] O. Parcollet, M. Ferrero, T. Ayral, H. Hafermann, I. Krivenko, L. Messio, and P. Seth, Comput. Phys. Commun. **196**, 398 (2015).
[34] P. Seth, I. Krivenko, M. Ferrero, and O. Parcollet, Comput. Phys. Commun. **200**, 274 (2016).
[35] J. P. Perdew, K. Burke, and M. Ernzerhof, Phys. Rev. Lett. **77**, 3865 (1996).
[36] B. Amadon, F. Lechermann, A. Georges, F. Jollet, T. O. Wehling, and A. I. Lichtenstein, Phys. Rev. B **77**, 205112 (2008).
[37] V. I. Anisimov, D. E. Kondakov, A. V. Kozhevnikov, I. A. Nekrasov, Z. V. Pchelkina, J. W. Allen, S.-K. Mo, H.-D. Kim, P. Metcalf, S. Suga *et al.*, Phys. Rev. B **71**, 125119 (2005).
[38] M. Aichhorn, L. Pourovskii, V. Vildosola, M. Ferrero, O. Parcollet, T. Miyake, A. Georges, and S. Biermann, Phys. Rev. B **80**, 085101 (2009).
[39] K. Haule, C.-H. Yee, and K. Kim, Phys. Rev. B **81**, 195107 (2010).
[40] M. Karolak, T. O. Wehling, F. Lechermann, and A. I. Lichtenstein, J. Phys.: Condens. Matter **23**, 085601 (2011).
[41] P. Werner, E. Gull, M. Troyer, and A. J. Millis, Phys. Rev. Lett. **101**, 166405 (2008).
[42] K. Haule and G. Kotliar, New J. Phys. **11**, 025021 (2009).
[43] L. de' Medici, J. Mravlje, and A. Georges, Phys. Rev. Lett. **107**, 256401 (2011).
[44] P. D. Desai, J. Phys. Chem. Ref. Data **16**, 109 (1987).
[45] G. Simmons and H. Wang, *Single Crystal Elastic Constants and Calculated Aggregated Properties* (MIT Press, Cambridge, MA, 1971).
[46] W. B. Pearson and G. H. Vineyard, *A Handbook of Lattice Spacings and Structures of Metals and Alloys* (Pergamon, Oxford, UK, 1958).
[47] S. J. Pickart and R. Nathans, Phys. Rev. **123**, 1163 (1961).
[48] D. Satula, L. Dobrzyński, A. Malinowski, K. Szymański, and J. Waliszweski, J. Magn. Magn. Mater. **151**, 211 (1995).
[49] J. Kudrnovský, V. Drchal, L. Bergqvist, J. Rusz, I. Turek, B. Újfalussy, and I. Vincze, Phys. Rev. B **90**, 134408 (2014).
[50] R. E. Watson and M. Weinert, Phys. Rev. B **58**, 5981 (1998).
[51] I. Leonov, A. I. Poteryaev, V. I. Anisimov, and D. Vollhardt, Phys. Rev. Lett. **106**, 106405 (2011).
[52] L. V. Pourovskii, T. Miyake, S. I. Simak, A. V. Ruban, L. Dubrovinsky, and I. A. Abrikosov, Phys. Rev. B **87**, 115130 (2013).
[53] I. Leonov, A. I. Poteryaev, V. I. Anisimov, and D. Vollhardt, Phys. Rev. B **85**, 020401(R) (2012).
[54] P. Delange, T. Ayral, S. I. Simak, M. Ferrero, O. Parcollet, S. Biermann, and L. Pourovskii, Phys. Rev. B **94**, 100102(R) (2016).
[55] B. Sundman, I. Ohnuma, N. Dupin, U. R. Kattner, and S. G. Fries, Acta Mater. **57**, 2896 (2009).

Four

Oxygen - vacancy rutile - based TiO_2

The TiO_2 compound has a very prominent role in condensed matter physics, both from a fundamental as well as from a possible technological point of view.

Most widely used are the three thermodynamically stable crystal structures: rutile, anatase and brookite. Of these forms, rutile TiO_2 is the most stable [BHM$^+$87] and of most interest.

The oxygen vacancy (V_O) is a very important point defect in TiO_2, which has been widely investigated both by theoretical calculations and experimental characterizations. It influences the absorption of water and other molecules on TiO_2 surfaces in photocatalytic devices [STL$^+$01]. The main phases encountered at room temperature are Ti_2O, TiO, Ti_2O_3, Ti_3O_5 and TiO_2. In addition, in between Ti_3O_5 and TiO_2 a series of Ti_nO_{2n-1} phases can be found. This is the Magneli series of homologous compounds [KO97, Ard94] where physical properties are changed dramatically, ranging from metallic to insulating depending on n. The formation of such reduced oxide phases can be described in terms of the elimination of a plane of oxygen atoms [Ard94].

The stoichiometric titanium dioxide with the rutile structure is a wide band - gap semiconductors with the band gape size of 3.06 eV [PCM78]. Values of the band - gap depend on the crystallographic direction. Kofstad [Kof67, Kof72] has proposed that doubly - charged vacancies and interstitial titanium ions with three or four charges may occur as point defects in the rutile crystal. The valence

band consists of O 2p states and the conduction band is formed of Ti 3d states [HG94]. Many theoretical papers have been devoted to the study of the electronic structure, and the physico - chemical properties of nonstoichiometric rutil [ERW05], [CHA$^+$06], [AKN$^+$06], [IBG07], [JVR$^+$10]. An overview of band structure calculations for TiO_2 is given in [Can03, Tan03]. In the studies mentioned above different DFT calculation techniques (e.g FLAPW, PAW) have been used. The results of electronic structure calculations of wide - band semiconductors in this works yields bad agreement with experiments. We have seen that, in terms of band structure calculations, the DFT tends to underestimate band gaps, the Hartree - Fock method always overestimates band gaps.

In our work we perform a realistic many - body study of the impact of oxygen vacancies in rutile TiO_2, both in the regime of lower- and higher - concentrations, based on a combination of density functional theory with dynamical mean - field theory in a charge self - consistent manner. Contrary to Kohn - Sham - based DFT, an isolated oxygen vacancy (V_O) in TiO_2 is insufficient for metallization of the system in the regime of low temperatures. The results of DFT + DMFT provide also both shallow and deep levels (in - gap) for oxygen - defficient TiO_2, known from experiments. Both bandlike levels are connected in the many - body sense, like a lower Hubbard band and a renormalized quasiparticle state, thus become localized due to site - dependent electronic correlations. In a semiconducting phase, we find an in - gap state at $\epsilon_{IG} \sim$ -0.75, which is in excellent agreement with various experiments, e.g. an absorption peak in reduced semiconducting TiO_2 single crystals at 0.75 eV was observed in optics measurements [CG51, Cro52]. By a variation of the correlated subspace the Coulomb interactions on the Ti sites mostly regulate the contrast between itinerancy and localization. The localized states at the V_O show a different occupation and energy state when excited. In the case of a higher oxygen vacancy concentration, the stabilization of a correlated metal occurs in the Magneli phase. The orbital - resolved character and the spectral properties are significant different

for a V_O - defect rutile structure of equal stoichiometry. Even with the proven importance of the charge disproportionation in the oxygen - deficient compounds, metal - insulator transitions driven or supported by charge are not detected.

Oxygen - vacancy driven electron localization and itinerancy in rutile - based TiO_2

F. Lechermann, W. Heckel,O. Kristanovski, and S. Müller
Physical Review B **95**, 195159 (2017).

The reference numbering used in this reprinted article is only valid within this specific article.

Oxygen-vacancy driven electron localization and itinerancy in rutile-based TiO_2

Frank Lechermann,[1,2] Wolfgang Heckel,[2] Oleg Kristanovski,[1] and Stefan Müller[2]
[1]*I. Institut für Theoretische Physik, Universität Hamburg, D-20355 Hamburg, Germany*
[2]*Institut für Keramische Hochleistungswerkstoffe, Technische Universität Hamburg-Harburg, D-21073 Hamburg, Germany*
(Received 16 March 2017; published 30 May 2017)

Oxygen-deficient TiO_2 in the rutile structure as well as the Ti_3O_5 Magnéli phase is investigated within the charge self-consistent combination of density functional theory with dynamical mean-field theory. It is shown that an isolated oxygen vacancy (V_O) in titanium dioxide is not sufficient to metallize the system at low temperatures. In a semiconducting phase, an in-gap state is identified at $\varepsilon_{IG} \sim -0.75$ eV in excellent agreement with experimental data. Bandlike impurity levels, resulting from a threefold V_O-Ti coordination as well as entangled (t_{2g},e_g) states, become localized due to site-dependent electronic correlations. Charge localization and strong orbital polarization occur in the V_O-near Ti ions, the details of which can be modified by a variation of the correlated subspace. At higher oxygen vacancy concentration, a correlated metal is stabilized in the Magnéli phase. A V_O-defect rutile structure of identical stoichiometry shows key differences in the orbital-resolved character and the spectral properties. Charge disproportionation is vital in the oxygen-deficient compounds, but obvious metal-insulator transitions driven or sustained by charge order are not identified.

DOI: 10.1103/PhysRevB.95.195159

I. INTRODUCTION

From two motivating research directions, the investigation of oxygen-deficient transition-metal oxides has gained enormous renewed interest. First, the emerging field of oxide heterostructures leads to questions concerning the impact of oxygen vacancies on interface properties. Since especially the $SrTiO_3$ band insulator marks an important heterostructure building block, elucidating the role of such vacancies in that compound has recently attracted lots of attention [1–7]. Second, on the search of realizing a memristor [8], $TiO_{2-\delta}$ remains a key material [9,10]. Formation and migration of oxygen-vacancy defects are identified to regulate the resistance modulation therein.

Stoichiometric $SrTiO_3$ is characterized as a cubic (perovskite) $Ti^{4+}(3d^0)$ compound with crystal-field split e_g and t_{2g} states (cf. Fig. 1). The band gap is located between the dominant $O(2p)$ and the t_{2g} manifold. Due to the strong $O(2p) - e_g$ hybridization, the creation of an oxygen vacancy (V_O) leads to local $Ti^{3+}(3d^1)$ sites and e_g-dominated in-gap states [1]. The interplay of Ti^{4+}- and Ti^{3+}-like states gives rise to a competition between electron localization and itinerancy, posing an intriguing many-body problem. Recently, that problem was approached by theory within the combination of density functional theory (DFT) with dynamical mean-field theory (DMFT) [5,6,11]. Experiments indeed suggest that V_O's on the surface of strontium titanate as well as in the interface of $LaAlO_3/SrTiO_3$ may be relevant not only for metallicity, but also for emergent magnetic and/or superconducting order.

Oxygen vacancies in TiO_2 pose a related intricate problem, yet with a twist. Besides single-defect scenarios, long-range-ordered vacancy structures provided by the Ti_nO_{2n-1} Magnéli phases [12–14] are an additional point of materials reference. The role of oxygen vacancies in titanium dioxide, with its twofold structural representations of rutile and anatase, is a longstanding problem, and has so far been studied in several theoretical works based on conventional DFT [15], using hybrid functionals [16–20], as well as by treating static electronic correlations within DFT+U [20–24]. Within the latter framework, Mattioli *et al.* [21] originally showed that isolated V_O's in TiO_2 can introduce shallow electronic levels only in anatase, while solely deep localized levels are induced in rutile. The more recent oxygen-deficient rutile studies [18,22,24] suggest an intricate coexistence of shallow and deep levels.

Electronic structure investigations of various Magnéli phases, which may in fact be derived starting from the rutile structure [15], furthermore revealed challenging physics, such as, e.g., metal-insulator transitions and charge ordering [25–27]. But those assessments are so far limited by the possibilities of DFT(+U) to describe electron correlation.

In this work we want to provide a theoretical account of electron correlations in oxygen-deficient rutile-based TiO_2 from a DFT+DMFT perspective. This not only provides a relevant examination of defect-mediated electronic self-energy effects beyond Kohn-Sham exchange-correlation treatments for an oxide compound with high potential for technological applications. It also allows us to compare the characteristics of the induced defect states to, e.g., the ones found in the $SrTiO_3$ perovskite. We show that energy-similar in-gap states are emerging upon creation of V_O's, but metallicity does only occur above a corresponding concentration threshold.

Rutile is known to be the thermodynamically stable TiO_2 phase at all temperatures and pressures [28], while anatase is metastable but can kinetically be stabilized at low temperatures. We therefore restrict the investigation on the rutile structural case of TiO_2 as well as the Ti_3O_5 Magnéli phase as a higher V_O-concentration counterpart.

II. COMPUTATIONAL APPROACH

The supercell defect structures of rutile-$TiO_{2-\delta}$ as well as the Magnéli Ti_3O_5 structure are structurally relaxed [10] on the DFT level within the generalized-gradient approximation (GGA) using the PBEsol [29] functional in the VASP code [30–33].

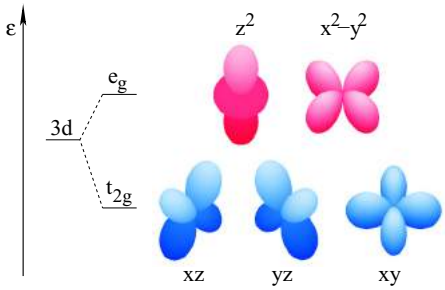

FIG. 1. Crystal-field splitting of a transition-metal $3d$ shell, located in a full-cubic symmetry environment, into t_{2g} and e_g states.

Our present charge self-consistent DFT+DMFT framework [34–36] builds up on the mixed-basis pseudopotential approach [37,38] for the DFT part and the continuous-time quantum–Monte Carlo method [39,40], as implemented in the TRIQS package [41,42] for the DMFT impurity problem. We utilize the GGA in the PBE [43] functional form within the Kohn-Sham cycle.

Locally, threefold effective Ti($3d$) functions define the correlated subspace, which as a whole consists of the corresponding sum over the various Ti sites in the defect problem. Projected-local orbitals [44–48] of $3d$ character provide the effective functions from acting on Kohn-Sham conduction states above the O($2p$)-dominated band manifold. Note that the resulting effective orbitals are not of exclusive t_{2g} or e_g kind, but are defined by the local three-orbital sector lowest in energy, respectively. Each Ti site marks an impurity problem, and the whole number of explicitly treated impurity problems depends on the number of symmetry-inequivalent transition-metal sites in the given supercell. A three-orbital Hubbard Hamiltonian of Slater-Kanamori form, if not otherwise stated parametrized by the Hubbard $U = 5$ eV and the Hund's exchange $J_{\mathrm{H}} = 0.7$ eV, is active on each Ti site. These values for the local Coulomb interactions are in line with previous studies on titanates [49–52]. A double-counting correction of the fully localized form [53] is utilized in this work. The analytical continuation of the finite-temperature Green's functions on the Matsubara axis $i\omega$ to real frequencies is performed via the maximum-entropy method.

Note that we study only paramagnetic states without broken spin symmetry, as well as charge-neutral lattice configurations. Yet possible intersite charge disproportionation is surely allowed.

III. RESULTS

A. Rutile TiO_2

To set the stage for the discussion of oxygen-deficient titanium dioxide, we briefly discuss the electronic structure at stoichiometry. The rutile structure [54] [see Fig. 2(a)] has tetragonal symmetry (space group $P4_2/mnm$) with a ratio $c/a = 0.64$ and the primitive cell comprises two TiO_2 formula units. It consists of corner- and edge-sharing TiO_6 octahedra, such that each oxygen ion is coordinated by three neighboring titanium ions. This is in contrast to common perovskite-based titanates, where the TiO_6 octahedra are exclusively corner sharing and O is twofold Ti coordinated. Of the three rutile

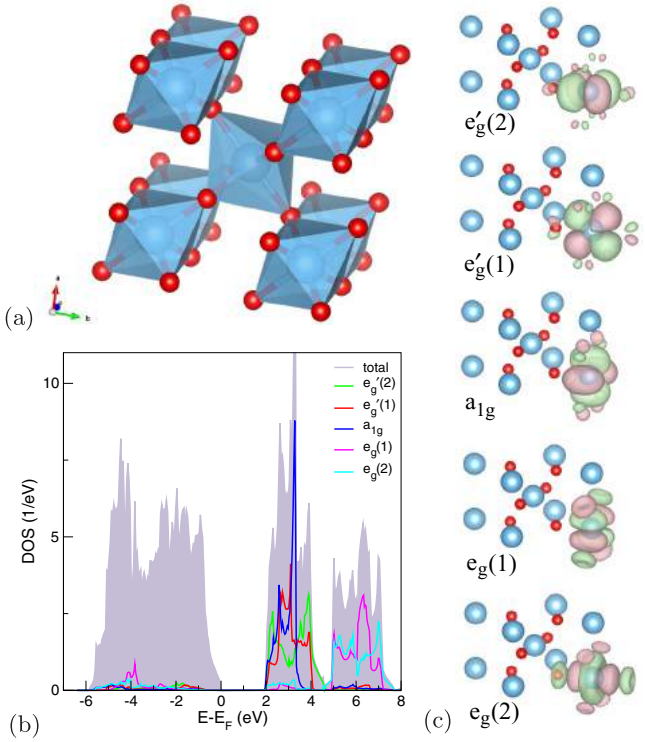

FIG. 2. Characterization of rutile-TiO_2. (a) Crystal structure with Ti (large blue/gray) and O (small red/dark) atoms. (b) Total and local-orbital GGA density of states. (c) Projected local Ti($3d$) orbitals.

minimal Ti-O bond lengths, the two shorter ones are identical in extent. Nominally, titanium is in the Ti^{4+} oxidation state with $3d^0$ occupation.

The given compound is a band insulator with an experimental (optical) band gap of size $\Delta_{\mathrm{g}} \sim 3$ eV [55–57]. Conventional DFT calculations yield a smaller gap $\Delta_{\mathrm{g}} \sim 2$ eV [cf. Fig. 2(b)]. Since TiO_2 is a nominal $3d^0$ material, the HOMO orbitals are of dominant O($2p$) kind and the LUMO orbitals are mainly of Ti($3d_{t_{2g}}$) character, while dominant Ti($3d_{e_g}$) is located at even higher energies above the band gap. Because of the fact that the c axis and the main TiO_6-octahedra axes are locally aligned trigonal, the Ti(t_{2g},e_g) orbitals may be written as linear combinations of cubic harmonics from diagonalization of the orbital-density matrix (see Table I). Due to the local symmetry, the internal (t_{2g},e_g) degeneracies known from the full octahedral group are lifted, respectively. Comparison of the crystal-field levels $\varepsilon_{\mathrm{CF}}$ marks the a_{1g} level as the lowest one:

TABLE I. Titanium $t_{2g} = (e_g'(2), e_g'(1), a_{1g})$ and $e_g = (e_g(1), e_g(2))$ orbitals in TiO_2 with their respective crystal-field level $\varepsilon_{\mathrm{CF}}$ (in meV), expressed in terms of cubic harmonics.

Orbital	$\varepsilon_{\mathrm{CF}}$	$\lvert z^2\rangle$	$\lvert xz\rangle$	$\lvert yz\rangle$	$\lvert x^2-y^2\rangle$	$\lvert xy\rangle$
$\lvert e_g'(2)\rangle$	2684	0.000	0.000	0.000	1.000	0.000
$\lvert e_g'(1)\rangle$	2653	0.000	0.707	0.707	0.000	0.000
$\lvert a_{1g}\rangle$	2574	−0.827	0.000	0.000	0.000	−0.562
$\lvert e_g(1)\rangle$	4398	0.000	−0.707	0.707	0.000	0.000
$\lvert e_g(2)\rangle$	4413	0.562	0.000	0.000	0.000	−0.827

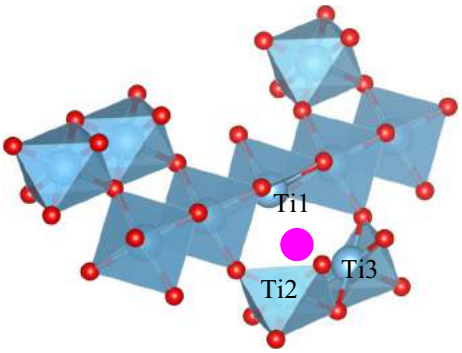

FIG. 3. Structural characterization of an oxygen vacancy (large purple/light gray) in rutile.

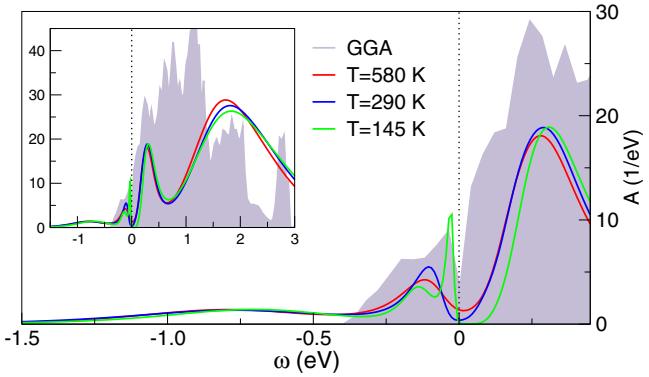

FIG. 4. Total spectral information for rutile-$TiO_{1.9}$ in GGA and DFT+DMFT. at different temperatures in two energy windows.

110 meV below $e'_g(2)$. The t_{2g}-based states are about 2.2 eV lower in energy than the e_g-based ones. Within the effective t_{2g} manifold, which has a bandwidth of about 2.5 eV, the $e'_g(2)$ orbital is designated, since its lobes point along the in-plane tetragonal axes [see Fig. 2(c)].

B. Oxygen vacancy in rutile TiO_2

1. Structural details and correlated subspaces

As shown in Fig. 3, a supercell five times the size of the primitive cell, i.e., with 10 Ti and 20 O atoms, serves as basis structure for the defect study. A single V_O leaves three nearest-neighbor titanium ions behind, here labeled Ti1, Ti2, and Ti3. In the stoichiometric rutile structure, the Ti2-Ti3 distance marks the short side of the given Ti triangle. The nominal V_O concentration in this constellation amounts to $c \equiv \delta/2 = 0.05$, i.e., our modeling describes a $TiO_{1.9}$ defect case. This represents a large V_O concentration, however, not unrealistic for the given system [58]. Table II shows that the interatomic distances are only weakly modified upon structural relaxation, which may be also related to the small supercell size. Still, the obtained pattern describes a shortening of the Ti1-Ti2,3 distances and an elongation of the Ti2-Ti3 bonding, providing a trend to balance the triangle distances through the V_O.

In the following we want to investigate the effect of a V_O in the rutile structure in terms of the local-orbital configuration as well as the net electronic structure. We will discuss two different choices for the correlated subspace. First, in Sec. III B 2, that space is formed by all Ti sites in the given structure, which marks the canonical and ground-state-oriented case. Second, in Sec. III B 3, the correlated subspace is restricted to the contribution of the Ti1-3 sites, i.e., it becomes more local. This second choice may be interpreted as treating an excited state of the system, where electrons do not see the explicit Coulomb repulsion on the remaining Ti sites. Since the $3d$ occupation on the original Ti(d^0) sites distant to the V_O is expected to be small, double occupation is there rather rare. If, moreover, the electrons have gained energy from an excitation process, they can even more easily escape from such double occupations (as well as more efficiently screen the Coulomb penalties). Thus the average effect of local U and J_H on the V_O-distant Ti sites can then be neglected to a good approximation to obtain a rough picture of the present system on a globally higher excitation level. This approximation and interpretation is also not in conflict with the definition of a one-particle spectral function. We thus simply term that space "excited correlated subspace," and this second choice allows us to shed light on possible changes in the oxidation state of the oxygen vacancy. Still note however that the Coulomb interactions on the Ti sites away from the V_O's are crucial to understand the semiconducting character of $TiO_{2-\delta}$, as will be explained in the following Sec. III B 2.

TABLE II. Comparison of the interatomic distances (in Å) between Ti ions surrounding a vacancy-designated oxygen site.

	Ti1 − Ti2	Ti1 − Ti3	Ti2 − Ti3
TiO_2	3.57	3.57	2.96
$TiO_{1.9}$	3.53	3.53	2.97

2. Canonical correlated subspace formed by all Ti sites

Let us start with the well-defined DFT+DMFT setting of the correlated subspace built by all the Ti sites. On the GGA level, as displayed by plotting the total spectral function $A(\omega) = \sum_{\mathbf{k}} A(\mathbf{k},\omega)$ in Fig. 4, the considered system becomes metallic with semimetallic tendencies around the Fermi level ε_F positioned within the t_{2g} manifold. Yet correlations and finite temperature T render the situation more intriguing. At low T the defect structure is semiconducting within DFT+DMFT, with a small charge gap $\Delta \sim 0.06$ eV at $T = 145$ K. That gap is filled with rising temperature, marking a bad-metal regime. In addition, there is sizable transfer of spectral weight to a broad in-gap structure centered at $\varepsilon_{IG} \sim -0.75$ eV. Note that optics measurements detect an absorption peak in reduced semiconducting TiO_2 single crystals at 0.75 eV [55,56], commonly used to explain its blue color [58]. Photoemission measurements on the rutile surface report a defect-state peak at $\sim$−0.9 eV [59–61], while on the anatase surface it is located at a higher energy of $\sim$−1.1 eV [59,62]. Furthermore, scanning tunneling spectroscopy finds an in-gap state at $\sim$−0.7 eV on the defect-rutile surface [63] and x-ray photoelectron spectroscopy on rutile TiO_2 nanoparticles reveals a defect state

TABLE III. Effective V_O-induced orbitals on the three nearby Ti sites in the rutile structure, with their respective crystal-field level ε_{CF} (in meV), written in terms of linear combinations of the original (t_{2g},e_g) functions.

Site	Orbital	ε_{CF}	$\lvert e'_g(2)\rangle$	$\lvert e'_g(1)\rangle$	$\lvert a_{1g}\rangle$	$\lvert e_g(1)\rangle$	$\lvert e_g(2)\rangle$
	$\lvert\psi_1\rangle$	1102	0.035	−0.999	0.000	0.000	−0.002
Ti1	$\lvert\psi_2\rangle$	698	0.000	0.000	−0.147	−0.006	0.990
	$\lvert\psi_3\rangle$	1023	0.000	0.001	0.990	−0.003	0.147
	$\lvert\varphi_1\rangle$	710	−0.032	−0.023	0.837	−0.427	−0.214
Ti2	$\lvert\varphi_2\rangle$	785	0.077	0.073	0.308	0.733	0.473
	$\lvert\varphi_3\rangle$	992	−0.759	−0.642	−0.221	0.096	0.058
	$\lvert\varphi'_1\rangle$	709	0.036	−0.027	0.872	0.437	−0.220
Ti3	$\lvert\varphi'_2\rangle$	780	0.083	−0.079	−0.488	0.726	−0.470
	$\lvert\varphi'_3\rangle$	992	0.758	−0.641	0.018	−0.103	0.063

at ∼−0.8 eV [20]. It is tempting to relate these experimental findings of deep levels in $TiO_{2-\delta}$ to the present satellite peak. On the other hand, n-type conductivity with rather high mobilities due to shallow level has been also reported in the literature [64], which might be connected to our small-gap feature.

To gain insight in the nature and characteristics of the Ti-local states near the V_O, first Table III provides the effective orbitals on Ti1–3 written in terms of linear combinations of the original (t_{2g},e_g) functions from Table I. The φ and φ' orbitals on Ti2,3 behave very similarly; therefore, we restrict the discussion to the φ branch. It is seen that while the ψ_2 orbital has strong e_g character, the orbitals φ_1, φ_2 have sizable contributions from both original orbital sectors. Thereby φ_1 is t_{2g} dominated and φ_2 is e_g dominated. Thus a nearly exclusive e_g character of the local defect states, as, e.g., given in oxygen-deficient $SrTiO_3$ [1,6], does not apply for oxygen vacancies in TiO_2. Note furthermore that the $e'_g(2)$ orbital has almost negligible contribution to the V_O-induced physics, as the $e'_g(2)$-dominated φ_3 orbital remains nearly empty.

Concerning tight-binding parameters, the hopping between both φ_1 on Ti2 and Ti3 is largest with $t_{\varphi_1} = -0.2$ eV, while the other hopping amplitudes on the Ti triangle are of absolute value $\leqslant 0.1$ eV. Not surprisingly, this marks Ti2,3 as more strongly coupled, and thus possibly prone to singlet/triplet formation.

Figure 5 provides the spectra on Ti1–3, which are expected to display (partly) Ti^{3+} character. Note that although all Ti sites in the supercell contribute to the full correlated subspace, electron occupation on the remaining Ti sites is very small. The filling on the Ti sites farther away from V_O is also not significantly raised with temperature. The effective orbitals on Ti2 and Ti3 are nearly equivalent by symmetry and behave here very similarly, so no site differentiation is needed. Of the three correlated orbitals $\{\psi_m\}$ on Ti1, only ψ_2 has sizable filling. Spurious occupation of ψ_1,ψ_3 in GGA is eliminated by correlations. On the contrary, two orbitals, i.e., φ_1 and φ_2, are occupied on Ti2,3. The designation of ψ_2, φ_1, and φ_2 is already suggested from their favorable crystal-field levels (cf. Table III). In DFT+DMFT the occupations read $(n_{\psi_2}, n_{\varphi_1}, n_{\varphi_2}) = (0.65, 0.29, 0.33)$; thus all three Ti sites have similar occupation, however, $n_{\mathrm{Ti1}} > n_{\mathrm{Ti2,3}}$ holds. Since the

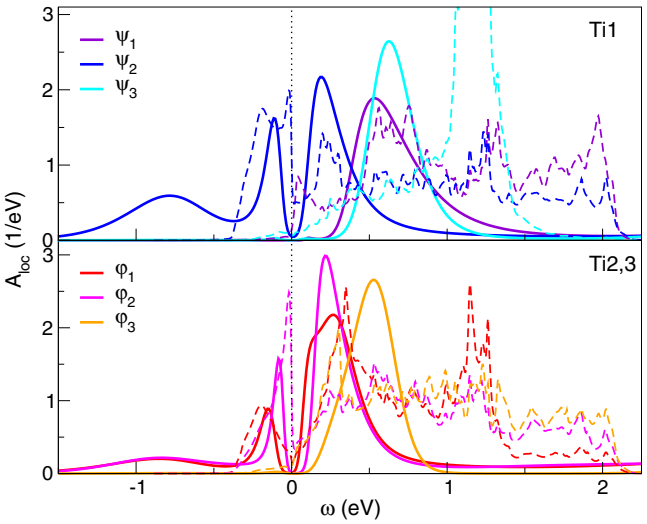

FIG. 5. Local spectral information for rutile-$TiO_{1.9}$ on Ti1 and Ti2,3 (cf. Fig. 3) at $T = 290$ K. Dashed lines correspond to the GGA result, respectively.

site-resolved fillings sum up to $n_{V_O} = 1.89$ and oxygen is in the O^{2-} oxidation state in the compound, the defect is described as being close to the nominal neutral vacancy state V_O^0.

In order to check for the influence of the chosen local Coulomb interactions on the physics, we additionally performed calculations for $U = 3.5$ eV and $U = 2.5$ eV, both with $J_H = 0.5$ eV. The values $U = 3.5$ eV and $J_H = 0.5$ eV were used in a recent DFT+DMFT study of the oxygen-deficient $SrTiO_3$ surface [6]. There are no qualitative differences between the resulting total spectral functions (cf. Fig. 6) for the sets ($U = 5$ eV, $J_H = 0.7$ eV) and ($U = 3.5$ eV, $J_H = 0.5$ eV); hence the detected physics is rather stable within a reasonable range of local Coulomb-interaction parameters. Only at much smaller $U = 2.5$ eV do the semiconducting gap as well as the deeper in-gap state seem to disappear.

It remains to specify the likely mechanism behind the DFT+DMFT finding. The results suggest that the V_O provides electron doping by initially forming rather shallow states below the original t_{2g} mainfold. Because of the higher O-Ti connectivity and the entangled (e_g,t_{2g}) defect signature

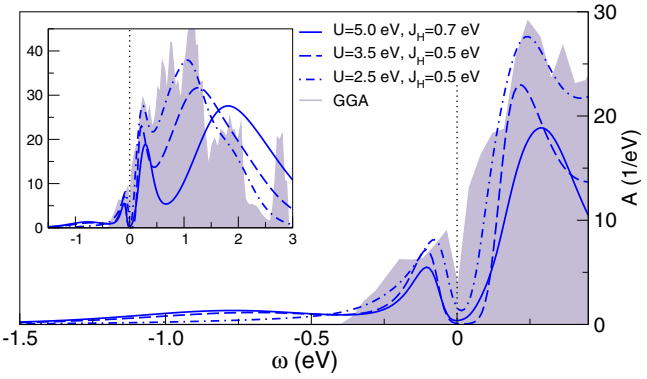

FIG. 6. Total spectral function for rutile $TiO_{1.9}$ based on three different sets of local Coulomb interactions at $T = 290$ K.

in rutile, both compared to, e.g., surface $SrTiO_3$ [6], the coherency of those states is increased and they seemingly develop bandlike character. Sizable Coulomb interactions then lead to a Mott criticality, resulting in band renormalization and formation of Hubbard(-like) bands. The latter give rise to the deep-level in-gap spectra. Importantly, the driving force between the Mott(-like) gap formation is different from a conventional correlated multiband lattice problem. Since the local states near the V_O are connected between different V_O's by fragile hopping paths, mainly the local Coulomb interactions on the Ti sites distant from the defects are determinative for driving the doped system again insulating. In other words, the "interstitial" Coulomb-repulsive region between the V_O's destroys the fragile bandlike defect states and localizes the electrons dominantly near the oxygen vacancy.

3. *Excited correlated subspace formed by Ti1, Ti2, and Ti3*

Letting only the sites Ti1–3 contribute to the correlated subspace serves our goal. First, it gives access to a possibly different V_O charging state. Second, it provides a check for our presented mechanism, denoting the Coulomb interactions on Ti away from V_O as being mainly to be blamed for the semiconducting character.

In general, the states V_O^0, V_O^{+1}, and V_O^{+2} are discussed for oxygen-deficient TiO_2 [18,22,24,65], which in other works appeared relevant to fit findings of shallow-donor properties and well-localized defect states within a coherent picture. As discussed in Sec. III B 2, the present DFT+DMFT study already provides means to such a coexistence by revealing small-gap as well as deeper in-gap features. Nonetheless, by performing additional calculations within the local-restricted correlated subspace one may learn further details of the V_O energy-level structure. Note that in principle the local Coulomb interactions also change when the correlated subspace is modified, i.e., in the present scenario should be lowered for the smaller subspace. But for simplicity we keep $U = 5$ eV and $J_H = 0.7$ eV on Ti1–3 to reveal the key features of the excited system.

As expected, a metallic solution results from the calculation, with reduced and shifted incoherent weight at higher energy [see Fig. 7(a)]. This is indeed in favor of our "interstitial Coulomb" mechanism being relevant for fully localizing electrons near V_O's. Interestingly, the Ti1–3 sites now display a rather different local filling in the dominant orbitals, namely $(n_{\psi_2}, n_{\varphi_1}, n_{\varphi_2}) = (0.24, 0.19, 0.43)$, and a total filling of these sites amounting to $n_{V_O} = 1.56$. This means that in the excited scheme not only the total filling of Ti close to V_O is substantially reduced compared to the canonical scheme, but also the local filling symmetry is different. Now the Ti2,3 sites are majorly occupied and the Ti1 site plays the weaker role, also visualized by plotting the local spectral functions in Fig. 7(b). The high-energy, incoherent, and strongly localized part of the spectra is now dominantly carried by states on Ti2,3. It appears that in the excited-system calculation, localized charge on Ti1 has been partially transferred to itinerant states.

These findings are indeed reminiscent of the identification of different V_O charging states in DFT+U and/or DFT hybrid-functional studies [18,22,24]. Also the characterization of two different site-orbital levels has been reported before,

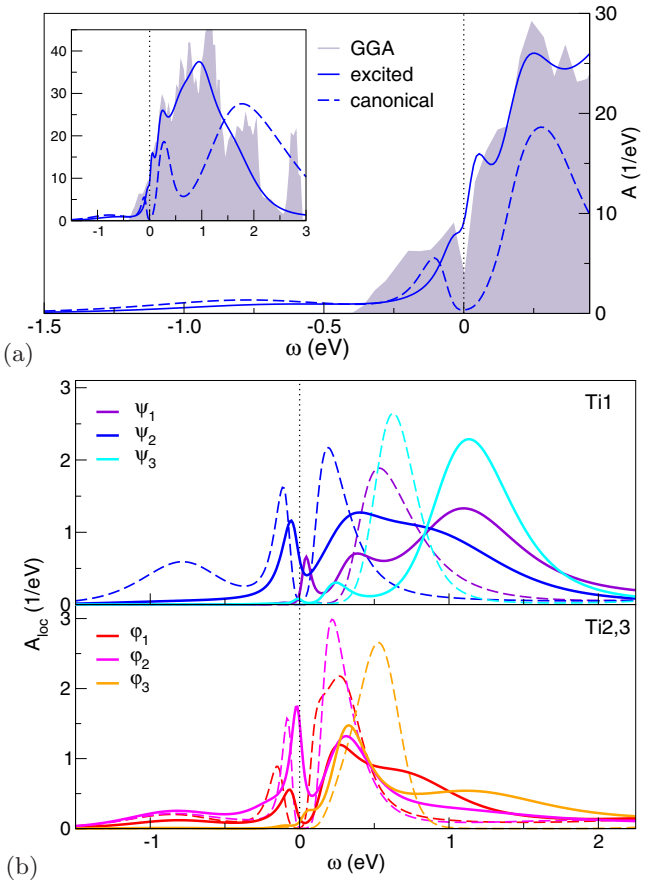

FIG. 7. Comparison of spectral information for rutile-$TiO_{1.9}$ using the canonical and the excited correlated subspace at $T = 290$ K. (a) Total spectral function. (b) Local spectra for Ti1 and Ti2,3 (cf. Fig. 3) at $T = 290$ K; full lines: excited; dashed lines: canonical.

yet usually by invoking explicit magnetic ordering. Our two detected charging states with $n_{V_O}^{can} = 1.89$, reading $V_O^{+0.11}$, and $n_{V_O}^{ex} = 1.56$, reading $V_O^{+0.44}$, do not very strongly deviate from the neutral-vacancy case. However, note that highly oxidized states like V_O^{+1}/V_O^{+2} are usually found in the presence of additional trivalent substitutional impurities on the Ti site, such as Fe^{3+} and Cr^{3+} [65]. An established theoretical picture [18] describes the vacancy-defect state as a bound object consisting of V_O^{2+} plus two polarons, rendering it charge neutral again. In principle, one may try to interpret our results also along such lines, since the present filling scenario with Hubbard-like high-energy spectral parts points to a local $S = 1$ spin in the paramagnetic material. On the other hand, as discussed, we do not have to invoke the polaron picture on clear grounds to account for the coexistence of shallow and deep states.

Let us finally note that the overall qualitative picture that we here derived for a single V_O in rutile TiO_2 is believed to be stable against modified structural relaxations, as, e.g., provided by a different (larger) supercell. More dilute V_O cases could still lead to a weakening of the shallow levels in favor of the deep level, with an increase of the semiconducting gap. Within the local-level manifold the subtle details of the energy hierarchy might be affected by structural issues. But

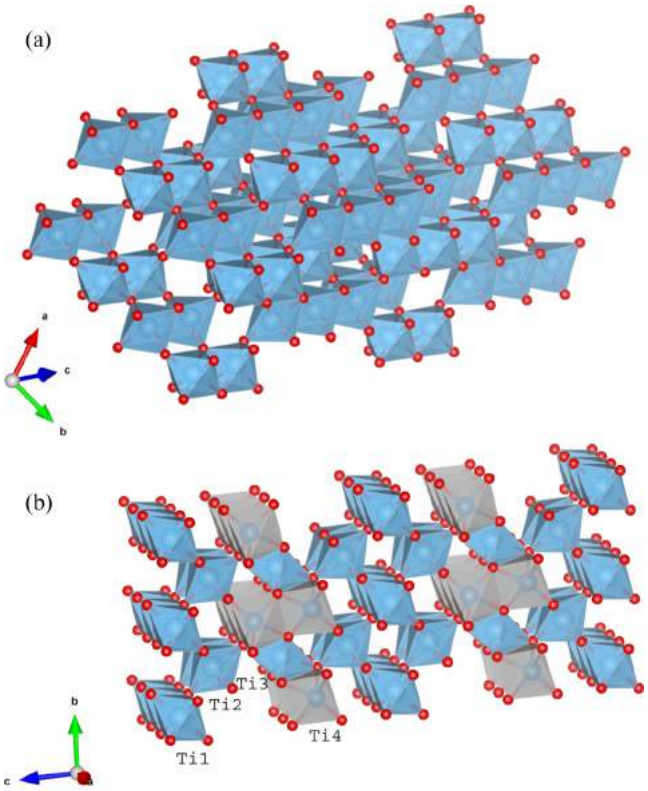

FIG. 8. Illustration of (a) the γ-Ti_3O_5 structure and (b) the defect-rutile Ti_3O_5 structure, both with Ti (large blue/gray) and O (small red/dark) atoms. In (b), the labels Ti1-4 mark symmetry-inequivalent Ti sites, with gray polyhedra surrounding the fivefold coordinated Ti4 sites.

the general notion of the relevant ψ_2 on Ti1 as well as φ_1 and φ_2 on Ti2,3 appears robust.

C. Higher oxygen-vacancy concentration: Ti_3O_5

1. Spectral properties and total energies

We now shift attention to the problem of oxygen vacancies at higher concentration. In order to gain insight in the properties of V_O's in a designated ordered limit, we study a specific Magnéli compound at Ti_3O_5 stoichiometry. There is strong interest in the various Magnéli phases at Ti_3O_5 [12,26,27,66–68], since, e.g., photoreversible phase transitions occur at room temperature. But as we are interested in the main effect of vacancy ordering, we focus on a single allotrop, the so-called γ phase. The underlying crystal structure has monoclinic symmetry and can be stabilized at room temperature [66].

Described in simple terms, whereas perovskite $SrTiO_3$ has corner-sharing TiO_6 octhedra and rutile TiO_2 an elementary alternation of corner- and face-sharing octahedra, the Magnéli phases exhibit more complicated arrangement of those two octahedra-sharing types to accommodate a desired stoichiometry [see Fig. 8(a)]. This may be interpreted as an ordering of vacancies; however, importantly, contrary to, e.g., our $TiO_{1.9}$ structure, there is no V_O-induced "destruction" of local TiO_6 octhedra. In terms of a formal oxygen deficiency δ, the given

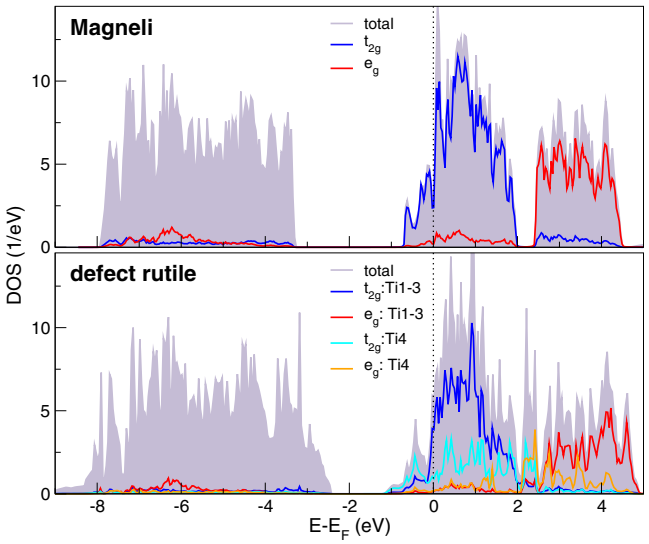

FIG. 9. Comparison of the GGA density of states of γ-Ti_3O_5 (top) and defect-rutile Ti_3O_5 (bottom), in view of (t_{2g},e_g) contributions. The labeling Ti1-3 and Ti4 refers to the sites marked in Fig. 8(b).

Ti_3O_5 stoichiometry amounts nonetheless to $\delta = 0.33$, i.e., the compound would correspond to $TiO_{1.67}$ with vacancy concentration $c = 0.167$.

In order to compare the electronic characteristics of the optimal-ordered Magnéli structure with V_O's in rutile, we in addition performed calculations for defect rutile with stoichiometrty Ti_3O_5. The corresponding crystal structure [cf. Fig. 8(b)] was determined by energy minimization of oxygen-vacancy arrangements at the desired composition by making use of the cluster-expansion technique (see Ref. [10] for details). In this defect-rutile structure, part of the TiO_6 are indeed "damaged," resulting in selected fivefold-O coordinated Ti sites, here designated as Ti4. A total-energy comparison on the GGA level, as expected, clearly favors the Magnéli structure. The more clever restoration of ideal sixfold-oxygen coordination around Ti is appreciated by a substantial ∼0.42 eV per Ti atom against defect rutile.

Figure 9 documents the differences in the GGA density of states in terms of the partitioning in Ti(t_{2g},e_g)-like contributions. Based on the robust TiO_6-octahedral structuring of the Magnéli phase, the electronic structure of γ-Ti_3O_5 shows a clear distinction into those $3d$ submanifolds. This is partly also true for defect-rutile Ti_3O_5, yet the (t_{2g},e_g) states from the TiO_5 polyhedra show there is more substantial overlap in energy. In fact, the small t_{2g}-e_g gap region above 2 eV in γ-Ti_3O_5 just becomes filled by such states in the defect-rutile structure.

The total spectral functions obtained within DFT+DMFT are plotted in Fig. 10. Both systems remain metallic with including many-body correlations. A lower Hubbard band located at ~ -1.1 eV and renormalization at low energy are identified for the Magnéli phase. This marks the system as a seemingly "textbook" correlated material, with coherent renormalized quasiparticles at low energy and incoherent Hubbard bands at higher energies. Already on the GGA level there is a small spectral dip at the Fermi level, verified also

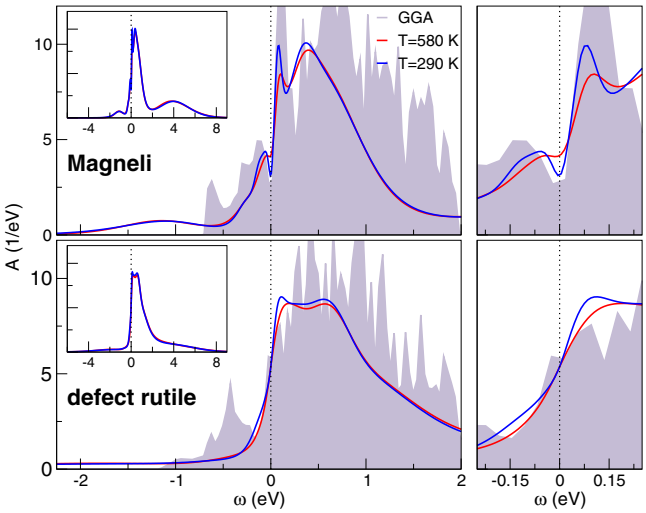

FIG. 10. Comparison of the correlated total spectral function of γ-Ti_3O_5 (top) and defect-rutile Ti_3O_5 (bottom) at two different temperatures.

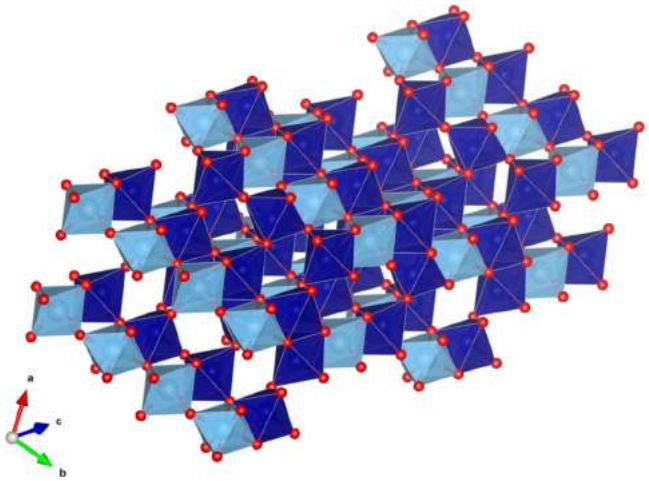

FIG. 11. Effective two-Ti-sublattice representation of γ-Ti_3O_5 (see text). Light(dark) blue octahedra correspond to Ti sites on sublattice 1(2).

with correlations at lower temperature. Note that the Hubbard band is of course nearly exclusively formed by t_{2g}-like states. Satellite structures of t_{2g} kind have recently been detected in a hard x-ray photoelectron spectroscopy study of the structurally different β-Ti_3O_5 and λ-Ti_3O_5 Magnéli compounds [69].

Though the same total filling scenario holds for the defect-rutile phase, the characterization with electronic correlations appears more subtle. First, in view of the semiconducting defect-rutile state discussed in Sec. III B 2, the metallic response at higher V_O concentration is not that surprising. The fragile hopping paths between V_O-near electronic states become increasingly robust with growing concentration of vacancies, such that eventually Coulomb repulsion is not anymore capable of establishing a charge-gapped material. In the low-energy spectrum there is some renormalization due to correlations, but not of a significant kind. On a first glance, the spectral function looks furthermore rather monotonic in the occupied part, yet importantly not necessarily implying that correlations are weak, because the comparison to the GGA results shows there is significant spectral-weight transfer to energies far away from the Fermi level, too. However, this transfer does not give rise to an obvious lower Hubbard-band peak, but is broadly distributed over a wider energy range (see inset of Fig. 10). This finding is somewhat reminiscent of observations made in resonant-photoemission experiments on electron-doped $SrTiO_3$ [70]. There, broader in-gap weight was assigned to the increased relevance of Ti($3d$)-O($2p$) hybridization. Since the e_g character, which is more strongly hybridized with O($2p$) than t_{2g}, plays a more prominent role in the defect-rutile case, the present result could possibly point to a similar interpretation. On the other hand, a recent GW+DMFT study suggests the possibility of diminished satellite peaks in some correlated compounds, as well as a reinterpretation of their original character [71].

The total-energy difference between both Ti_3O_5 structural types is even slightly increasing with including many-body correlations. At room temperature, the Magnéli phase is favored by ∼0.46 eV per Ti atom.

2. *Charge disproportionation between Ti sites*

So far we did not comment on the local occupations of the respective Ti sites in γ- and defect-rutile Ti_3O_5. Since the nominal oxidation state at that stoichiometry amounts to $Ti^{3.33+}$, charge fluctuations are expected to be more relevant than in many other oxides with nominal integer Ti valence. In fact, charge ordering in connection with a metal-insulator transition is commonly discussed for various Magnéli phases, especially for the Ti_4O_7 compound [25].

The oxygen deficiency quite naturally introduces symmetry-inequivalent Ti sites with potentially different electron occupation. Figure 8(b) shows four different Ti sites with especially the Ti4 site surrounded only by five oxygen atoms. The γ-Ti_3O_5 structure formally has eight Ti sites different by symmetry, which were also differently treated in our calculations. In the discussion, however, to a very good approximation, four Ti classes may be grouped to a single effective class, respectively, since the local-orbital structure only marginally differs. Figure 11 displays the present Magnéli structure in that effective two-Ti-sublattice picturing. An obvious pattern is derived therefrom. The TiO_6 octahedra of Ti sites within a given sublattice are corner sharing, whereas the octahedra are edge sharing between both sublattices. Therefore, the intrasublattice Ti-Ti distance is about 0.5 Å longer than the intersublattice pair distance. Both effective sublattices are not of equal-site size, since the Ti2 sublattice (dark-blue octahedra in Fig. 11) covers twice as many Ti sites as the Ti1 sublattice (light-blue octahedra in Fig. 11). Note that the Ti1 octahedra mark the middle of the stoichiometric undisturbed TiO_2 rutile slabs, which consist of three octahedra in the rutile (001) direction and are interrupted by a (121) V_O defect plane.

Tables IV and V provide the Ti($3d$) occupations for both considered Ti_3O_5 structures. Not surprisingly in defect rutile, the charge on the Ti4 sites with fivefold oxygen coordination

TABLE IV. Comparison of the 3*d* filling of the different Ti sites in defect-rutile Ti_3O_5 [see Fig. 8(b) for Ti labeling]. The DFT+DMFT data is taken at $T = 290$ K.

	GGA	DFT+DMFT ($U = 5$ eV)
Ti1	0.22	0.20
Ti2	0.26	0.24
Ti3	0.90	0.86
Ti4	1.15	1.23

is largest, marking that site with a $Ti^{2.8+}$ oxidation state. The nearby Ti3 sites are still close to Ti^{3+}, while Ti1-2 are closer to Ti^{4+}. There are no dramatic differences between the numbers based on GGA and those from DFT+DMFT; only the occupation of Ti4 is still somewhat higher with correlations.

The Magnéli phase γ-Ti_3O_5 has a more subtle Ti ordering. The geometrical constraints of keeping the TiO_6 octahedra in line with the nominal $Ti^{3.33+}$ state leads to slightly different charge states on both effective sublattices. The smaller Ti1 sublattice carries already on the GGA level more charge, with a disproportionation $\rho(\text{Ti1}) - \rho(\text{Ti2}) = 0.11e^-$. Electronic correlations increase this charge splitting only by small amounts, even when invoking a rather large Hubbard $U = 8$ eV. Importantly, the system remains always metallic. Also because a seemingly straightforward Ti^{3+}/Ti^{4+} splitting, as in principle possible in the Ti_4O_7 Magnéli system with a nominal $Ti^{3.5+}$ oxidation state, is not an obvious option. Note, however, that there is also a metal-insulator transition reported for Magnéli Ti_3O_5 [27], but from γ-Ti_3O_5 to δ-Ti_3O_5 upon lowering temperature. Thus further structural changes are in addition indispensable to allow for insulating behavior.

D. Summary and discussion

We presented a detailed first-principles many-body investigation of the effect of oxygen vacancies in rutile TiO_2, both in the lower- and the higher-concentration regime. In the former case, the DFT+DMFT results directly provide the three key ingredients known from experiment for $TiO_{2-\delta}$, namely semiconducting behavior and shallow levels as well as deep levels. Our deep-level (or in-gap) positioning is in excellent agreement with results from various experimental studies. Thereby the many-body perspective provides a different viewpoint on the longstanding discussion of deep vs shallow levels for oxygen-deficient TiO_2. Here, both levels are connected in the many-body sense, similar as a lower Hubbard band and a renormalized quasiparticle state in a conventional moderately correlated metal. Still the correlation-induced gap opening in the bandlike initial shallow levels is not of standard Mott type. Key to the electron localization at low V_O concentration is the Coulomb-repulsion region between defects that blocks the fragile hopping paths. Therefore, the resulting charge gap is rather small and does not scale with U in a conventional way.

TABLE V. Comparison of the 3*d* filling on the two effective sublattices in γ-Ti_3O_5 (see Fig. 11 for Ti-sublattice labeling). The DFT+DMFT data is taken at $T = 290$ K.

	GGA	DFT+DMFT	
		$U = 5$ eV	$U = 8$ eV
Ti1	0.740	0.752	0.766
Ti2	0.630	0.624	0.617

By invoking an excited correlated subspace we brought the semiconducting solution into the transport regime, therewith showing that indeed the Coulomb interactions on the Ti sites distant from the oxygen vacancies dominantly control the competition between itinerancy and localization. Moreover, the localized states at the V_O display a different occupation and energy state upon excitation. This connects our study to other (static-correlation) theory work for $TiO_{2-\delta}$, where, e.g., different V_O charge states and polaron formation are discussed [16–24].

In comparison to oxygen-deficient $SrTiO_3$, the defect-rutile problem differs in two crucial points. First, the defect structure with a V_O in nearest-neighbor distance to three Ti sites, contrary to two Ti sites in the perovskite structure, fosters a modified oxygen-vacancy impact. The higher connectivity with the defect gives way to the formation of more bandlike impurity states on the single-electron level. Second, the higher entanglement between t_{2g} and e_g states lifts the electron dichotomy observed on the $SrTiO_{3-\delta}$ surface [6], suppressing both a decoupled t_{2g} band formation and a rather disconnect straightforward e_g deep-level formation. Therefore, at small V_O concentrations, rutile TiO_2 remains insulating (or semiconducting) due to correlation-induced gap opening in (t_{2g}, e_g)-entangled bandlike impurity levels. Note in this context, however, that the very correlation details of bulk $SrTiO_{3-\delta}$ still need to be investigated by similar means.

In the higher V_O-concentration regime we focused on the Ti_3O_5 stoichiometry, studying the metallic Magnéli γ phase as well as a theory-derived metallic defect-rutile phase. The interplay of Ti coordination and (t_{2g},e_g) electronic structure properties was discussed and therefrom the differences in total energy and in the spectral features explained. While γ-Ti_3O_5 turns out as a "textbook"-like correlated metal, the defect-rutile version displays spectral-weight transfers to higher energies in a much broader (incoherent) fashion. Charge disproportionation is a natural by-product of the V_O ordering in rutile-based TiO_2 (which formally includes the Magnéli phases) [15] and is already captured on the Kohn-Sham level. Electronic correlations beyond the latter provide at least for Ti_3O_5 only minor changes to the Ti charging states.

Although in direct comparison, defect-rutile Ti_3O_5 is energetically rather unfavorable compared to the Magnéli phase, its discussion is nonetheless relevant in view of engineering memristive processes and devices. Since there in TiO_2, transport of V_O's and electrons when starting from the rutile structure is a possible technological aspect. In fact, in realistic close-to-device-like TiO_2 materials, the formation of defect-rutile and Magnéli Ti_nO_{2n-1} phases may happen in parallel within a given material system [9]. Thus understanding the differences between both structural types on a basic level is of crucial importance. In the long run, the present study shall contribute to paving the road for elucidating further engineering options in the interplay between the transport of oxygen vacancies and electrons.

It would also be highly interesting to extend the present investigation to the rutile VO_2 system. As the vanadium ion in the +4 oxidation state has $3d^1$ occupation, it is known that already the stoichiometric system is prone to strong correlation physics [72–76], possibly giving reason to the hallmark metal-to-insulator transition slightly above room temperature [77]. Recent doping studies of VO_2 via oxygen vacancies display opportunities to tune the competition between the metallic and insulating regime [78,79].

Finally coming back to basic features of V_O's in transition-metal oxides, our examination challenges the simplest views on in-gap states, namely the weak-coupling defect-level and the strong-coupling Hubbard-band paradigm. Albeit one encounters features of both original mechanisms in oxygen-deficient TiO_2, as in related systems such as $SrTiO_{3-\delta}$ or the $LaAlO_3/SrTiO_3$ interface, a unique and well-defined picture describing the general nature of defects in transition-metal oxides is still missing. Crystal-field effects, renormalizations, Hubbard-band formation, lifetime effects, *p-d* hybridization, screening, charge transfer, polaron formation, etc. are potentially part of this demanding physics. Thoughts trying to put the problem in an adequate model setting have been put forward from several perspectives, e.g., Ref. [80]. The future task is to cast those into a sound and solid materials-dependent picture.

ACKNOWLEDGMENTS

We gratefully acknowledge financial support from the German Science Foundation (DFG) via SFB986 and through FOR1346. Computations were performed at the University of Hamburg and the JURECA Cluster of the Jülich Supercomputing Centre (JSC) under Project No. hhh08.

[1] W. Luo, W. Duan, S. G. Louie, and M. L. Cohen, Phys. Rev. B **70**, 214109 (2004).
[2] N. Pavlenko, T. Kopp, E. Y. Tsymbal, J. Mannhart, and G. A. Sawatzky, Phys. Rev. B **86**, 064431 (2012).
[3] C. Mitra, C. Lin, J. Robertson, and A. A. Demkov, Phys. Rev. B **86**, 155105 (2012).
[4] J. Shen, H. Lee, R. Valentí, and H. O. Jeschke, Phys. Rev. B **86**, 195119 (2012).
[5] F. Lechermann, L. Boehnke, D. Grieger, and C. Piefke, Phys. Rev. B **90**, 085125 (2014).
[6] F. Lechermann, H. O. Jeschke, A. J. Kim, S. Backes, and R. Valentí, Phys. Rev. B **93**, 121103(R) (2016).
[7] M. Altmeyer, H. O. Jeschke, O. Hijano-Cubelos, C. Martins, F. Lechermann, K. Koepernik, A. F. Santander-Syro, M. J. Rozenberg, R. Valentí, and M. Gabay, Phys. Rev. Lett. **116**, 157203 (2016).
[8] J. J. Yang, D. B. Strukov, and D. R. Stewart, Nat. Nanotechnol. **8**, 13 (2013).
[9] D.-H. Kwon, K. M. Kim, J. H. Jang, J. M. Jeon, M. H. Lee, G. H. Kim, X.-S. Li, G.-S. Park, B. Lee, S. Han *et al.*, Nat. Nanotechnol. **5**, 148 (2010).
[10] W. Heckel, M. Wehlau, S. B. Maisel, T. Frauenheim, J. M. Knaup, and S. Müller, Phys. Rev. B **92**, 214104 (2015).
[11] M. Behrmann and F. Lechermann, Phys. Rev. B **92**, 125148 (2015).
[12] S. Åsbrink and A. Magnéli, Acta Crystallogr. **12**, 575 (1959).
[13] S. Andersson and L. Jahnberg, Ark. Kemi **21**, 413 (1963).
[14] L. A. Bursill and B. G. Hyde, Prog. Solid State Chem. **7**, 177 (1972).
[15] L. Liborio and N. Harrison, Phys. Rev. B **77**, 104104 (2008).
[16] A. Janotti, J. B. Varley, P. Rinke, N. Umezawa, G. Kresse, and C. G. Van de Walle, Phys. Rev. B **81**, 085212 (2010).
[17] P. Deák, B. Aradi, and T. Frauenheim, Phys. Rev. B **86**, 195206 (2012).
[18] A. Janotti, C. Franchini, J. B. Varley, G. Kresse, and C. G. V. de Walle, Phys. Status Solidi RRL **7**, 199 (2013).
[19] D. Berger, H. Oberhofer, and K. Reuter, Phys. Rev. B **92**, 075308 (2015).
[20] G. C. Vásquez, S. Z. Karazhanov, D. Maestre, A. Cremades, J. Piqueras, and S. E. Foss, Phys. Rev. B **94**, 235209 (2016).
[21] G. Mattioli, F. Filippone, P. Alippi, and A. Amore Bonapasta, Phys. Rev. B **78**, 241201(R) (2008).
[22] G. Mattioli, P. Alippi, F. Filippone, R. Caminiti, and A. A. Bonapasta, J. Phys. Chem. C **114**, 21694 (2010).
[23] B. J. Morgan and G. W. Watson, J. Phys. Chem. C **114**, 2321 (2010).
[24] C. Lin, D. Shin, and A. A. Demkov, J. Appl. Phys. **117**, 225703 (2015).
[25] I. Leonov, A. N. Yaresko, V. N. Antonov, U. Schwingenschlögl, V. Eyert, and V. I. Anisimov, J. Phys.: Condens. Matter **18**, 10955 (2006).
[26] A. C. M. Padilha, J. M. Osorio-Guillén, A. R. Rocha, and G. M. Dalpian, Phys. Rev. B **90**, 035213 (2014).
[27] K. Tanaka, T. Nasu, Y. Miyamoto, N. Ozaki, S. Tanaka, T. Nagata, F. Hakoe, M. Yoshikiyo, K. Nakagawa, Y. Umeta *et al.*, Cryst. Growth Des. **15**, 653 (2015).
[28] D. A. H. Hanaor and C. C. Sorrell, J. Mater. Sci. **46**, 855 (2011).
[29] J. P. Perdew, A. Ruzsinszky, G. I. Csonka, O. A. Vydrov, G. E. Scuseria, L. A. Constantin, X. Zhou, and K. Burke, Phys. Rev. Lett. **100**, 136406 (2008).
[30] G. Kresse and J. Hafner, Phys. Rev. B **47**, 558 (1993).
[31] G. Kresse and J. Hafner, Phys. Rev. B **49**, 14251 (1994).
[32] G. Kresse and J. Furthmüller, Phys. Rev. B **54**, 11169 (1996).
[33] G. Kresse and J. Furthmüller, Comput. Mater. Sci. **6**, 15 (1996).
[34] S. Y. Savrasov, G. Kotliar, and E. Abrahams, Nature (London) **410**, 793 (2001).
[35] L. V. Pourovskii, B. Amadon, S. Biermann, and A. Georges, Phys. Rev. B **76**, 235101 (2007).
[36] D. Grieger, C. Piefke, O. E. Peil, and F. Lechermann, Phys. Rev. B **86**, 155121 (2012).
[37] S. G. Louie, K. M. Ho, and M. L. Cohen, Phys. Rev. B **19**, 1774 (1979).
[38] B. Meyer, C. Elsässer, F. Lechermann, and M. Fähnle, Fortran 90 program for mixed-basis-pseudopotential calculations for crystals.
[39] A. N. Rubtsov, V. V. Savkin, and A. I. Lichtenstein, Phys. Rev. B **72**, 035122 (2005).
[40] P. Werner, A. Comanac, L. de' Medici, M. Troyer, and A. J. Millis, Phys. Rev. Lett. **97**, 076405 (2006).

[41] O. Parcollet, M. Ferrero, T. Ayral, H. Hafermann, I. Krivenko, L. Messio, and P. Seth, Comput. Phys. Commun. **196**, 398 (2015).
[42] P. Seth, I. Krivenko, M. Ferrero, and O. Parcollet, Comput. Phys. Commun. **200**, 274 (2016).
[43] J. P. Perdew, K. Burke, and M. Ernzerhof, Phys. Rev. Lett. **77**, 3865 (1996).
[44] B. Amadon, F. Lechermann, A. Georges, F. Jollet, T. O. Wehling, and A. I. Lichtenstein, Phys. Rev. B **77**, 205112 (2008).
[45] V. I. Anisimov, D. E. Kondakov, A. V. Kozhevnikov, I. A. Nekrasov, Z. V. Pchelkina, J. W. Allen, S.-K. Mo, H.-D. Kim, P. Metcalf, S. Suga *et al.*, Phys. Rev. B **71**, 125119 (2005).
[46] M. Aichhorn, L. Pourovskii, V. Vildosola, M. Ferrero, O. Parcollet, T. Miyake, A. Georges, and S. Biermann, Phys. Rev. B **80**, 085101 (2009).
[47] K. Haule, C.-H. Yee, and K. Kim, Phys. Rev. B **81**, 195107 (2010).
[48] M. Karolak, T. O. Wehling, F. Lechermann, and A. I. Lichtenstein, J. Phys.: Condens. Matter **23**, 085601 (2011).
[49] T. Mizokawa and A. Fujimori, Phys. Rev. B **51**, 12880(R) (1995).
[50] E. Pavarini, S. Biermann, A. Poteryaev, A. I. Lichtenstein, A. Georges, and O. K. Andersen, Phys. Rev. Lett. **92**, 176403 (2004).
[51] S. Okamoto, A. J. Millis, and N. A. Spaldin, Phys. Rev. Lett. **97**, 056802 (2006).
[52] F. Lechermann and M. Obermeyer, New J. Phys. **17**, 043026 (2015).
[53] V. I. Anisimov, I. V. Solovyev, M. A. Korotin, M. T. Czyżyk, and G. A. Sawatzky, Phys. Rev. B **48**, 16929 (1993).
[54] J. K. Burdett, T. Hughbanks, G. J. Miller, J. W. Richardson, Jr., and J. V. Smith, J. Am. Chem. Soc. **109**, 3639 (1987).
[55] D. C. Cronemeyer and M. A. Gilleo, Phys. Rev. **82**, 975 (1951).
[56] D. C. Cronemeyer, Phys. Rev. **87**, 876 (1952).
[57] J. Pascual, J. Camassel, and H. Mathieu, Phys. Rev. B **18**, 5606 (1978).
[58] J. C. Parker and R. W. Siegel, Appl. Phys. Lett. **57**, 943 (1990).
[59] A. G. Thomas, W. R. Flavell, A. K. Mallick, A. R. Kumarasinghe, D. Tsoutsou, N. Khan, C. Chatwin, S. Rayner, G. C. Smith, R. L. Stockbauer *et al.*, Phys. Rev. B **75**, 035105 (2007).
[60] S. Wendt, P. T. Sprunger, E. Lira, G. K. H. Madsen, Z. Li, J. Ø. Hansen, J. Matthiesen, A. Blekinge-Rasmussen, E. Lægsgaard, B. Hammer *et al.*, Science **320**, 1755 (2008).
[61] C. M. Yim, C. L. Pang, and G. Thornton, Phys. Rev. Lett. **104**, 036806 (2010).
[62] T. C. Rödel, F. Fortuna, F. Bertran, M. Gabay, M. J. Rozenberg, A. F. Santander-Syro, and P. Le Fèvre, Phys. Rev. B **92**, 041106(R) (2015).
[63] M. Setvin, C. Franchini, X. Hao, M. Schmid, A. Janotti, M. Kaltak, C. G. Van de Walle, G. Kresse, and U. Diebold, Phys. Rev. Lett. **113**, 086402 (2014).
[64] E. Yagi, R. R. Hasiguti, and M. Aono, Phys. Rev. B **54**, 7945 (1996).
[65] S. Yang, L. E. Halliburton, A. Manivannan, P. H. Bunton, D. B. Baker, M. Klemm, S. Horn, and A. Fujishima, Appl. Phys. Lett. **94**, 162114 (2009).
[66] S.-H. Hong and S. Åsbrink, Acta Crystallogr. Sect. B **38**, 2570 (1982).
[67] M. Onoda, J. Solid State Chem. **136**, 67 (1998).
[68] S. Ohkoshi, Y. Tsunobuchi, T. Matsuda, K. Hashimoto, A. Namai, F. Hakoe, and H. Tokoro, Nat. Chem. **2**, 539 (2010).
[69] K. Kobayashi, M. Taguchi, M. Kobata, K. Tanaka, H. Tokoro, H. Daimon, T. Okane, H. Yamagami, E. Ikenaga, and S. I. Ohkoshi, Phys. Rev. B **95**, 085133 (2017).
[70] Y. Ishida, R. Eguchi, M. Matsunami, K. Horiba, M. Taguchi, A. Chainani, Y. Senba, H. Ohashi, H. Ohta, and S. Shin, Phys. Rev. Lett. **100**, 056401 (2008).
[71] L. Boehnke, F. Nilsson, F. Aryasetiawan, and P. Werner, Phys. Rev. B **94**, 201106(R) (2016).
[72] A. Zylbersztejn and N. Mott, Phys. Rev. B **11**, 4383 (1975).
[73] C. Sommers and S. Doniach, Solid State Commun. **28**, 133 (1978).
[74] T. M. Rice, H. Launois, and J. P. Pouget, Phys. Rev. Lett. **73**, 3042 (1994).
[75] S. Biermann, A. Poteryaev, A. I. Lichtenstein, and A. Georges, Phys. Rev. Lett. **94**, 026404 (2005).
[76] O. Nájera, M. Civelli, V. Dobrosavljević, and M. J. Rozenberg, Phys. Rev. B **95**, 035113 (2017).
[77] F. J. Morin, Phys. Rev. Lett. **3**, 34 (1959).
[78] J. Jeong, N. Aetukuri, T. Graf, T. D. Schladt, M. G. Samant, and S. S. P. Parkin, Science **339**, 1402 (2013).
[79] Z. Zhang, F. Zuo, C. Wan, A. Dutta, J. Kim, J. Rensberg, R. Nawrodt, H. Hejin Park, T. J. Larrabee, X. Guan *et al.*, Phys. Rev. Appl. **7**, 034008 (2017).
[80] F. D. M. Haldane and P. W. Anderson, Phys. Rev. B **13**, 2553 (1976).

Five

Double - counting solution: Total energy and structural optimization of pnictide superconductors

The main fundamental problem of the combined DFT + DMFT scheme is the double - counting of the electronic Coulomb interactions, since in DFT calculations there is already a part of local electron - electron interactions in the form of a Hartree contribution and exchange - correlation potential, and the DMFT gives the exact local solution of the Hubbard model. Thus, it becomes clear that to unite the DFT and DMFT, it is necessary to subtract a certain quantity from the DFT of the Hamiltonian in order to avoid double taking into account local interactions. The problem of double - counting is that it was no connection between DFT and DMFT at the microscopic level. The double - counting problem is very important. According the study of [KUW$^+$10] it was shown that the choice of different approaches to "solve" the problem plays a big role and could lead to qualitatively different results.

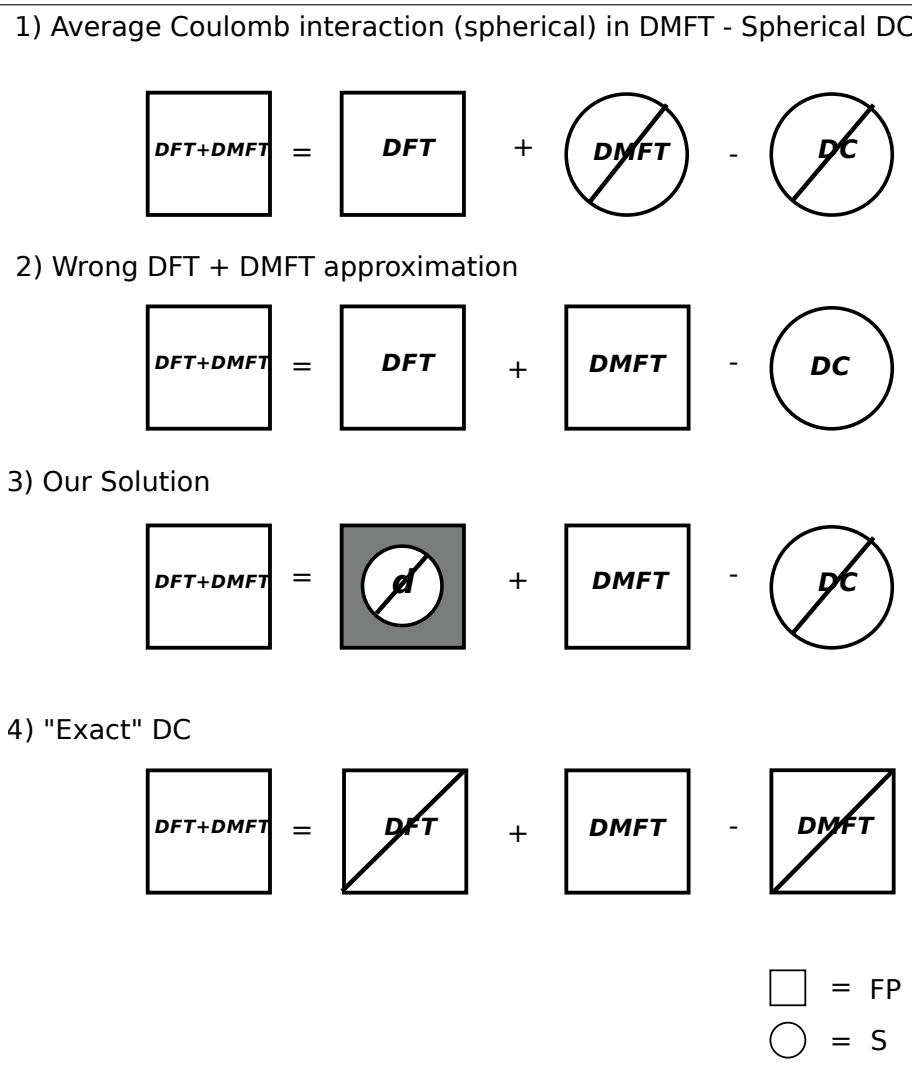

Figure 5.1: Double - counting corrections to the DFT + DMFT method

In the CT - QMC scheme the nonspherical part of local Coulomb interactions could be treated exactly. As shown in Fig. 5.1, the double - counting corrections in a standard DFT + DMFT scheme [KSH+06] are from spherically symmetric treatment (spherical). This spherical correction is able to repair only the average Coulomb interactions either in the DFT or the DMFT parts. As is usually done in the static

mean - field - like DFT + U scheme, the double - counting can be corrected within a substraction of an average Coulomb interaction that is taken either in the limit of itinerant or localized electrons. With the full - potential DFT approach for various structural calculations, this will work just for a stricly spherical type of Hubbard - U correction [DBS$^+$98].

In this work we developed a scheme to avoid a problem of the nonspherical double - counting in a simple way. It was used a traditional DFT + U way of correcting full - potential part of the density functional theory. We make use of our "Mixed - basis pseudopotential" code (MBPP), which electronic charge density ρ(r) consists of three terms. We are interested in the purely local term because the correction is designed to remove the nonspherical contributions between d(f) - orbitals on given site. These contributions are then included in the DMFT part. Thus, we spherically average this local term for those states, which are corrected by DMFT. So, the local nonspherical parts in the purely local charge density do not contribute to the DFT part of the Hartree and exchange - correlation energies. It removes the nonspherical double - counting in the DFT + DMFT total - energy charge self - consistent calculations.

As mentoined above, most of the double - counting formulas were derived by approximating the Hubbard interaction term by some static approximation. It is not clear how to solve the Hubbard model by DFT. But if Luttinger - Ward functionals for the two approximate methods are written side by side in the same form, the intersection of the two is evident. We can either perform the DMFT approximation on the LDA functional, or, the LDA approximation on the DMFT, and in both cases we arrive at the same term, which is counted twice.

In Ref. [Hau15], K. Haule makes use of this Luttinger - Ward functional to develope a new form of the double - counting correction, which is able to derive "exact" overlap between the dynamical mean field theory and density functional theory. This "exact" E_{dc} is free from the nonspherical double - counting (see Fig. 5.1), so it was applied to the structural optimization of the pnictide superconduc-

tor $LaFeAsO$. In our work we have shown that the both double - counting free schemes gives the similar results for structural properties of pnictide superconductor materials, but our scheme can be more useful for practical calculations of crystal - field splitting in f - electron system [DBMP17] than the so - called "exact" double - counting corrections of [Hau15]. This should be carefully check in the future investigations.

Most recently in 2006 superconductivity has been reported in LaFePO, a member of the iron oxypnictides with a $T_c = 3.2$ K [KHH$^+$06]. This group of materials gained much more attention in 2008 when another material of the iron oxypnictides - $LaO_{1-x}F_xAs$ - was reported to be superconducting at a much higher critical temperature of $T_c = 26$ K [KWHH08]. The crystal structure of $LaO_{1-x}F_xAs$ is a tetragonal ZrCuSiAs - type structure (P4/nmm), and is composed of a stack of insulating LaO and conducting FeAs layers. The correct description of the equilibrium structure is particularly important for cases where the forces on the ions are important, e.g., phonon calculations. The magnetic properties show an unusual sensitivity to the internal As position and are aslo sensitive, unusual for localized moments but typical for itinerant magnets, to the exchange - correlation potential.

In general, the structural optimization of LaFeAsO are hard to describe in conventional DFT + DMFT, as shown in previous publications, and we show here that the advanced DFT + DMFT approach can improve thereon.

The simple scheme for avoiding nonspherical double - counting in DFT + DMFT and "exact" double counting makes it possible to reveal Fe - As distance in good agreement with experiment. The standard double - counting scheme in the atomic limit will be useful for strongly correlated d - and f - systems with anisotropic Coulomb interaction close to insulating states. This should stimulate further research on the relevance of many - body effects for structural properties correlated systems.

Role of non - spherical double counting in DFT + DMFT: total energy and structural optimization of pnictide superconductors

O. Kristanovski, A. B. Shick, F. Lechermann, and A. I. Lichtenstein
Physical Review B **97**, 20116(R) (2018).

The reference numbering used in this reprinted article is only valid within this specific article.

Rapid Communications

Role of nonspherical double counting in DFT+DMFT: Total energy and structural optimization of pnictide superconductors

Oleg Kristanovski,[1] Alexander B. Shick,[2] Frank Lechermann,[1] and Alexander I. Lichtenstein[1]
[1]*I. Institut für Theoretische Physik, Universität Hamburg, D-20355 Hamburg, Germany*
[2]*Institute of Physics, Czech Academy of Sciences, Na Slovance 2, CZ-182 21 Prague, Czech Republic*

(Received 23 January 2018; revised manuscript received 8 May 2018; published 31 May 2018)

A simple scheme for avoiding nonspherical double counting in the combination of density functional theory with dynamical mean-field theory (DFT+DMFT) is developed. It is applied to total-energy calculations and structural optimization of the pnictide superconductor LaFeAsO. The results are compared to a recently proposed "exact" double-counting formulation. Both schemes bring the optimized Fe-As interatomic distance close to the experimental value. This resolves the long-standing controversy between DFT+DMFT and experiment for the structural optimization of LaFeAsO.

DOI: 10.1103/PhysRevB.97.201116

I. INTRODUCTION

Recent progress in realistic electronic structure calculations of correlated materials is based on a combination of the density functional theory (DFT) with the dynamical mean-field theory (DMFT) [1,2]. The DFT+DMFT approach opens unique possibilities to investigate the electronic and structural properties of solids with partially filled d- and f-electron shells. The main reason for this success is based on the optimal nature of the local self-energy scheme in the DMFT method [3], and on the development of an efficient multiorbital impurity solver within continuous-time quantum Monte Carlo (CT-QMC) schemes [4].

The ability to treat the nonspherical part of local Coulomb interactions exactly in the CT-QMC scheme brings an additional aspect to the so-called double-counting correction in the DFT+DMFT approach, which is commonly used to account for Coulomb interactions already treated on the DFT level. In a standard DFT+DMFT scheme [1] the double-counting corrections are spherical and are designed to repair only the average Coulomb interactions either in the DFT or the DMFT parts. Usually, as in the static mean-field-like DFT+U scheme, the double-counting correction consists of a subtraction of an average Coulomb interaction that is taken either in the limits of itinerant or localized electrons [5]. With the full-potential DFT approach for different structural calculations, this will work only for a strictly spherical type of Hubbard-U correction [6].

Already in the nonspherical rotationally invariant DFT+U investigations of orbital ordering and structural instability in the $KCuF_3$ perovskite [7], care was taken to avoid full-potential contributions of d electrons in the DFT part. Applications of the rotationally invariant DFT+U scheme to calculations of the complex crystal structure of cuprates [8] and magnetic-anisotropy problems [9] show the importance of accurate treatments of the double-counting corrections.

Another way to solve the problem of the proper DFT+DMFT interface is related to transferring the double-counting corrections to the DFT part, in order to subtract the part of the exchange-correlation energy related to d or f electrons [10]. Recently, a so-called "exact" double-counting correction to the DFT+DMFT scheme employs a similar idea to subtract the exchange-correlation term that corresponds to a local Yukawa-like short-range interaction [11]. It is not clear which scheme is more appropriate for different classes of materials. For instance, a successful application of DFT+DMFT to the complicated problem of the anisotropic Fermi surface of Sr_2RuO_4 [12] used a standard mean-field-like double-counting correction for the itinerant limit.

In this Rapid Communication, we introduce a proper double-counting scheme for the atomic limit and make a comparison with a recent "exact" scheme [11]. As a test case, we choose the problem of structurally optimizing the Fe-As distance in the pnictide superconductor LaFeAsO.

II. METHODOLOGY

In a practical implementation, the total energy of the charge self-consistent DFT+DMFT reads [13,14],

$$E^{\mathrm{DFT+DMFT}} = E^{\mathrm{DFT}}[\rho^{\mathrm{DMFT}}(\boldsymbol{r})] + \sum_{\boldsymbol{k}}\sum_{\nu}\epsilon_{\boldsymbol{k}\nu}\Delta N^{(\boldsymbol{k})}_{\nu\nu} + \langle \hat{H}_{\mathrm{int}}\rangle - E_{\mathrm{dc}}, \quad (1)$$

where E^{DFT} is a standard DFT functional acting on the DMFT charge density ρ^{DMFT}, $\epsilon_{\boldsymbol{k}\nu}$ are the Kohn-Sham (KS) energy eigenvalues, $\Delta N^{(\boldsymbol{k})}$ is the KS occupation matrix correction due to the DMFT self-energy [15], $\langle \hat{H}^{\mathrm{int}}\rangle$ is an expectation value of the Coulomb vertex, and E_{dc} marks the double-counting correction. Equation (1) assumes the use of the Bloch basis in which the kinetic energy operator is diagonal in a basis of the Kohn-Sham eigenstates.

The double-counting correction E_{dc} in Eq. (1) accounts approximately for the mean-field value of the electron-electron interaction, already included in E^{DFT}. Until recently, there was no precise solution for the double counting when utilizing conventional DFT implemented in the local-density or generalized-gradient approximations (LDA or GGA). The most commonly used double-counting correction forms in the

DFT+DMFT scheme are the so-called "fully localized (or atomiclike) limit" (FLL) [7,16]

$$E_{\rm dc}^{\rm (FLL)} = \frac{U}{2}N(N-1) - \frac{J}{2}\sum_{\sigma} N_\sigma(N_\sigma - 1), \qquad (2)$$

or, the "around-mean-field" (AMF) scheme [17,18],

$$E_{\rm dc}^{\rm (AMF)} = U n_\uparrow n_\downarrow + \frac{1}{2}(n_\uparrow^2 + n_\downarrow^2)\frac{2l}{2l+1}(U-J), \qquad (3)$$

where $n_\sigma = {\rm Tr}[n_{m\sigma,m'\sigma}]$, $n = n_\uparrow + n_\downarrow$ is the total d (or f) on-site occupation, and U and J are the intra-atomic Coulomb repulsion and exchange parameters, respectively [19]. This $E_{\rm dc}$ stems from a spherically symmetric treatment, while the DFT part of the Hartree and the exchange-correlation energies,

$$E_{\rm H} + E_{\rm XC} = \frac{1}{2}\int d\vec{r}\,d\vec{r}\,'\frac{\rho(\vec{r})\rho(\vec{r}\,')}{|\vec{r}-\vec{r}\,'|} + \int d\vec{r}\,\rho(\vec{r})\epsilon_{\rm XC}[\rho(\vec{r})], \qquad (4)$$

remain accounted together with the nonspherical contributions into the DFT+DMFT energy functional Eq. (1) (for simplicity, we write everything in terms of a charge density only, while the inclusion of the spin is straightforward).

One way to exclude this "nonspherical" double counting is to keep only the spherically symmetric contributions in the $\langle \hat{H}_{\rm int}\rangle$ term of Eq. (1) [6]. But this is not what one truly aims for, and the DFT+DMFT-induced enhancement of the orbital polarization beyond DFT will be lost.

Alternatively, the nonspherical contributions entering the DFT part of the Hartree and the exchange-correlation energies from the d (or f) states can be excluded in a simple way, similar to what was proposed earlier in DFT+U [20], and DFT+HIA (Hubbard-I approximation) [21,22] implementations of the full-potential linearized augmented plane-wave (FLAPW) method [23].

In this work, we make use of the mixed-basis pseudopotential method (MBPP) [24–27], and expand the KS wave function for the Bloch vector $\boldsymbol{k}$ and band ν into plane waves (pw's) and localized functions (lf's),

$$\psi_{\boldsymbol{k}\nu}(\boldsymbol{r}) = \frac{1}{\sqrt{\Omega_c}}\sum_{\boldsymbol{G}} \psi_{\boldsymbol{G}}^{\boldsymbol{k}\nu}\, e^{i(\boldsymbol{k}+\boldsymbol{G})\cdot\boldsymbol{r}} + \sum_{\gamma lm} \beta_{\gamma lm}^{\boldsymbol{k}\nu}\,\phi_{\gamma lm}^{\boldsymbol{k}}(\boldsymbol{r}), \qquad (5)$$

where Ω_c is the unit-cell volume, $\boldsymbol{G}$ a reciprocal-lattice vector, γ labels an atom in the unit cell, and lm are the usual angular-momentum quantum numbers. The localized functions are given by

$$\begin{aligned} \phi_{\gamma lm}(\boldsymbol{r}) &= i^l\, g_{\gamma l}(r)\, K_{lm}(\hat{\boldsymbol{r}}), \\ \phi_{\gamma lm}^{\boldsymbol{k}}(\boldsymbol{r}) &= \sum_{\boldsymbol{T}} e^{i\boldsymbol{k}\cdot(\boldsymbol{T}+\boldsymbol{R}_\gamma)}\phi_{\gamma lm}(\boldsymbol{r}-\boldsymbol{T}-\boldsymbol{R}_\gamma), \end{aligned} \qquad (6)$$

whereby g is a radial function, and K is a cubic harmonic.

Accordingly, the MBPP electronic charge density $\rho(\boldsymbol{r})$ consists of three terms, i.e.,

$$\rho(\boldsymbol{r}) = \sum_{\boldsymbol{k}\nu} f_{\boldsymbol{k}\nu}|\psi_{\boldsymbol{k}\nu}(\boldsymbol{r})|^2 = \rho^{\rm pw,pw}(\boldsymbol{r}) + \rho^{\rm pw,lf}(\boldsymbol{r}) + \rho^{\rm lf,lf}(\boldsymbol{r}). \qquad (7)$$

For our concerns, the purely local third term $\rho^{\rm lf,lf}$ is of key interest. It is written as

$$\begin{aligned} \rho^{\rm lf,lf}(\boldsymbol{r}) &= \sum_{\boldsymbol{k}\nu} f_{\boldsymbol{k}\nu}\left|\sum_{\gamma lm}\beta_{\gamma lm}^{\boldsymbol{k}\nu}\,\phi_{\gamma lm}^{\boldsymbol{k}}(\boldsymbol{r})\right|^2 \\ &= \sum_{\boldsymbol{T},\gamma lm}\rho_{\gamma lm}^{\rm lf,lf}(r)\,K_{lm}(\hat{\boldsymbol{r}}), \end{aligned} \qquad (8)$$

with $\boldsymbol{r}' = \boldsymbol{r} - \boldsymbol{T} - \boldsymbol{R}_\gamma$, and hence can be understood as an expansion into the cubic harmonics on each site $\boldsymbol{R}_\gamma$.

We spherically average the purely local term $\rho^{\rm lf,lf}$ in Eq. (8) for those states which are corrected by DMFT (with $l = 2$ for the d states, and $l = 3$ for the f states). Thus, the local nonspherical parts in $\rho_\gamma^{\rm lf,lf}$ vanish on each site $\boldsymbol{R}_\gamma$, and do not contribute to the DFT part of the Hartree and the exchange-correlation energies Eq. (4). It removes the nonspherical double counting in the DFT+DMFT total-energy charge self-consistent calculations.

Until recently, there was no exact solution of the double-counting problem. Density functional theory does not have a diagrammatic representation that would provide an explicit identification of the corresponding many-body interaction terms. Also, it is not clear how to solve the Hubbard model by DFT. The FLL/AMF forms of $E_{\rm dc}$, which were discussed above, are derived in some static approximations to the Hubbard interaction term. The "physical" arguments prevailed in the choice of $E_{\rm dc}$.

In Ref. [11], Haule proposed a new "exact" form of the double-counting correction making use of the Luttinger-Ward functional representation for both DFT and DMFT. This $E_{\rm dc}$ was applied to a number of correlated solids, and good agreement between the theory and experiment was achieved. Importantly, the $E_{\rm dc}$ of Ref. [11] is free from the nonspherical double counting, and no additional correction is required. Therefore, we applied it to the structural optimization of the pnictide superconductor LaFeAsO.

III. RESULTS

Electronic structure theory of the high-temperature superconductor LaFeAsO occupies a fundamental place in condensed matter physics and material science. The calculations are often performed either within the DFT or DFT+DMFT. Both approaches fall short in the correct description of the equilibrium crystal structure. When the paramagnetic high-temperature phase is modeled by a nonmagnetic DFT calculation, a too short Fe-As distance, governed by the internal unit-cell parameter z, is obtained. The latter has a drastic influence on the low-energy electronic structure [28], and very precise electron-electron correlation effects need to be tackled. Charge self-consistency within DFT+DMFT becomes important and based thereon, previous studies [29,30] indeed improved upon pure nonmagnetic DFT calculations. However, still, those correlated electronic structure results remain ambiguous, and depend on the choice of the double-counting correction (FLL or AMF).

We overtook the values of Hubbard-$U = 2.7$ eV and Hund's exchange of $J = 0.8$ eV for the local Coulomb interactions from Ref. [29], which were calculated within the

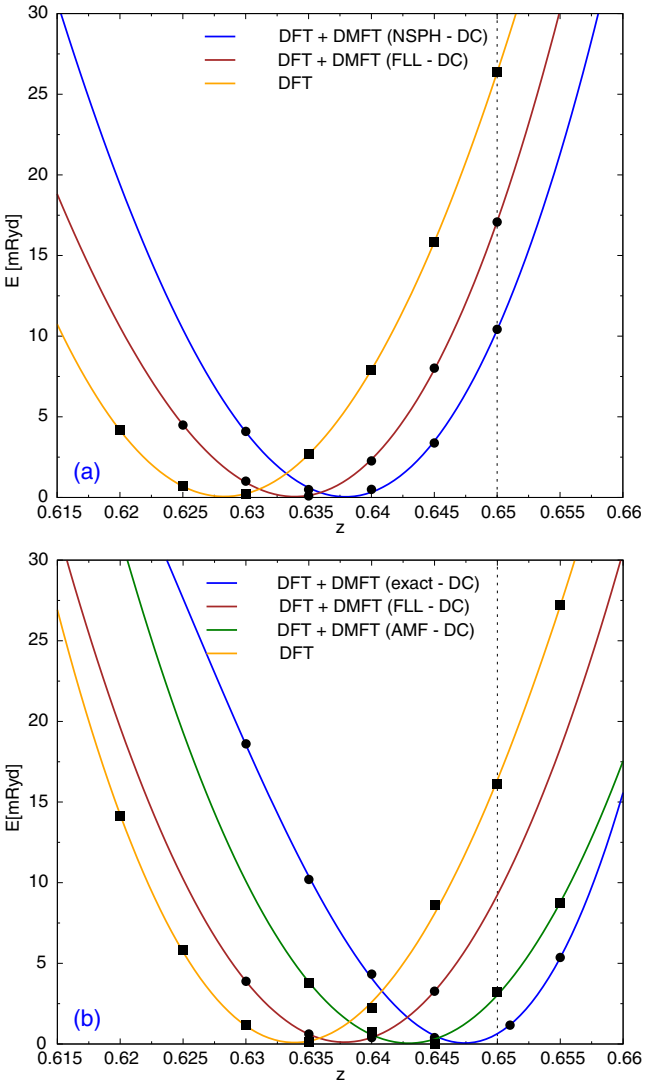

FIG. 1. The relative total energy of LaFeAsO as a function of the As height, expressed by the z parameter, in the unit cell. (a) MBPP based, (b) WIEN2K based (AMF is from Ref. 30). The dashed line marks the experimental z position of the As atom.

constrained random-phase approximation (cRPA) [31,32]. The inverse temperature is set to $\beta = 40\ \mathrm{eV}^{-1}$, which corresponds to room temperature $T = 290$ K. For the solution of the quantum impurity problem we apply the continuous-time hybridization (cthyb)-QMC method [33]. The multiorbital Hubbard Hamiltonian of Slater-Kanamori form, parametrized by Hubbard-U and Hund's exchange J, is applied to the respective full five-orbital $3d$ manifold.

We performed the total-energy electronic structure DFT and DFT+DMFT calculations of LaFeAsO making use of the MBPP method [34] and compared them with WIEN2K calculations [35]. The FLL form of the double-counting correction was used, as well as the exact double counting from Ref. [11]. The total energies within the MBPP-based schemes are shown in Fig. 1(a), and are compared with WIEN2K-based results shown in Fig. 1(b). The values of the As atom z parameter that correspond to the total-energy minima are given in Table I.

TABLE I. Comparison of the As atom z position calculated with different methods and codes.

MBPP	z	WIEN2K	z
DFT	0.628	DFT	0.634
DMFT (FLL)	0.633	DMFT (FLL)	0.638
DMFT (FLL+NSPH)	0.638	DMFT ("exact")	0.648

Both MBPP and WIEN2K DFT calculations yield values for the As atom z parameter that are substantially smaller (see Table I) than the experimental value of $z = 0.651$ [28]. The inclusion of correlation effects by DFT+DMFT (FLL) without the nonspherical (NSPH) double-counting correction has a visible effect on the total energy, and improves the As atom z parameter over the DFT results. This is in agreement with the previous WIEN2K-based DFT+DMFT calculations [29]. Still, the difference $\Delta z = 0.013$ between the experimental and theoretical values remains unresolved.

Note that within an identical setting, DFT and DFT+DMFT calculations based on the pseudopotential (MBPP) method produce z parameter values $\approx$0.005 smaller than the corresponding all-electron (WIEN2K) calculations. Nevertheless, the difference between DFT and DFT+DMFT results obtained with MBPP is the same as from the WIEN2K calculations, and illustrates the important role of electron-correlation effects.

It was proposed in Ref. [30] that a further improvement of the value of $z = 0.643$ can be achieved by switching to the AMF form of E_{dc}, suggesting a partial delocalization of the $3d$ states in metallic LaFeAsO, shown in Fig. 1(b). However, no nonspherical double-counting corrections were used in these calculations. As follows from our MBPP results shown in Fig. 1(a) and Table I, avoiding nonsphericity in the FLL double counting leads to an increase of the z parameter to $z = 0.638$ over the $z = 0.633$ FLL result with no nonspherical double-counting correction. Taking into account that MBPP yields slightly smaller values for the z parameter, the proposed double-counting correction brings the total-energy minimum into close proximity of the experimental data.

Finally, we performed calculations with the exact double-counting implementation [11], and obtained the total-energy minimum at $z = 0.648$ [see Fig. 1(b) and Table I], now shifted close to the experimental value [28]. The accuracy of this implementation, which is free from the nonspherical double counting, for structural optimizations in correlated materials has been validated in a previous study [36]. This supports our finding that the source of discrepancy between experiment and DFT+DMFT is not a form of the double counting due to the metallic character of LaFeAsO, as suggested by Ref. [30], but because of the nonspherical double counting in the DFT and DMFT parts of DFT+DMFT.

To conclude, we developed a simple scheme for avoiding nonspherical double counting in DFT+DMFT and compared with the "exact" double-counting scheme [11]. As a proof of principle, the results show a similar shift in the Fe-As distance and bring results of DFT+DMFT closer to experiments. While the so-called exact double-counting scheme

[11] aims to exclude additional nonspherical contributions from the correlated subspace of DFT numerically, our FLL double-counting scheme forces the removal of double counting from DFT analytically. In the case of the AMF double-counting scheme, due to a simple mean-field nature of the approximation, one can do both flavors of the spherical AMF scheme with analytical DFT subtraction [20] and numerical nonspherical AMF subtraction [12], similar to the rotationally invariant LDA+U method [7]. In this respect, in future investigations it will be very interesting to check more fine effects, for example, the crystal field parameters of transition-metal and rare-earth ions in different crystals. We think that the standard double-counting scheme in the atomic limit will be useful for strongly correlated d and f systems with anisotropic Coulomb interactions close to insulating states.

ACKNOWLEDGMENTS

We thank Kristjan Haule and Eva Pavarini for helpful discussions. Financial support was provided by the Deutsche Forschungsgemeinschaft (DFG) Grants No. DFG LI 1413/8-1 and No. DFG LE 2446/4-1, as well as the Czech Science Foundation Grant No. 18-06240S. Computations were performed at the University of Hamburg and at the North-German Supercomputing Alliance (HLRN) under Grant No. hhp00040.

[1] G. Kotliar, S. Y. Savrasov, K. Haule, V. S. Oudovenko, O. Parcollet, and C. A. Marianetti, Rev. Mod. Phys. **78**, 865 (2006).
[2] D. Vollhardt and A. Lichtenstein, Eur. Phys. J. Spec. Top. **226**, 2439 (2017).
[3] A. Georges, G. Kotliar, W. Krauth, and M. J. Rozenberg, Rev. Mod. Phys. **68**, 13 (1996).
[4] E. Gull, A. J. Millis, A. I. Lichtenstein, A. N. Rubtsov, M. Troyer, and P. Werner, Rev. Mod. Phys. **83**, 349 (2011).
[5] V. I. Anisimov, F. Aryasetiawan, and A. Lichtenstein, J. Phys.: Condens. Matter **9**, 767 (1997).
[6] S. Dudarev, G. Botton, S. Y. Savrasov, W. M. Temmerman, and A. P. Sutton, Planet. Space Sci. **166**, 429 (1998).
[7] A. I. Liechtenstein, V. I. Anisimov, and J. Zaanen, Phys. Rev. B **52**, R5467(R) (1995).
[8] H. Eschrig, K. Koepernik, and I. Chaplygin, J. Solid State Chem. **176**, 482 (2003).
[9] E. R. Ylvisaker, W. E. Pickett, and K. Koepernik, Phys. Rev. B **79**, 035103 (2009).
[10] I. A. Nekrasov, N. S. Pavlov, and M. Sadovskii, JETP Lett. **95**, 581 (2012).
[11] K. Haule, Phys. Rev. Lett. **115**, 196403 (2015).
[12] G. Zhang, E. Gorelov, E. Sarvestani, and E. Pavarini, Phys. Rev. Lett. **116**, 106402 (2016).
[13] L. V. Pourovskii, B. Amadon, S. Biermann, and A. Georges, Phys. Rev. B **76**, 235101 (2007).
[14] I. Di Marco, J. Minar, S. Chadov, M. I. Katsnelson, H. Ebert, and A. I. Lichtenstein, Phys. Rev. B **79**, 115111 (2009).
[15] F. Lechermann, A. Georges, A. Poteryaev, S. Biermann, M. Posternak, A. Yamasaki, and O. K. Andersen, Phys. Rev. B **74**, 125120 (2006).
[16] I. V. Solovyev, P. H. Dederichs, and V. I. Anisimov, Phys. Rev. B **50**, 16861 (1994).
[17] V. I. Anisimov, J. Zaanen, and O. K. Andersen, Phys. Rev. B **44**, 943 (1991).
[18] I. V. Solovyev, A. I. Liechtenstein, and K. Terakura, Phys. Rev. Lett. **80**, 5758 (1998).
[19] V. I. Anisimov and O. Gunnarsson, Phys. Rev. B **43**, 7570 (1991).
[20] A. B. Shick, V. Janis, V. Drchal, and W. E. Pickett, Phys. Rev. B **70**, 134506 (2004).
[21] A. B. Shick, J. Kolorenc, A. I. Lichtenstein, and L. Havela, Phys. Rev. B **80**, 085106 (2009).
[22] P. Delange, S. Biermann, T. Miyake, and L. Pourovskii, Phys. Rev. B **96**, 155132 (2017).
[23] E. Wimmer, H. Krakauer, M. Weinert, and A. J. Freeman, Phys. Rev. B **24**, 864 (1981).
[24] S. G. Louie, K. M. Ho, and M. L. Cohen, Phys. Rev. B **19**, 1774 (1979).
[25] C.-L. Fu and K.-M. Ho, Phys. Rev. B **28**, 5480 (1983).
[26] C. Elsaesser, N. Takeuchi, K. M. Ho, C. T. Chan, P. Braun, and M. Faehnle, J. Phys.: Condens. Matter **2**, 4371 (1990).
[27] B. Meyer, C. Elsässer, F. Lechermann, and M. Fähnle, FORTRAN 90 program for mixed-basis-pseudopotential calculations for crystals.
[28] I. I. Mazin, M. D. Johannes, L. Boeri, K. Koepernik, and D. J. Singh, Phys. Rev. B **78**, 085104 (2008).
[29] M. Aichhorn, L. Pourovskii, V. Vildosola, M. Ferrero, O. Parcollet, T. Miyake, A. Georges, and S. Biermann, Phys. Rev. B **80**, 085101 (2009).
[30] M. Aichhorn, L. Pourovskii, and A. Georges, Phys. Rev. B **84**, 054529 (2011).
[31] T. Miyake, K. Nakamura, R. Arita, and M. Imada, J. Phys. Soc. Jpn. **79**, 044705 (2010).
[32] T. Miyake, L. Pourovskii, V. Vildosola, S. Biermann, and A. Goerge, J. Phys. Soc. Jpn. Suppl. **77**, 99 (2008).
[33] P. Werner, A. Comanac, L. de' Medici, M. Troyer, and A. J. Millis, Phys. Rev. Lett. **97**, 076405 (2006).
[34] D. Grieger, C. Piefke, O. E. Peil, and F. Lechermann, Phys. Rev. B **86**, 155121 (2012).
[35] K. Haule, C.-H. Yee, and K. Kim, Phys. Rev. B **81**, 195107 (2010).
[36] K. Haule and G. L. Pascut, Phys. Rev. B **94**, 195146 (2016).

Six

Magnon dynamics in $CrBr_3$

Recently, the family of two - dimensional materials has been expanded to include ferromagnets. It was shown that CrI_3 exhibited ferromagnetism down to thicknesses of a single monolayer [HCNM$^+$17]. CrI_3 is part of a group of materials known as the chromium trihalides, CrX3 (where X=Cl, Br or I). Here, for the first time, we show that a few layers of exfoliated $CrBr_3$ (2 - 6 layers) are also ferromagnetic by fabricating and characterizing functional tunnelling devices where the $CrBr_3$ layer is sandwiched in between two graphene electrodes. We also report a new type of tunneling mechanism in van der Waals heterostructures by demonstrating that electrons in our device tunnel between the graphene layers via the emission (and, at high temperature, absorption) of magnons in the $CrBr_3$ barrier. The temperature and magnetic field dependence of the magnon spectra were investigated within the self - consistent spin - wave - theory. We modify it to the case of a hexagonal lattice and calculated the magnon density of states in the nearest - neighbor approximation with the exchange integrals taken from the experiment. We have also calculated the density of states, the optical properties, and the exchange parameters with spin - polirization using a the full potential linearized augmented plane - wave (FLAPW) Wien2k code within the generalized gradient approximation (GGA) and experimental crystal structure [BSM$^+$01]. We further investigate the electronic structure and optical properties of $CrBr_3$. As shown in Fig. 6.1 results implies inderect semiconductors. The corresponding value of the band gap are 1.63 eV for

ferromagnetic orientation (1.18 and 1.88 eV for ferromagnetic in each layers with antiferromagnetic orientation between the layers, and antiferromagnetic within the layer respectively).

(a) Total

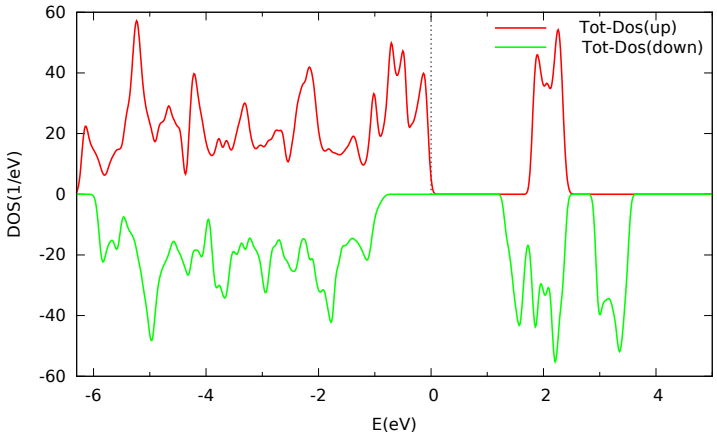

(b) Partial

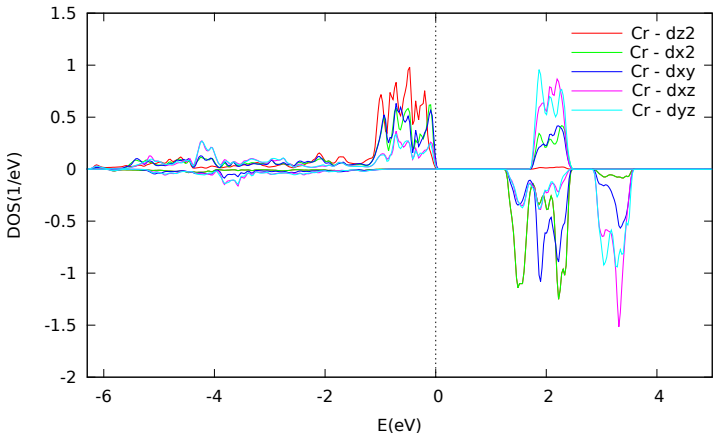

Figure 6.1: Total and partial density of states of $CrBr_3$ for ferromagnetic orientation.

The dielectric functions are only along the z axis different (along the x and y are identical), due to hexagonal symmetry of the lattice. Figure 6.2 shows the imaginary part of the dielectric function for ferromagnetic and antiferromagnetic orintation between the layers. The main peak is contributed by p - d excitation from Br - 3p states of

valence band to Cr - 3d states of lowest conduction band. The satellite states are induced by d - d excitation from occupied 3d and unoccupied states as shown in Fig 6.1(b). We expected a large difference between the values of the dielectric functions along the z axis for the antiferromagnetic and ferromagnetic calculations and a small difference along the x and y axis. Contrary to our expectation, we didn't observe any striking differences, only a small renormalization and a shift of peaks.

(a) xx=yy

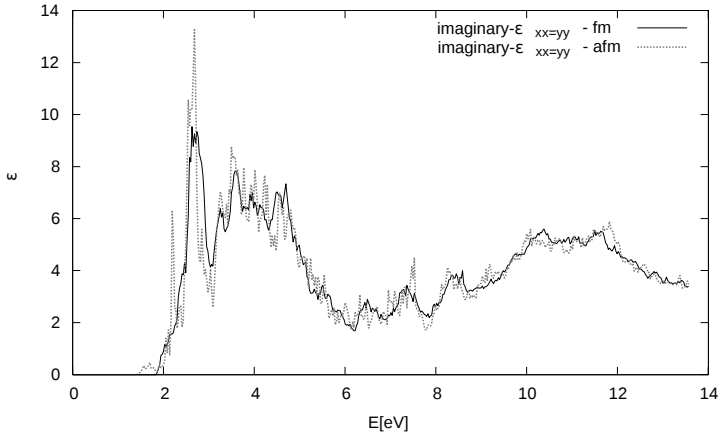

(b) zz

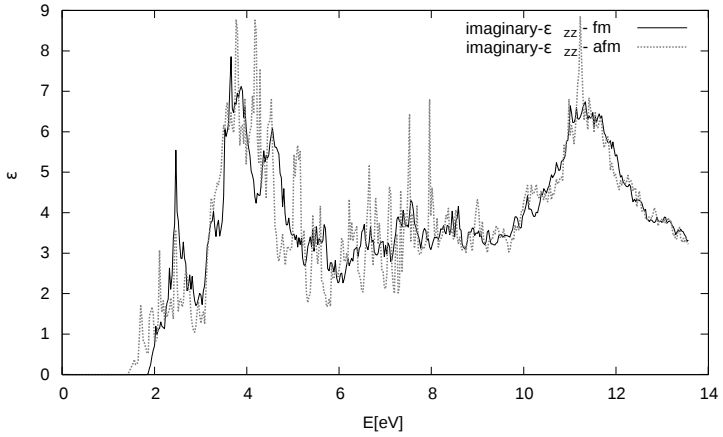

Figure 6.2: Imaginary part of the dielectric function of $CrBr_3$.

To estimate the parameters J (in the plain) and J_L (interlayers) from the total energies from DFT calculations, we consider three different magnetic configurations: ferromagnetic, ferromagnetic in each layers with antiferromagnetic orientation between the layers, and antiferromagnetic within the layer. Using the Heisenberg spin Hamiltonian

$$\hat{H} = -1/2 \sum_{i \neq i} J_{ij} \mathbf{S}_i \cdot \mathbf{S}_j, \tag{6.1}$$

where $\mathbf{S}_i$ denotes the magnetic moment on atom i (which is about S = 3/2 in magnitude), magnetic energies of $CrBr_3$ for each Cr - atom in the cell can be explicitly expressed as:

$$E_H = 2 J_{ij} \mathbf{S}_i \cdot \mathbf{S}_j. \tag{6.2}$$

The results for (12x12x2) k - point mesh are J=0.94meV and J_L = 0.076meV, respectively. The calculated exchange parameters are strong dependet on ineratomic distance. It was confirmed by other calculations which were peformed with the theoretical GGA latice parameters [ZQZL15] instead of the experimental ones (the intralayer exchange J is about 45 % larger than the experimental value [SSSR71]). We chose the experimental values for the calculation of the magnon density of states. The van Hove singularities in the spectrum at 8.5 meV and 17 meV result from the hexagonal symmetry of the $CrBr_3$ lattice. We refer these peaks to the two step - like increases in G observed in the low bias experiment when V_b about 7.5 mV and 17 mV. Announced inelastic neutron scattering investigations of magnons in $CrBr_3$ are in a good agreement with calculated results. At low temperatures and high magnetic fields, a larger shift of the van Hove singularities of $\approx$ 2.4 μ_BB is observed by self - consistent spin wave calculations. It results from magnon - magnon interactions.

The differential conductance depends on the temperature. In the regime of temperatures close to T_C the magnon population is very high, therefore absorption of a magnon by a tunneling electron is more prob-

able. There are no longer a short - range magnetic ordering between the layers and a long - range magnetic ordering within the $CrBr_3$ layer.

The creation of van der Waals heterostructures on the basis of ferromagnetic materials enriches the spectrum of experiments and applications of two - dimensional ferromagnets. Experiments to lift the spin degeneracy of electrons in the layers, and the study of circularly polarised optical emission from these types of structures, are only two examples of possible directions of research in this field. Furthermore, as magnon emission can only occur for a given polarization of the spin of the tunneling electron, only electrons with that particular spin polarization will be able to tunnel. Therefore, our results raise the interesting possibility of using these types of magnetic tunnel barriers for spin injection into two - dimensional materials, a crucial requirement for the development and creation of 2D spintronic devices.

Magnon - assisted tunnelling in van der Waals heterostructures based on $CrBr_3$

D. Ghazaryan, M. T. Greenaway, Z. Wang, V. H. Guarochico - Moreira, I. J. Vera - Marun, J. Yin, Y. Liao, S. V. Morozov, O. Kristanovski, A. I. Lichtenstein, M. I. Katsnelson, F. Withers, A. Mishchenko, L. Eaves, A. K. Geim, K. S. Novoselov, A. Misra
Nature electronics **1**,344 - 349, June (2018).

The reference numbering used in this reprinted article is only valid within this specific article.

ARTICLES
https://doi.org/10.1038/s41928-018-0087-z
nature electronics

Magnon-assisted tunnelling in van der Waals heterostructures based on $CrBr_3$

D. Ghazaryan[1], M. T. Greenaway[2], Z. Wang[1], V. H. Guarochico-Moreira[1,3], I. J. Vera-Marun[1], J. Yin[1], Y. Liao[1], S. V. Morozov[4], O. Kristanovski[5], A. I. Lichtenstein[5], M. I. Katsnelson[6], F. Withers[7], A. Mishchenko[1,8], L. Eaves[1,9], A. K. Geim[1,8], K. S. Novoselov[1,8*] and A. Misra[1,10*]

Van der Waals heterostructures, which are composed of layered two-dimensional materials, offer a platform to investigate a diverse range of physical phenomena and could be of use in a variety of applications. Heterostructures containing two-dimensional ferromagnets, such as chromium triiodide (CrI_3), have recently been reported, which could allow two-dimensional spintronic devices to be developed. Here we study tunnelling through thin ferromagnetic chromium tribromide ($CrBr_3$) barriers that are sandwiched between graphene electrodes. In devices with non-magnetic barriers, conservation of momentum can be relaxed by phonon-assisted tunnelling or by tunnelling through localized states. In contrast, in the devices with ferromagnetic barriers, the major tunnelling mechanisms are the emission of magnons at low temperatures and the scattering of electrons on localized magnetic excitations at temperatures above the Curie temperature. Magnetoresistance in the graphene electrodes further suggests induced spin–orbit coupling and proximity exchange via the ferromagnetic barrier. Tunnelling with magnon emission offers the possibility of spin injection.

The growing family of two-dimensional (2D) materials[1–5] can be used to assemble van der Waals heterostructures with a wide range of properties[6–9]. Expanding the range of available materials to ferromagnetic layered crystals[10–16] would substantially increase the possible functionality of the van der Waals heterostructures. Of particular interest are tunnelling heterostructures[17–20], which have been used to study the electronic states both in the tunnelling barrier and in the emitter and collector contacts[21,22]. The use of ferromagnetic materials as tunnelling barriers can offer novel tunnelling mechanisms where momentum conservation can be fulfilled by magnon[16] emission (unlike in the case of non-ferromagnetic barriers where the tunnelling occurs through emission of a phonon[18,23–25] or via localized states[18,25,26]). In this Article, we investigate electron tunnelling through a thin (2–6 layers) ferromagnetic $CrBr_3$ barrier and demonstrate that magnon-assisted tunnelling offers the possibility of spin-injection, as has previously been demonstrated with other ferromagnetic barriers[27,28].

Device fabrication and characterization

Our devices were assembled on an oxidized silicon wafer by the dry transfer method in an inert atmosphere. The layer structure of our devices is Si/SiO_2/hBN/Gr/$CrBr_3$/Gr/hBN; here, Gr stands for graphene and hBN stands for hexagonal boron nitride (see Fig. 1a). The typical area of the devices is a few tens of square micrometres. We prepared several devices with different numbers $N = 2$, 4 and 6 of $CrBr_3$ monolayers (see Supplementary Fig. 1 for more details on sample fabrication). A tunnel current, I, flows when a bias voltage, V_b, is applied across the two graphene layers. A typical plot of differential conductance $G = dI/dV_b$ is presented in Fig. 1b. The zero-bias conductance depends exponentially on the barrier thickness (see Fig. 1c).

The dependence of G on the applied gate (V_g) and bias voltages for a sample with six $CrBr_3$ monolayers is presented as a colour map in Fig. 1b. In previously studied devices with hBN barriers, the passage of the Fermi level through the zero in the density of states at the Dirac points of the top and bottom graphene electrodes is observed as an X-shaped feature in the colour map[21–23,29], where $G = 0$. This feature is not observed in the devices with a $CrBr_3$ barrier. We attribute this to a high level of doping of the graphene electrodes by the $CrBr_3$.

A magnetic field, $B_\perp$ applied perpendicular to the layers (that is, parallel to the tunnel current) causes the electron spectrum to quantize into a series of Landau levels (LL). In Fig. 1d the Landau quantization is revealed in $G(V_b, V_g)$ as a series of parallel stripes, with a positive slope, due to the passage of the chemical potential through the cyclotron gaps. Only this series of peaks with a positive slope is observed, corresponding to Landau quantization in the lower graphene electrode. The absence of stripes with a negative slope that would arise from LLs in the top electrode indicates that the $CrBr_3$ layer screens the gate voltage-induced electric field, so that the chemical potential in the top graphene layer is unchanged by V_g.

Figure 1b,e reveals a series of step-like increases of the tunnel conductance, with values of V_b that are independent of the gate voltage. These features cannot be associated with any modulation in the density of states of our crystals, as they are absent in our quantum capacitance measurements[30,31] (see Supplementary Fig. 4). This type of behaviour is characteristic of inelastic tunnelling with phonon emission and has been observed previously for Gr/hBN/Gr tunnel

[1]School of Physics and Astronomy, University of Manchester, Manchester, UK. [2]Department of Physics, Loughborough University, Loughborough, UK. [3]Escuela Superior Politécnica del Litoral, ESPOL, Facultad de CNM, Guayaquil, Ecuador. [4]Institute of Microelectronics Technology and High Purity Materials, RAS, Chernogolovka, Russia. [5]Institute of Theoretical Physics, University Hamburg, Hamburg, Germany. [6]Institute for Molecules and Materials, Radboud University, Nijmegen, the Netherlands. [7]College of Engineering, Mathematics and Physical Sciences, University of Exeter, Exeter, UK. [8]National Graphene Institute, University of Manchester, Manchester, UK. [9]School of Physics and Astronomy, University of Nottingham, Nottingham, UK. [10]Department of Physics, Indian Institute of Technology Madras (IIT Madras), Chennai, India. *e-mail: Kostya@manchester.ac.uk; abhishek.misra@iitm.ac.in

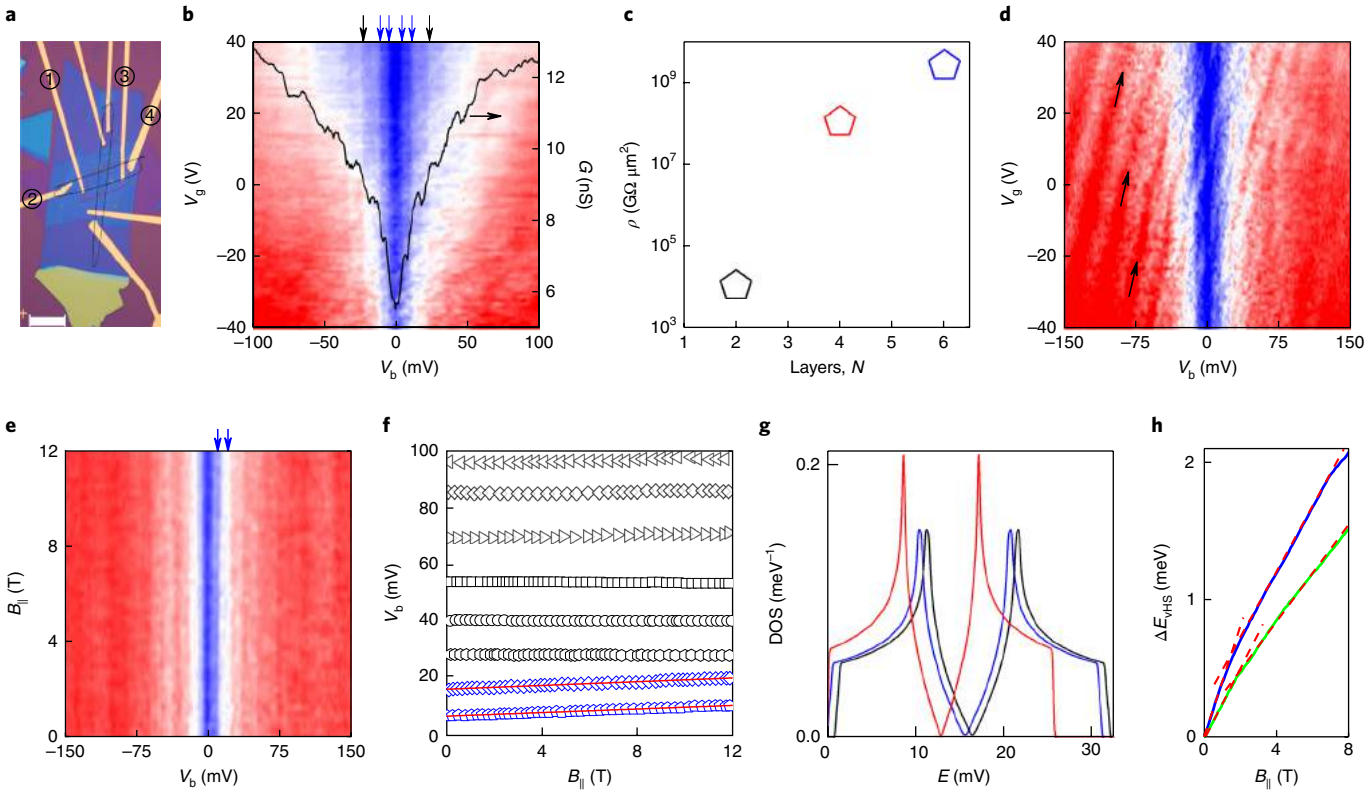

Fig. 1 | Inelastic magnon-assisted tunnelling. a, An optical micrograph of the investigated device. The black and red contours outline the graphene and $CrBr_3$ flakes, respectively. Scale bar, 20 μm. **b**, Zero-field differential tunnelling conductance G dependence on the gate and bias voltages (colour scale is blue to white to red, 6 nS to 11.5 nS to 17 nS) for a 6-layer $CrBr_3$ tunnel barrier device. The black curve is the tunnelling conductance when $V_g = 0$ V. The arrows indicate some of the step-like increase in G that corresponds to inelastic tunnelling with the emission of a magnon (blue arrows) or a phonon (black arrows). **c**, Zero-bias resistivity of junctions with different barrier thicknesses (different colours correspond to different samples). **d**, The same as for **b**, in a perpendicular field of $B_\perp = 12.5$ T. The black arrows correspond to peaks in conductance due to inter-LL tunnelling. The colour scale is blue to white to red, 6 nS to 12 nS to 19 nS. **e**, Differential tunnelling conductance G as a function of $B_\parallel$ and V_b ($V_g = 0$ V). The colour scale is blue to white to red, 6 nS to 12 nS to 19 nS. **f**, Bias position of the step-like features in G as a function of $B_\parallel$. The red lines are the linear fitting with the slopes (from bottom to top) $(5.7 \pm 0.2)\mu_B$, $(5.1 \pm 0.2)\mu_B$. **g**, Calculated magnon density of states for $T = 10$ K, $B = 0$ T (blue line), $T = 10$ K, $B = 6.25$ T (black line), and $T = T_C$, $B = 0$ T (red line). The same calculations provide $T_C = 88$ K. **h**, Calculated changes of the position of the van Hove singularities in magnon density of states (**g**) as a function of magnetic field for temperatures close to T_C. Green curve: for the peak at 8.5 meV at $B = 0$ T; blue: 17 meV at $B = 0$ T. The red dashed lines are guides to the eye to highlight the change of slope at low magnetic fields.

junctions[18,23–25]. When the two graphene electrodes of the device are crystallographically misaligned, in-plane momentum conservation requires that the tunnelling electrons emit a phonon[21] or are scattered by impurities.

Magnon-assisted tunnelling

To identify the quasiparticles responsible for inelastic tunnelling events in the $CrBr_3$ devices, we measure G as a function of magnetic field parallel to the layers, $B_\parallel$ (perpendicular to the tunnelling current; see Fig. 1e). In this geometry, LL quantization of the electrons in graphene is absent. The measured resistance of the device contacts is practically independent of applied magnetic field; therefore, any change in position of a particular feature in conductance must be due to a change in the tunnel mechanism. In Fig. 1e,f, some of the peak positions are clearly dispersed in V_b by the applied magnetic field, whereas others are not. We attribute the non-dispersing peaks to the phonon-assisted tunnelling[18,23–25] and the dispersing peaks to the magnon-assisted tunnelling[16,32]. The dispersing peaks are shifted linearly with $B_\parallel$, with a slope of between $(5.1 \pm 0.2)\mu_B$ and $(5.7 \pm 0.2)\mu_B$, depending on the particular peak, here $\mu_B = 5.79 \times 10^{-5}$ eV T^{-1} is the electron Bohr magneton.

The calculated magnon density of states in $CrBr_3$, based on experimentally measured exchange parameters[33,34], is shown in Fig. 1g. The two van Hove singularities in the spectrum at 8.5 meV and 17 meV arise from the hexagonal symmetry of the $CrBr_3$ lattice. We relate these peaks to the two step-like increases in G observed in the experiment at low bias, when $V_b \approx 7.5$ mV and 17 mV (see Fig. 1b). Previously reported inelastic neutron scattering studies of magnons in $CrBr_3$ are in good agreement with our calculations and indicate that the magnon energy is limited to about 30 meV (refs [33,34]). This supports our assumption that non-dispersing steps in G at energies above 30 meV should be attributed to phonon-assisted tunnelling.

In a magnetic field, the Zeeman effect would shift the whole magnon spectrum by an energy $2\mu_B B$, along with the two van Hove singularities, if the magnon–magnon interaction is neglected (Fig. 1g and Supplementary Fig. 7). In the regime of low temperatures and high magnetic fields, self-consistent spin-wave calculations[35] predict a larger shift of the van Hove singularities of $\sim 2.4\mu_B B$. This enhanced shift of the magnon spectrum is due to magnon–magnon interactions, as explained in detail in the Supplementary Information. However, the observed magnetic field-induced shift of the position of the steps in conductance of $\sim 5\mu_B B$ is approximately twice larger than that expected by our

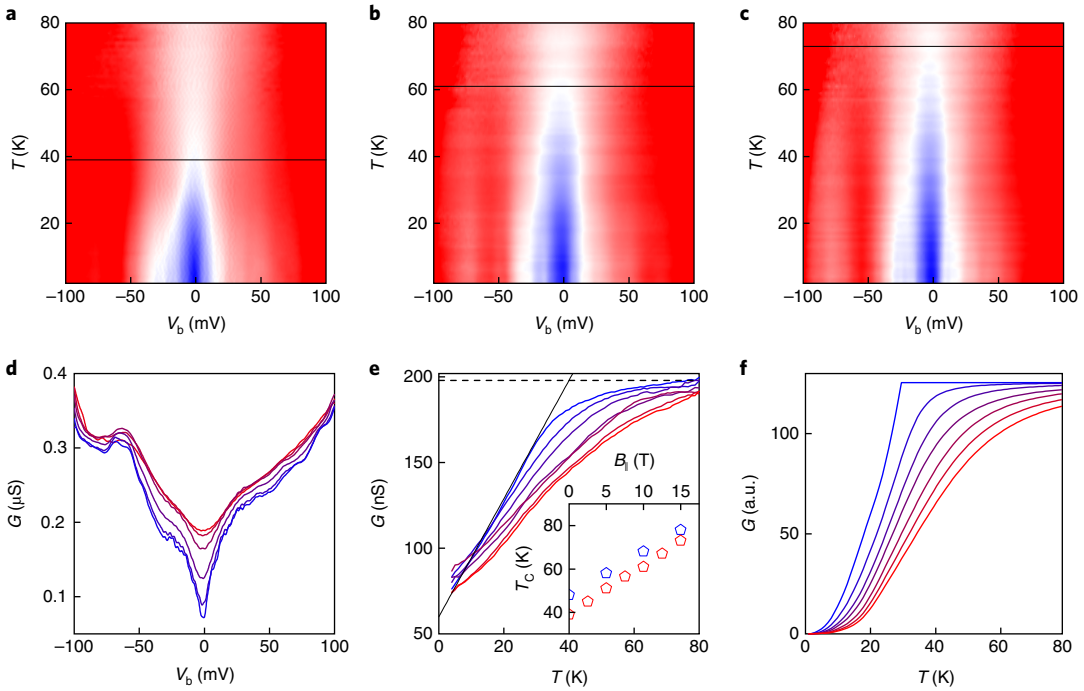

Fig. 2 | Effect of conductance on in-plane magnetic field. a–c, $G(V_b,T)$ when $V_g=0$ V and $B_\parallel=0$ T (**a**), $B_\parallel=10$ T (**b**), and $B_\parallel=15$ T (**c**) for a device with a 4-layer-thick $CrBr_3$ tunnel barrier (colour scale is blue to white to red, 0.06 μS to 0.17 μS to 0.3 μS for all contour plots in the figure). The black horizontal lines in **a–c** mark the extracted value of T_C. **d**, Zero-field tunnelling conductance plots for various temperatures at a fixed gate voltage of $V_g=0$ V (blue to red curves range from $T=2$ K to $T=50$ K with a step of 10 K). **e**, Dependence of the zero-bias tunnelling conductance G on T for different $B_\parallel$ (blue to red curves range between $B_\parallel=0$ T and $B_\parallel=15$ T with a 2.5 T increment). The straight lines are a guide for the eye and illustrate the method for extraction of the Currie temperature (plotted for $B_\parallel=0$ T). The dashed black horizontal line illustrates the saturating conductance at the high temperatures, and the straight solid line indicates the tangent to the particular curve. Inset: the extracted dependence of T_C on $B_\parallel$. The red and blue symbols are for devices with thicknesses of the $CrBr_3$ barrier of four and six layers respectively. **f**, Theoretical modelling of the zero-bias tunnelling conductance G dependence on T for different $B_\parallel$ (blue to red curves range between $B_\parallel=0$ T and $B_\parallel=15$ T with a 2.5 T increment). a.u., arbitrary units.

theory. Currently, we have no explanation for this discrepancy; understanding it will be the subject of future work. However, we note that at low B and temperatures close to T_C, our self-consistent spin-wave calculations predict a magnetic field-induced shift in the two van Hove singularities of $4.5\mu_B B$ and $7.1\mu_B B$, respectively (Fig. 1h and Supplementary Information), which is comparable to the shift measured in our experiments. Such a strong dependence of magnon spectra on magnetic field close to T_C can be understood as follows. Magnon frequencies depend strongly on temperature because both long- and short-range magnetic order are suppressed by spin fluctuations: both interlayer exchange interactions and the Zeeman gap in the magnon spectrum suppress the fluctuations, making the magnons stiffer. The transition between these regimes occurs when $2\mu_B B \approx J_L$ (J_L is the exchange integral between the layers). This is observed as a change in the slope of the calculated energy dependence of the van Hove singularities on the magnetic field at low B (Fig. 1h).

We now consider the dependence of the differential conductance on temperature, T. Figure 2a,d plots G as a function of V_b and T. We observe that the zero-bias differential conductance, $G_0=G(V_b=0)$, increases with increasing temperature. Its rate of change, dG_0/dT, is largest for temperatures between 15 K and 30 K and saturates above 40 K, close to the Curie temperature, $T_C\approx35$ K (refs [33,36]), for $CrBr_3$ (Fig. 2e). This behaviour is similar for devices with different $CrBr_3$ barrier thicknesses (see Supplementary Figs. 2 and 3) and we attribute it to an increase of elastic scattering of tunnelling electrons with temperature. We also measure the dependence of G on bias voltage and temperature for different $B_\parallel$ (Fig. 2a–c). In all cases, dG_0/dT decreases with increasing $B_\parallel$ (Fig. 2e).

At temperatures close to T_C, the magnon population is very high, so absorption of a magnon by a tunnelling electron is more probable. Moreover, at such temperatures, the short-range magnetic ordering between the layers and the long-range magnetic ordering within the $CrBr_3$ layer are destroyed as described by the self-consistent spin-wave theory of quasi-two-dimensional magnets[35,37]. The correlation length $\xi(T)$ within the layers is estimated to be

$$\frac{a}{\xi(T)}=\sqrt{\frac{2\,|\mu|}{3J\gamma}}$$

where a is the nearest-neighbour distance between magnetic atoms, and μ is the chemical potential of the self-consistent spin waves (see Supplementary Information). $J\gamma$ is the renormalized in-plane exchange interaction and the renormalization parameter γ is determined from self-consistent equations and defines the magnon hopping between adjacent sites (see Supplementary Information and ref. [35]) It can also be defined as $\gamma=SJ_{eff}/J$, where $S=3/2$ is the spin of Cr ion and J_{eff} is the effective exchange parameter in finite temperatures and magnetic fields when magnon occupation factors are finite.

These observations suggest two possible mechanisms for elastic tunnelling with momentum conservation at zero bias. First, consider a two-magnon process. In the case of a ferromagnetic barrier, emission of two magnons by a tunnelling electron is forbidden by spin conservation. However, a three-particle process, in which an electron emits one magnon and absorbs another, is possible. This type of process does not change the energy of the electron, changing

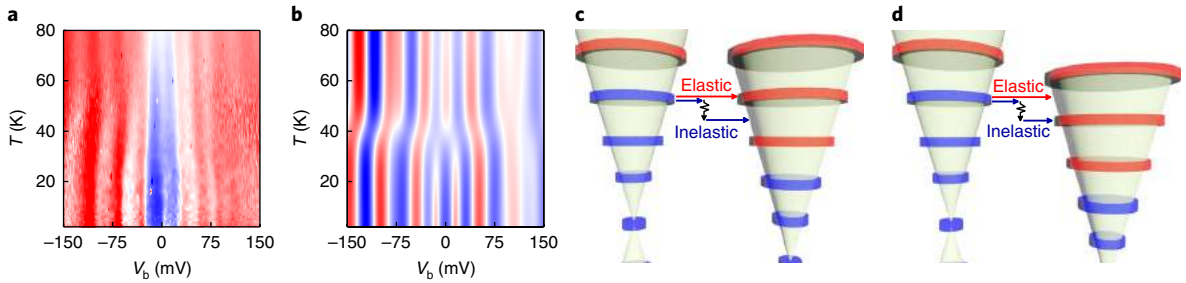

Fig. 3 | Inter-LL tunnelling. a,**b**, Measured (**a**) and calculated (**b**) $G(V_b,T)$ when $V_g=0$ V and $B_\perp=17.5$ T for a device with a 6-layer $CrBr_3$ barrier (colour scale is blue to white to red, 4 nS to 13 nS to 22 nS). **c**,**d**, Schematic diagrams of inelastic and elastic tunnelling events between the LL spectrum of the two graphene layers. Blue states are occupied; red states are empty. At low temperatures, the tunnelling is inelastic (blue arrows) with magnon emission (black arrow). Increasing temperature increases the contribution to the current of elastic two-magnon and spin-disorder scattering (red arrows). Application of a bias voltage differentiates between these two processes. In **c**, the bias is such that elastic processes allow resonant tunnelling between the third and fourth LLs. In **d**, the bias is higher, which brings the same third and fourth LLs into resonance, but is now mediated by inelastic tunnelling.

only its momentum, thus ensuring momentum conservation for electrons tunnelling between the Dirac cones of the two misoriented graphene layers. The ratio between the intensities of the magnon emission (Stokes) and absorption (anti-Stokes) processes is given by $\exp(E_m/k_BT)$, where E_m is the magnon energy and k_B is the Boltzmann constant. At low temperatures, absorption processes are suppressed. However, close to T_C and for our range of parameters, the typical magnon energies are of the order of $\sim k_BT_C$. In 3D magnets with $S\approx1$, typical magnon energies are of the order of k_BT_C since they are both proportional to zJ, where $z=3$ is the nearest-neighbour number. For 2D magnets, T_C is suppressed by a factor $\sim1/\ln(J/J_L)$ (see ref. [35] for explicit relations). The exchange integrals for $CrBr_3$ have previously been extracted experimentally[33,34] as $J=1.698$ mV and $J_L=0.082$ mV, giving $J/J_L\approx21$ and the suppression factor to be ~1/3, still of the order of unity. This makes the three-particle Stokes–anti-Stokes processes significant.

A second potential elastic scattering mechanism, which becomes dominant for $T\sim T_C$, is electron scattering on the imperfections in the spin texture within a $CrBr_3$ layer[38,39]. These imperfections break translational symmetry and are capable of scattering the wavevector of electrons by $1/\xi(T)$. According to our calculations, for temperatures close to T_C, the correlation length falls to values $\sim10a$, and to $\sim2a$ at $T\sim1.5T_C$ (see Supplementary Figs. 5 and 6). This length scale is much smaller than the de Broglie wavelength of the tunnelling electrons, which is of the order of tens or even hundreds of interatomic distances for the case of graphene under the measurement conditions reported here. Hence, close to and above T_C, tunnelling electrons encounter a highly disordered spin configuration; short-range order is lost entirely for $T>T_C$ (ref. [37]). Scattering of electrons on the short-range spin disorder is therefore analogous to the electron scattering on charged impurities, thereby ensuring momentum conservation for electrons tunnelling between misaligned graphene layers.

We model the elastic tunnelling rate at zero bias by calculating the scattering rate due to two-magnon processes at low temperatures ($T\lesssim T_C$) and scattering arising from spin imperfections in the ferromagnet at high temperatures ($T\gtrsim T_C$) (see Supplementary Fig. 8). For $T\lesssim T_C$, elastic scattering is dominated by two-magnon processes with a rate, W_{2mag}, proportional to the contribution of the longitudinal spectral density[40,41]. The probability of these two-magnon processes go to zero above $\sim T_C$ because the magnon description of spin excitation becomes invalid in this temperature regime. Instead, for $T\gtrsim T_C$, the elastic tunnelling rate, W_{spin}, is dominated by scattering on the disordered spin texture[38,39], which is dependent on the magnetization of the ferromagnet[42]. We combine the two scattering rates by smoothly varying the amplitudes of the two scattering rates to reflect the increase in the thermal spin disorder of the lattice, hence $W_{tot}=(1-f(T))W_{2mag}+f(T)W_{spin}$, where $f(T)=0.5[1+\tanh(\beta(T/T_C-1))]$. We obtain a good fit to the data when $\beta=4$ (see Fig. 2f).

The measured magnetic field dependence of the conductance also fits well to our model: as the external magnetic field increases, the magnon energy increases due to the Zeeman effect (Fig. 1g), thus reducing the magnon population and the rate W_{2mag} at a given T. At high temperatures, the external magnetic field contributes to spin alignment, thus reducing scattering by imperfections of the spin texture.

Inter-LL tunnelling

We also consider the effect of $B_\perp$ on G as a function of bias and temperature. Tunnelling between the LLs of the two graphene layers gives rise to peaks in G (see Fig. 3a). As T approaches T_C, we observe a clear shift in the position of the peaks in V_b. We interpret such behaviour as a transition from inter-LL tunnelling dominated by inelastic transitions, due to emission of a single magnon, to tunnelling dominated by elastic transitions, as described in the previous section. These tunnel processes are illustrated in the band diagrams (Fig. 3c,d), where inelastic and elastic tunnelling processes are depicted by blue and red arrows, respectively.

For instance, for the process depicted in Fig. 3c, in the case of inelastic tunnelling, an electron in the third LL of the bottom electrode cannot tunnel with the emission of a magnon since its reduced energy lies in the energy gap between the third and fourth LLs of the top graphene electrode (see blue arrow in Fig. 3c). In contrast, a peak in conductance is observed for electrons tunnelling with conservation of energy (red arrow in Fig. 3c), because the third LL in the bottom electrode is aligned in energy with the fourth LL in the top electrode. A slightly higher bias voltage brings the reduced energy of the inelastic tunnelling electron into alignment with an unoccupied state of the fourth LL in the top electrode, resulting in a peak in conductance (Fig. 3d). To demonstrate the effect of the temperature-dependent change in the relative contributions of these two processes, we show in Fig. 3b a colour map of conductance calculated using a model developed previously for phonon-assisted[23] inter-LL tunnelling[29] in a device with a non-magnetic hBN barrier. The model includes the two competing processes: inelastic tunnelling processes induced by a single magnon with an energy of 10 meV and a scattering amplitude, $\propto1-f(T)$, which decreases as the temperature increases through T_C; and elastic tunnelling processes whose amplitude, $\propto f(T)$, increases as the temperature increases. The model is in qualitative agreement with measured data (see Fig. 3a,b).

Spin-injection and proximity effects

This type of ferromagnetic tunnel barrier could be used to inject spin-polarized carriers into graphene or other 2D materials.

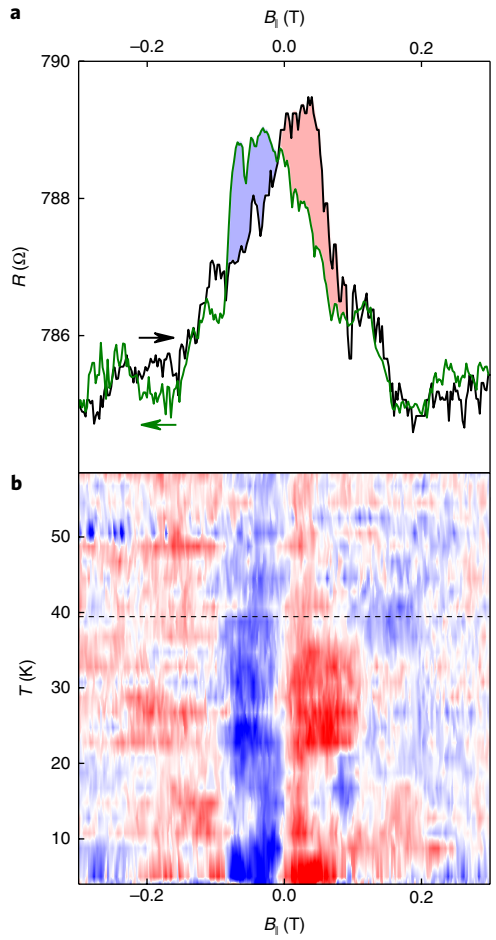

Fig. 4 | Magnetotransport in graphene proximitized with $CrBr_3$. a, Four-probe resistance plots of the bottom graphene electrode in a device with a 4-layer-thick $CrBr_3$ barrier as a function of in-plane magnetic field $B_{\parallel}$, at $T = 5$ K. The black and green curves correspond to sweeping $B_{\parallel}$ in the trace and retrace directions, respectively, indicated by the corresponding arrows. In the low field regime, $|B_{\parallel}| < 0.1$ T, the graphene exhibits a magnetoresistance of 0.5% and a hysteretic behaviour. The latter is indicated by the blue and red coloured areas between the trace and retrace curves. **b**, Colour map of the difference between trace and retrace curves as in **a**, now also as a function of temperature (colour scale is blue to white to red, −1 Ω to 0 Ω to 1 Ω). The black horizontal dashed line marks the extracted value of T_C, as in Fig. 2a. The hysteresis is visible in the colour map as the blue and red lobes in the range $|B_{\parallel}| < 0.1$ T. Both the magnitude of the hysteresis and the range of the hysteresis in $B_{\parallel}$ decrease for $T > T_C$, indicating their origin from the long-range magnetic order in the $CrBr_3$ barrier.

Pioneering work in traditional 3D materials has established the possibility to create a large (close to 100%) spin polarization in the tunnel current using ferromagnetic barriers, quantified via tunnelling spectroscopy using a superconductor electrode (also known as the Meservey–Tedrow technique)[27,28]. In van der Waals heterostructures based on graphene and other 2D crystals, the mechanisms of spin injection, and thus the possibility of obtaining large spin polarization, are linked strongly to the momentum conservation conditions. Thus, when the tunnelling states in the emitter and collector are displaced in the momentum space (as for twisted graphene lattices or for two materials with different lattice periodicity), conservation of in-plane momentum can be enabled by magnon emission, which selects only one spin polarization. Note that this is not the case for two-magnon processes, which cannot provide spin polarization. The use of ferromagnetic tunnel barriers could therefore enrich the type and functionality of van der Waals heterostructures.

A quite different set of physical phenomena, with the potential to enable van der Waals heterostructures for spintronics, are proximity effects between an electrode and ferromagnetic barrier. Recent works have provided evidence for the presence of both an induced exchange field and spin–orbit coupling in graphene, when in contact with a magnetically ordered 3D insulator, either by measuring the anomalous Hall effect[43] or by directly detecting pure spin current[44]. There is also evidence that proximity effects can lead to anisotropic magnetoresistance in graphene[45]. In our multi-terminal tunnelling structures, we have also measured in-plane transport within each of the two graphene electrodes. Thus, for the device shown in Fig. 1a, we measure the voltage between contacts 1 and 3, when a current flows from contacts 2 to 4 in the graphene layer below the ferromagnetic barrier (similar measurements were made for the top electrode with current flowing above the ferromagnetic barrier). In this type of measurement, the transport within a single graphene electrode is studied as a function of the in-plane magnetic field, for which there is neither Lorentz magnetoresistance nor LL quantization. Surprisingly, we still observe an appreciable magnetoresistance of ~0.5% (Fig. 4a). More importantly, the magnetoresistance exhibits hysteresis on the in-plane magnetic field, with this hysteresis diminishing rapidly for temperatures above T_C (Fig. 4b).

We attribute these observations to a proximity-induced anisotropic magnetoresistance (PAMR) in graphene[46], driven by the magnetization reversal processes of the tunnel barrier. The PAMR response is in qualitative and quantitative agreement with recent experimental[45] and theoretical[46] works, and indicates the presence of both spin–orbit coupling and an exchange field[47] in the graphene electrode. Finally, we note that the observation of PAMR provides an independent demonstration of ferromagnetic order in the tunnel barrier. This is further evidence that the vertical transport effects shown in Fig. 2 originate from the magnetic nature of the barrier.

Conclusions

We argue that tunnelling with magnon emission and proximity effects offers new prospects for exploiting 2D ferromagnetic barriers in graphene spintronics. In particular, the tunnel current can be spin-filtered. For the case of tunnelling through a ferromagnetic barrier, one-magnon processes will result in selective tunnelling of only one spin polarization. Indeed, at low temperatures, spin conservation, combined with the emission of a magnon, enables a tunnelling electron, initially in the spin-down state, to flip its spin into a final spin-up state. The one-magnon tunnelling process from an initial spin-up state is forbidden. Two-magnon processes would allow both spin polarizations to tunnel. However, they have a small probability at low temperatures since they require not only emission but also absorption of magnons; there are no magnons available for absorption near the ferromagnetic ground state.

Methods

Fabrication. The $CrBr_3$ crystals were purchased from a commercial supplier, HQ graphene.

$CrBr_3$ was first exfoliated onto a polypropylene carbonate-coated SiO_2/Si substrate in an argon-filled glove box maintaining the water and oxygen concentration less than 0.1 ppm. $CrBr_3$ flakes of different thicknesses (two to six layers) were identified by using the contrast variation under different colour filters and dark-field imaging. Heterostructures comprising SLG/$CrBr_3$/SLG encapsulated within thin boron nitride (BN) layers were assembled on a 290 nm SiO_2/Si substrate following a standard dry transfer procedure using a poly(methyl methacrylate) (PMMA) membrane. First, a single-layer graphene (SLG) sheet was picked up by a thin boron nitride layer (~8–10 nm BN) using the PMMA membrane. Subsequently, a suitable $CrBr_3$ layer was picked up by a SLG/BN/PMMA membrane in the glove box. Finally, this stack of $CrBr_3$/SLG/BN on the PMMA membrane was peeled onto the SLG/BN/290 nm SiO_2/Si substrate. The final stack consists of Si/290 nm SiO_2/~25 nm BN/SLG/$CrBr_3$/SLG/~10 nm BN.

For electrical characterization of the tunnelling devices, Cr/Au edge contacts were made on the top and bottom graphene layers using electron-beam lithography followed by boron nitride etching, metal deposition and a lift-off process. Boron nitride was etched in a reactive ion etching system using CHF_3 and oxygen chemistry. Contacts on the graphene sheets were made so as to have a four-probe measurement geometry. Note that during the heterostructure assembly, the top and bottom graphene layers were chosen to extend beyond the $CrBr_3$ layer so that the contact processing (especially the top BN etching and subsequent lift-off process) does not affect the $CrBr_3$.

Modelling. The magnon density of states was calculated in the nearest-neighbour approximation with the values of exchange integrals $J = 1.698$ meV and $J_L = 0.082$ meV taken from the experiment[33,34]. The temperature and magnetic field dependences of the magnon spectra were calculated within the self-consistent spin-wave theory[35]. The details are presented in the Supplementary Information.

Data availability. The data that support the plots within this paper and other findings of this study are available from the corresponding author upon reasonable request.

Received: 11 March 2018; Accepted: 15 May 2018;
Published online: 13 June 2018

References

1. Novoselov, K. S. et al. Electric field effect in atomically thin carbon films. *Science* **306**, 666–669 (2004).
2. Novoselov, K. S. et al. Two-dimensional atomic crystals. *Proc. Natl Acad. Sci. USA* **102**, 10451–10453 (2005).
3. Novoselov, K. S. Nobel Lecture: Graphene: Materials in the flatland. *Rev. Mod. Phys.* **83**, 837–849 (2011).
4. Butler, S. Z. et al. Progress, challenges, and opportunities in two-dimensional materials beyond graphene. *ACS Nano* **7**, 2898–2926 (2013).
5. Neto, A. H. C. & Novoselov, K. New directions in science and technology: two-dimensional crystals. *Rep. Progress. Phys.* **74**, 082501 (2011).
6. Geim, A. K. & Grigorieva, I. V. Van der Waals heterostructures. *Nature* **499**, 419–425 (2013).
7. Novoselov, K. S., Mishchenko, A., Carvalho, A. & Castro Neto, A. H. 2D materials and van der Waals heterostructures. *Science* **353**, aac9439 (2016).
8. Dean, C. et al. Graphene based heterostructures. *Solid State Commun.* **152**, 1275–1282 (2012).
9. Novoselov, K. S. & Neto, A. H. C. Two-dimensional crystals-based heterostructures: materials with tailored properties. *Phys. Scr.* **T146**, 014006 (2012).
10. Wang, H., Eyert, V. & Schwingenschlogl, U. Electronic structure and magnetic ordering of the semiconducting chromium trihalides $CrCl_3$, $CrBr_3$, and CrI_3. *J. Phys. Condens. Matter* **23**, 116003 (2011).
11. Sachs, B., Wehling, T. O., Novoselov, K. S., Lichtenstein, A. I. & Katsnelson, M. I. Ferromagnetic two-dimensional crystals: Single layers of K_2CuF_4. *Phys. Rev. B* **88**, 201402 (2013).
12. Zhang, W. B., Qu, Q., Zhua, P. & Lam, C. H. Robust intrinsic ferromagnetism and half semiconductivity in stable two-dimensional single-layer chromium trihalides. *J. Mater. Chem. C* **3**, 12457–12468 (2015).
13. Liu, J. Y., Sun, Q., Kawazoe, Y. & Jena, P. Exfoliating biocompatible ferromagnetic Cr-trihalide monolayers. *Phys. Chem. Chem. Phys.* **18**, 8777–8784 (2016).
14. McGuire, M. A., Dixit, H., Cooper, V. R. & Sales, B. C. Coupling of crystal structure and magnetism in the layered, ferromagnetic insulator CrI_3. *Chem. Mater.* **27**, 612–620 (2015).
15. Huang, B. et al. Layer-dependent ferromagnetism in a van der Waals crystal down to the monolayer limit. *Nature* **546**, 270–273 (2017).
16. Klein, D. R. et al. Probing magnetism in 2D van der Waals crystalline insulators via electron tunneling. *Science*, eaar3617 (2018).
17. Lee, G. H. et al. Electron tunneling through atomically flat and ultrathin hexagonal boron nitride. *Appl. Phys. Lett.* **99**, 243114 (2011).
18. Amet, F. et al. Tunneling spectroscopy of graphene-boron-nitride heterostructures. *Phys. Rev. B* **85**, 073405 (2012).
19. Britnell, L. et al. Electron tunneling through ultrathin boron nitride crystalline barriers. *Nano Lett.* **12**, 1707–1710 (2012).
20. Britnell, L. et al. Field-effect tunneling transistor based on vertical graphene heterostructures. *Science* **335**, 947–950 (2012).
21. Mishchenko, A. et al. Twist-controlled resonant tunnelling in graphene/boron nitride/graphene heterostructures. *Nat. Nanotech.* **9**, 808–813 (2014).
22. Wallbank, J. R. et al. Tuning the valley and chiral quantum state of Dirac electrons in van der Waals heterostructures. *Science* **353**, 575–579 (2016).
23. Vdovin, E. E. et al. Phonon-assisted resonant tunneling of electrons in graphene-boron nitride transistors. *Phys. Rev. Lett.* **116**, 186603 (2016).
24. Jung, S. et al. Vibrational properties of h-BN and h-BN-graphene heterostructures probed by inelastic electron tunneling spectroscopy. *Sci. Rep.* **5**, 16642 (2015).
25. Chandni, U., Watanabe, K., Taniguchi, T. & Eisenstein, J. P. Signatures of phonon and defect-assisted tunneling in planar metal-hexagonal boron nitride-graphene junctions. *Nano Lett.* **16**, 7982–7987 (2016).
26. Chandni, U., Watanabe, K., Taniguchi, T. & Eisenstein, J. P. Evidence for defect-mediated tunneling in hexagonal boron nitride-based junctions. *Nano Lett.* **15**, 7329–7333 (2015).
27. Moodera, J. S., Hao, X., Gibson, G. A. & Meservey, R. Electron-spin polarization in tunnel junctions in zero applied field with ferromagnetic EuS barriers. *Phys. Rev. Lett.* **61**, 637–640 (1988).
28. Santos, T. S. & Moodera, J. S. Observation of spin filtering with a ferromagnetic EuO tunnel barrier. *Phys. Rev. B* **69**, 241203 (2004).
29. Greenaway, M. T. et al. Resonant tunnelling between the chiral Landau states of twisted graphene lattices. *Nat. Phys.* **11**, 1057–1062 (2015).
30. Yu, G. L. et al. Interaction phenomena in graphene seen through quantum capacitance. *Proc. Natl Acad. Sci. USA* **110**, 3282–3286 (2013).
31. Yu, G. L. et al. Hierarchy of Hofstadter states and replica quantum Hall ferromagnetism in graphene superlattices. *Nat. Phys.* **10**, 525–529 (2014).
32. Tsui, D. C., Dietz, R. E. & Walker, L. R. Multiple magnon excitation in NiO by electron tunneling. *Phys. Rev. Lett.* **27**, 1729–1732 (1971).
33. Samuelsen, E. J., Silberglitt, R., Shirane, G. & Remeika, J. P. Spin waves in ferromagnetic $CrBr_3$ studied by inelastic neutron scattering. *Phys. Rev. B* **3**, 157–166 (1971).
34. Yelon, W. B. & Silberglitt, R. Renormalization of large-wave-vector magnons in ferromagnetic $CrBr_3$ studied by inelastic neutron scattering: spin-wave correlation effect. *Phys. Rev. B* **4**, 2280–2286 (1971).
35. Irkhin, V. Y., Katanin, A. A. & Katsnelson, M. I. Self-consistent spin-wave theory of layered Heisenberg magnets. *Phys. Rev. B* **60**, 1082–1099 (1999).
36. Ho, J. T. & Litster, J. D. Magnetic equation of state of $CrBr_3$ near critical point. *Phys. Rev. Lett.* **22**, 603–606 (1969).
37. Ghannadzadeh, S. et al. Simultaneous loss of interlayer coherence and long-range magnetism in quasi-two-dimensional $PdCrO_2$. *Nat. Commun.* **8**, 15001 (2017).
38. De Gennes, P. G. & Friedel, J. Anomalies de resistivite dans certains metaus magnettiques. *J. Phys. Chem. Solids* **4**, 71–77 (1958).
39. Haas, C. Spin-disorder scattering and magnetoresistance of magnetic semiconductors. *Phys. Rev.* **168**, 531–538 (1968).
40. Irkhin, V. Y. & Katsnelson, M. I. Current carriers in a quantum 2-dimensional antiferromagnet. *J. Phys. Condens. Matter* **3**, 6439–6453 (1991).
41. Korenblit, I. Y. & Lazarenko, Y. P. Electron–magnon interaction in ferromagnetic semiconductors. *Phys. Status Solidi B* **71**, K107–K110 (1975).
42. Gantmakher, V. F. & Levinson, Y. B. *Carrier Scattering in Metals and Semiconductors* (North Holland, Amsterdam,1987).
43. Wang, Z. Y., Tang, C., Sachs, R., Barlas, Y. & Shi, J. Proximity-induced ferromagnetism in graphene revealed by the anomalous Hall effect. *Phys. Rev. Lett.* **114**, 016603 (2015).
44. Leutenantsmeyer, J. C., Kaverzin, A. A., Wojtaszek, M. & van Wees, B. J. Proximity induced room temperature ferromagnetism in graphene probed with spin currents. *2D Mater.* **4**, 014001 (2017).
45. Mendes, J. B. S. et al. Spin-current to charge-current conversion and magnetoresistance in a hybrid structure of graphene and yttrium iron garnet. *Phys. Rev. Lett.* **115**, 226601 (2015).
46. Lee, J. & Fabian, J. Magnetotransport signatures of the proximity exchange and spin–orbit couplings in graphene. *Phys. Rev. B* **94**, 195401 (2016).
47. Asshoff, P. U. et al. Magnetoresistance of vertical Co-graphene-NiFe junctions controlled by charge transfer and proximity-induced spin splitting in graphene. *2D Mater.* **4**, 031004 (2017).

Acknowledgements

This work was supported by the EU Graphene Flagship Program, the European Research Council Synergy Grant Hetero2D, the Royal Society, the Engineering and Physical Research Council (UK) and the US Army Research Office (W911NF-16-1-0279). S.V.M. was supported by RFBR (17-02-01129a) and RAS Presidium Program N4 (task 007-00220-18-00).

Author contributions

A.M., F.W. and Y.L. manufactured the devices; D.G., Z.W., V.H.G.-M., J.Y. and S.V.M. performed the measurements; M.T.G., O.K., A.I.L. and M.I.K. performed theoretical simulations, I.J.V.-M., A.M., L.E., A.K.G. and K.S.N. initiated and supervised the work, and wrote the manuscript.

Competing interests

The authors declare no competing interests.

Additional information

Supplementary information is available for this paper at https://doi.org/10.1038/s41928-018-0087-z.

Reprints and permissions information is available at www.nature.com/reprints.

Correspondence and requests for materials should be addressed to K.S.N.

Publisher's note: Springer Nature remains neutral with regard to jurisdictional claims in published maps and institutional affiliations.

S1. Device fabrication

S2. Temperature dependence of differential dI/dV_b conductance on magnetic field for devices with different thickness of $CrBr_3$

S3. Quantum capacitance of Gr/$CrBr_3$/Gr devices

S4. Calculation of magnon density of states

S5. Scattering rates

S1. Device fabrication

Several devices with a different number of $CrBr_3$ layers (2 to 6) were fabricated. Fig. S1 depicts the procedure for fabricating a device with 4 layers of $CrBr_3$.

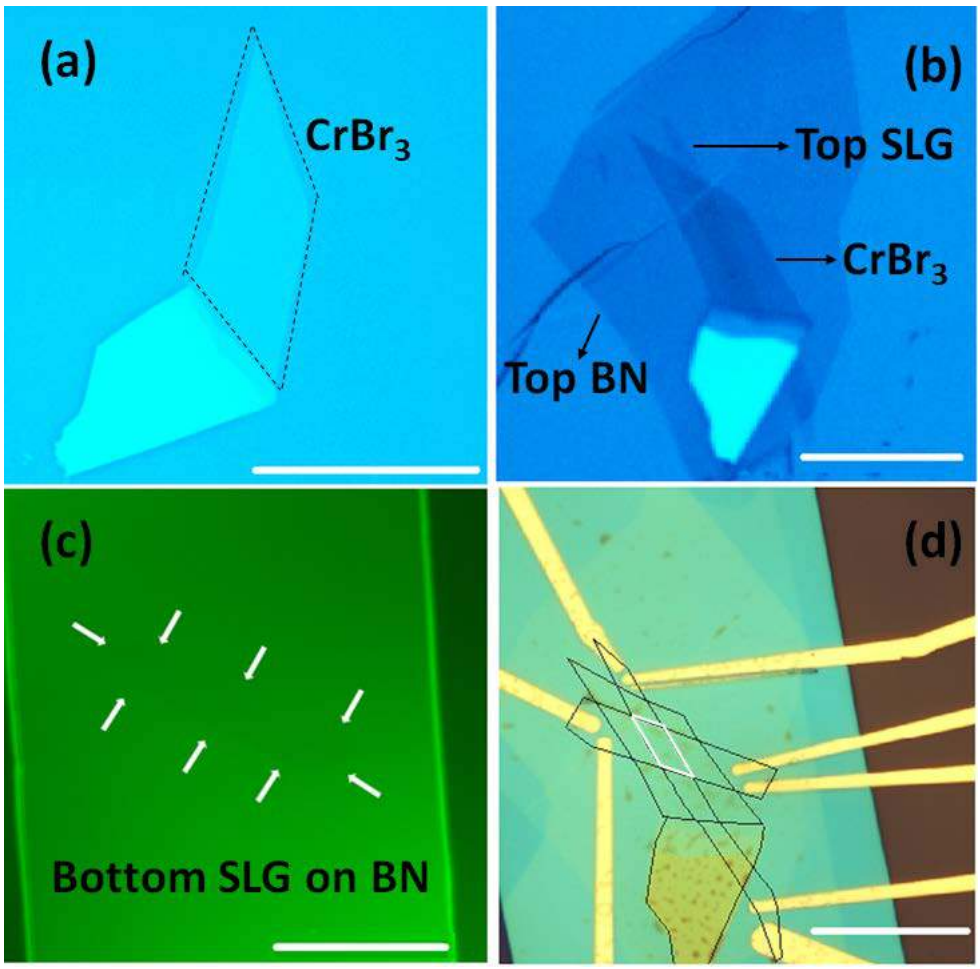

Supplementary Figure 1| Optical images of Gr/$CrBr_3$/Gr tunnel device encapsulated with hBN during different fabrication steps. a, 4 layers $CrBr_3$ flake (marked by black dashed line). **b,** $CrBr_3$/SLG/top BN picked up on PMMA membrane (SLG – single layer graphene). **c,** SLG (marked by the white arrows) transferred on bottom hBN. After this, the stack shown in b, was transferred on the SLG/BN/SiO_2/Si shown in c,. **d,** hBN encapsulated SLG/$CrBr_3$/SLG stack with deposited Cr/Au contacts. Black lines highlight different layers and white parallelogram marks the actual tunnelling area. Scale bars in all images are 20 μm.

S2. Temperature dependence of differential dI/dV_b conductance on magnetic field for devices with different thickness of $CrBr_3$

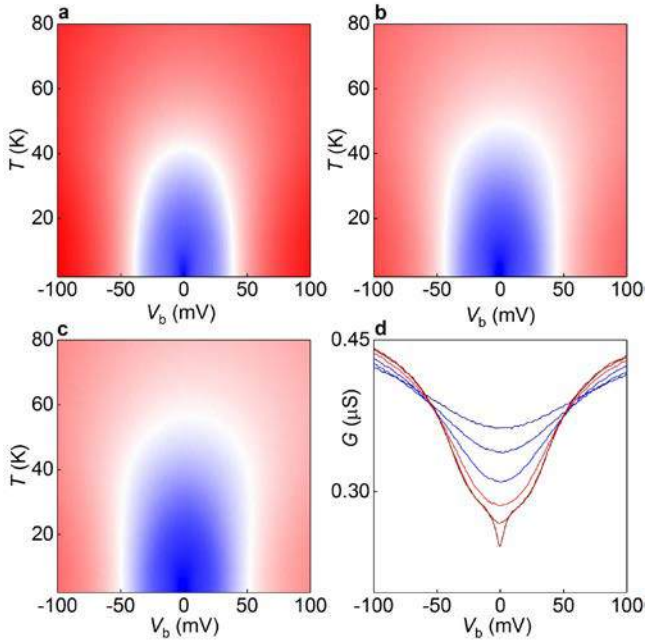

Supplementary Figure 2|a, Differential tunnel conductance as a function of V_b and T at $B_{||}$=0T and V_g=0V for a device with 2 layer thick $CrBr_3$ tunnel barrier (colour scale blue to white to red, 244μS to 343μS to 443μS for all contour plots in the figure). **b**, Similar to a, except $B_{||}$=10T. **c**, Similar to a, except $B_{||}$=17.5T. **d**, Zero-field tunnel conductance plots for various temperatures at a fixed gate voltage of V_g=*0V* (blue to purple curves range from *T*=2*K* to *T*=50K with the step 10K).

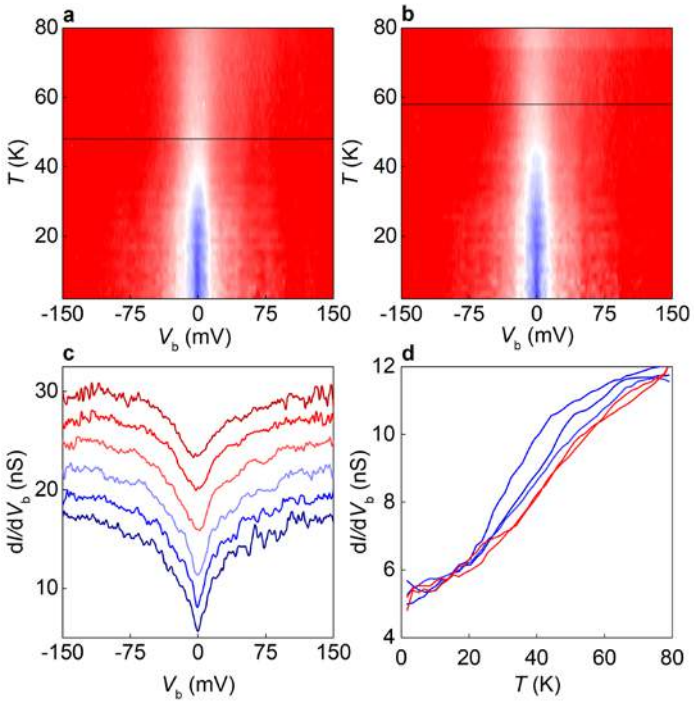

Supplementary Figure 3|a, Differential tunnel conductance as a function of V_b and T at $B_{||}$=0T and V_g=0V for a device with a 6-layer thick $CrBr_3$ tunnel barrier (colour scale blue to white to red, 3nS to 9.25nS to 16.5nS for all contour plots in the figure). Black horizontal lines in a,b mark the position of

the extracted value of T_c. **b**, Similar to a, except $B_{||}$=10T. **c**, Zero-field tunnel conductance plots for various temperatures at a fixed gate voltage, V_g=0V (blue to purple curves range from 2K to 50K in steps of 10K, curves are shifted vertically for clarity). **d,** Dependence of the zero bias tunneling conductance dI/dV_b on T for different $B_{||}$ (red to blue curves are $B_{||}$=0T, 5T, 10T, 15T, 17.5T).

S3. Quantum capacitance of Gr/$CrBr_3$/Gr devices

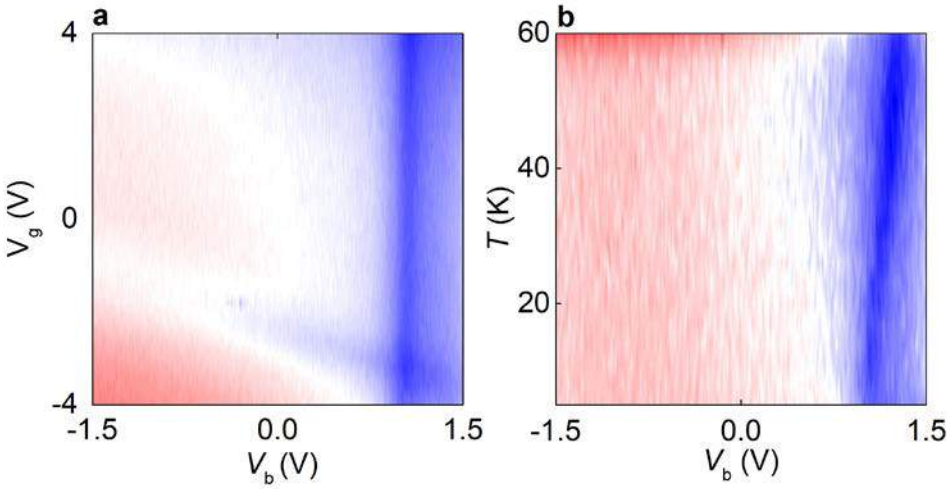

Supplementary Figure 4| Quantum capacitance measurements of the top gated Gr/$CrBr_3$/Gr device (fabricated on quartz substrate). $CrBr_3$ thickness 15nm, cross-section area 100μm^2. a, Capacitance as a function of V_b and V_g at T=2K and zero magnetic field (colour scale blue to white to red, 0.23pF to 0.24pF to 0.25pF). Two blue regions correspond to the suppressed density of states near the Dirac points of the top and bottom graphene layers. The edge of the blue region for the bottom layer is vertical, consistent with strong screening of the gate-induced electric field by the thick $CrBr_3$ barrier. **b,** the differential capacitance as a function of V_b and T at a fixed V_g=*0V* voltage.

S4. Magnon density of states

To calculate renormalized magnon spectra at finite temperatures we use self-consistent spin-wave theory in the form suggested in Ref.[S1]. We modify it to the case of a hexagonal lattice. For a single layer, there are two magnetic atoms per elementary cell with the corresponding magnon annihilation operators b_1 and b_2. The magnon spectrum is diagonalized by the same unitary transformation as for the electronic spectrum of graphene [S2],

$$b_{\vec{k}1} = \frac{1}{\sqrt{2}}\left(\alpha_{\vec{k}1} + \alpha_{\vec{k}2}\right),$$
$$b_{\vec{k}2} = \frac{S\left(\vec{k}\right)}{\sqrt{2}\,f\left(\vec{k}\right)}\left(\alpha_{\vec{k}1} - \alpha_{\vec{k}2}\right)$$

where $\vec{k}$ is the magnon wave vector, $S\left(\vec{k}\right) = \sum_{\vec{\delta}} e^{i\vec{k}\vec{\delta}}$, $\vec{\delta}$ are the nearest neighbour vectors and $f\left(\vec{k}\right) = \left|S\left(\vec{k}\right)\right|$. The self-consistent magnon spectrum at finite temperatures is determined by the two

parameters, γ, γ_L characterizing the renormalization of in-plane and out-of-plane exchange integrals (J and J_L), respectively. The two magnon branches are:

$$E_{\vec{k}1,2} = 2J\gamma\left(3 \mp f\left(\vec{k}\right)\right) + 2J_L\gamma_L\left(1-\cos k_z c\right) - \mu,$$

where c is the interlayer distance and μ is the magnon chemical potential which is nonzero above the Curie temperature. The self-consistent equations for the parameters γ, γ_L and the average spin per site $\overline{S}$ are

$$\gamma = \overline{S} + \frac{1}{6}\sum_{\vec{k}} f\left(\vec{k}\right)\left[N_B\left(E_{\vec{k}1}\right) - N_B\left(E_{\vec{k}2}\right)\right]$$

$$\gamma_L = \overline{S} + \frac{1}{2}\sum_{\vec{k}}\left[N_B\left(E_{\vec{k}1}\right) + N_B\left(E_{\vec{k}2}\right)\right]\cos k_z c$$

$$\overline{S} = S + (2S+1)N_B\left(E_f\right) - \frac{1}{2}\sum_{\vec{k}}\left[N_B\left(E_{\vec{k}1}\right) + N_B\left(E_{\vec{k}2}\right)\right]$$

where $E_f = (2S+1)(6J\gamma + 2J_L\gamma_L - \mu)$ and $N_B(E) = \dfrac{1}{\exp(E/k_BT)-1}$ is the Bose Einstein distribution function.

The computational results are shown in Fig.S5. The calculations show that the effective magnetic coupling between the layers characterized by the parameter γ_L disappears near the Curie temperature whereas the short-range order in-plane characterized by the parameter γ survives to higher temperatures, as expected for quasi-two-dimensional magnets [S3].

The in-plane correlation length $\xi(T)$ can be estimated from the effective spin-wave spectrum above the Curie temperature,

$$E\left(\vec{k}\right) = D\left(k^2 + \frac{1}{\xi^2}\right),$$

where D is the spin-wave stiffness constant. For the particular case of the honeycomb lattice in the nearest-neighbour approximation

$$a/\xi(T) = \sqrt{\frac{2|\mu|}{3J\gamma}},$$

where a is the distance between the neighbouring magnetic ions. The computational results are shown in Fig. S6.

The self-consistent spin-wave theory does not give a very accurate estimate of T_c, but is rather an upper estimate. Fluctuation corrections will lower the value of T_c, by a factor ~1.5 [S1]. Therefore, in

our comparison of the theory with experiment, we have shifted the temperature dependence of calculated variables by the calculated value of T_c but keeping the same ratio of J/J_L.

To consider how the magnetic field B affects the magnon spectrum, one needs to replace $-\mu$ by the Zeeman gap $2\mu_B B$, where μ_B is the Bohr magneton, in all the above equations. Self-consistent solution of the equations for our parameters gives us the shift of magnon energy peaks with the slope being between $4.5\cdot\mu_B$ V/T and $7.1\cdot\mu_B$ V/T depends on two Van Hove singularities at temperature close to T_c (Figure S7).

Within the self-consistent spin-wave theory, the intensity of the two-magnon processes (one magnon is emitted and one magnon is adsorbed) with the total energy change close to zero and the total wave vector change equal to $\vec{q}$ is proportional to the corresponding contribution to the longitudinal spectral density and reads [S4]

$$K_{\vec{q}}(T,H)=\sum_{\vec{k}} N_{\vec{k}}(1+N_{\vec{k}+\vec{q}})\delta\left(E_{\vec{k}}-E_{\vec{k}+\vec{q}}\right)$$

In all the calculations we use the experimental values of the exchange parameters. We have performed also the first-principle calculations of these quantities. Assuming the nearest-neighbour approximation, we estimated the parameters J and J_L from the total energy differences of various magnetic configurations (ferromagnetic, ferromagnetic in each layers with antiferromagnetic orientation between the layers, and antiferromagnetic within the layer) using the accurate full potential linearized augmented plane-wave (FLAPW) Wien2k code [S5] within the generalized gradient approximation (GGA) and experimental crystal structure. The results for (12x12x2) k-point mesh are J=0.94mV and J_L=0.076mV, respectively. The theoretical exchange J_L parameter agrees well with the experimental values [S6], while the intralayer exchange J is about 45% smaller. If one uses the theoretical GGA lattice parameters [S7] instead of the experimental ones, the corresponding exchange J is about 44% larger than the experimental value [S6]. So strong dependence of the calculated exchange parameters on interatomic distances makes the use of the experimental values the most reliable choice.

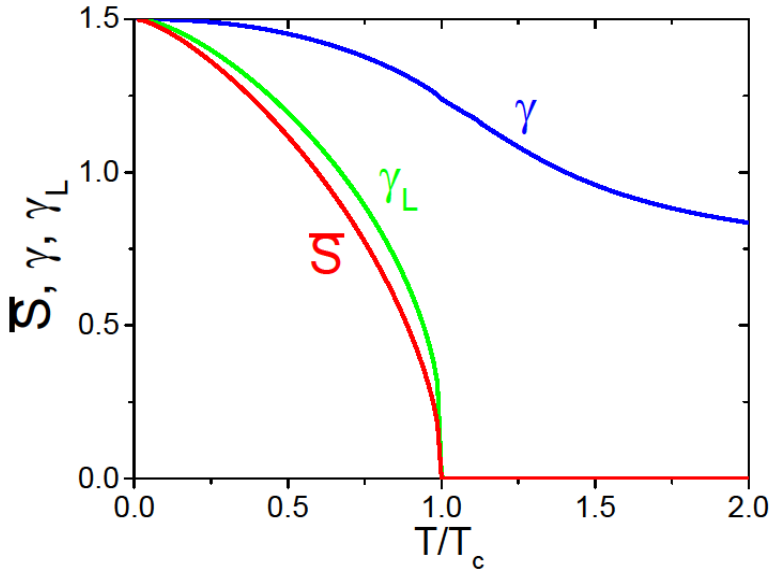

Supplementary Figure 5|Temperature dependences of $\bar{S}, \gamma, \gamma_L$ at zero magnetic field.

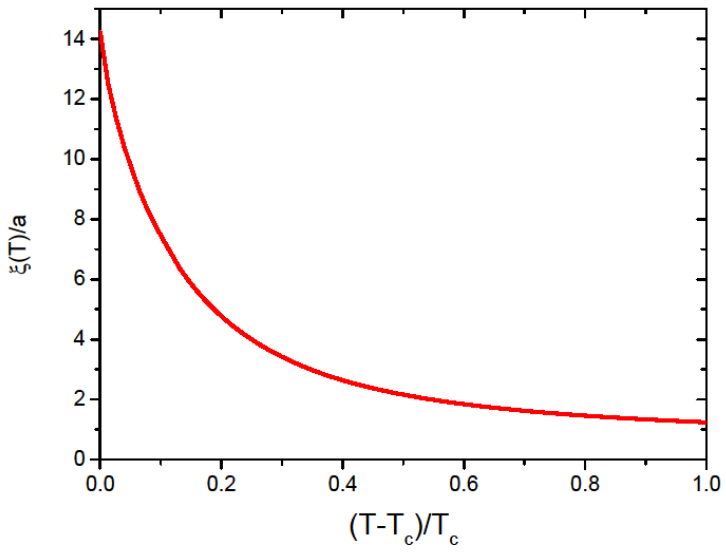

Supplementary Figure 6|Temperature dependence of $\xi(T)$/ a.

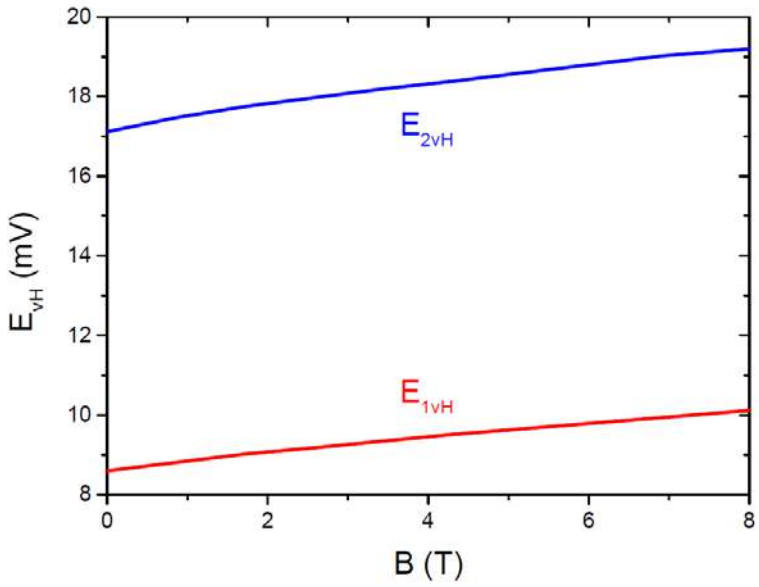

Supplementary Figure 7|Magnetic field dependence of the positions of van Hove singularities in magnon spectrum.

S5 Scattering rates

The scattering rate for the two magnon process (one magnon is emitted and one magnon is adsorbed) is proportional to the corresponding contribution to the longitudinal spectral density which is given by the function K_q. To make this relationship explicit we define $W_{2mag} \propto K_q$. The temperature dependence of W_{2mag} is shown in Fig S8.

The scattering rate from the disordered spin texture at high temperatures $T \gtrsim T_c$ is proportional to the spin correlator for the longitudinal component of the atomic spin, $\langle(\delta S^z)^2\rangle$, see ref. 42 of the manuscript for more detail, so that

$$W_{spin} \propto \langle(\delta S^z)^2\rangle$$

We find that a good fit to the data can be obtained if we take a mean field approach where

$$\langle(\delta S^z)^2\rangle = S(S+1) + \langle S^z\rangle \coth \beta/2 - \langle S^z\rangle^2$$

and the expectation value of the spin $\langle S^z\rangle$ is obtained using the standard self-consistent solution of the Brillouin function, using the Curie Weiss law so that:

$$\beta = \frac{gS\mu_B}{k_B T}(B + \lambda M)$$

In which μ_B is the Bohr magneton, $\lambda(T_c)$ is the Weiss molecular field constant and $M{=}Ng\mu_B\langle S^z\rangle$ is the magnetisation.

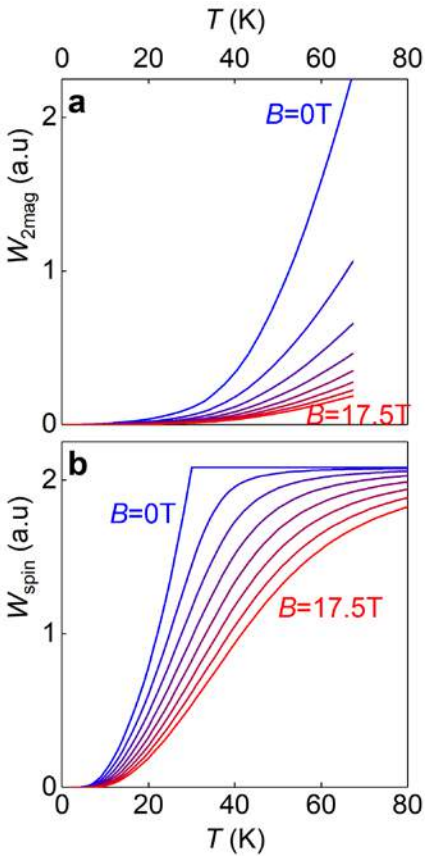

Supplementary Figure 8| Scattering rates. Curves blue to red are for magnetic fields $B_{\|}$=0T to $B_{\|}$=17.5T in 2.5T increment.

Supplementary References

[S1] Irkhin, V. Y., Katanin, A. A. & Katsnelson, M. I. Self-consistent spin-wave theory of layered Heisenberg magnets. *Phys. Rev. B* **60**, 1082-1099, doi:10.1103/PhysRevB.60.1082 (1999).

[S2] Katsnelson, M. I. Graphene: Carbon in Two Dimensions (Cambridge Univ, Press, Cambridge, 2012)

[S3] Ghannadzadeh, S. *et al.* Simultaneous loss of interlayer coherence and long-range magnetism in quasi-two-dimensional PdCrO2. *Nat. Commun.* **8**, 15001, doi:10.1038/ncomms15001 (2017).

[S4] Irkhin, V. Yu. & Katsnelson, M. I. Current carriers in a quantum two-dimensional magnets, *J. Phys.: Cond. Mat.* **3**, 6439-6453, doi:10.1088/0953-8984/3/33/021 (1991).

[S5] Blaha, P., Schwarz, K., Madsen, G., Kvasnicka, D. & Luitz, J. WIEN2k, An augmented Plane Wave+Local Orbitals Program for Calculating Crystal Properties, Techn. Universitat Wien, Austria, ISBN 3-9501031-1-2, 2001.

[S6] Samuelsen, E. J., Silberglitt, R., Shirane, G. & Remeika, J. P. Spin waves in ferromagnetic CrBr3 studied by inelastic neutron scattering. *Physical Review B-Solid State* **3**, 157-166, doi:10.1103/PhysRevB.3.157 (1971).

[S7] Zhang, W. B., Qu, Q., Zhua, P. & Lam, C. H. Robust intrinsic ferromagnetism and half semiconductivity in stable two-dimensional single-layer chromium trihalides. *J. Mater. Chem. C* **3**, 12457-12468, doi:10.1039/c5tc02840j (2015).

Seven

Conclusion

The aim of the present thesis was to study the electronic and magnetic properties of strongly correlated systems within the approach based on a combination of density functional theory and dynamical mean - field theory in charge self - consistent manner and to develop the scheme to avoid a problem of nonspherical double - counting.

The main conclusions and scientific results of the thesis can be formulated as follows:

1) We applied a DFT + DMFT approach in a charge self - consistent manner to show that although both compounds do not fall in the standard class of strongly correlated systems, more subtle many - body effects are required for an accurate description of the Fe_3Al and Fe_2VAl. This study provides an explanation as to how such effects provide an improved value for the formation energy with a clear separation to the $L1_2$ structure to get enhanced energetics and phase stability. The charge self - consistent version of the DFT + DMFT framework is essential to clarify such physics. The issue of chemical disorder is definitely applicable concerning the phase stabilities close to the Fe_3Al composition of the Fe - Al phase diagram. The detailed thermodynamic understanding of Fe - Al still needs to be further faced.

The Fe_2VAl compound is gotten from the well - known Fe_3Al metal however shows an intricate gap opening reminiscent of (pseudo)gap physics found in correlated oxides. The DFT + DMFT gap size and its sensitivity to temperature are compared with the experimental data and are in excellent agreement. Since also Hund's

physics may assume a part on the vanadium site, this example indicates the whole difficulty of mechanisms from strongly correlated properties for traditional material physics. Our results concerning the thermoelectric properties of Fe_2VAl could be interesting in a future work.

2) We performed a first - principles many - body examination of the impact of oxygen vacancies in rutile TiO_2, both in the regime of lower - and the higher - concentration. In the previous case, the results of DFT + DMFT give the three key components known from experiment for $TiO_{2-\delta}$, particularly semiconducting behavior and shallow levels as well as deep levels. Our deep - level (or in - gap) position is in excellent agreement with results of different experimental studies.

3) One important issue arising in the DFT + DMFT approach is that when we add the Coulomb interaction to the one - electron DFT Hamiltonian, we are counting effects of the Coulomb interaction twice, because some parts of the interaction are already included in the DFT Hamiltonian through the Hartree and exchange - correlation terms. In this scheme, double - counting is corrected approximately. This double - counting correction stems from a spherically symmetric treatment. The DFT part of the Hartree and exchange correlation energies are preserved along with the nonspherical contributions into the DFT + DMFT energy functional. We managed to exclude this nonspherical double - counting in DFT + DMFT. In our work we used the advanced DFT + DMFT approach to calculate the total - energy calculation and structural optimization of the pnictide superconductor LaFeAsO. We compared our results with the "exact" double - counting scheme of [Hau15]. In both cases a similar shift in the distance of Fe - As is observed, which brings the DFT + DMFT results closer to experiments. In future investigations it will be interesting to check more fine effects, for example, the crystal field parameters of transition - metal and rare - earth ions in different crystals. The standard double - counting scheme in the atomic limit could be appropriate for strongly correlated d - and f - systems with anisotropic Coulomb interactions near the insulating states.

4) Finally, it was demonstrated that electrons tunnel between the graphene layers via the emission (and, at high temperature, absorption) of magnons in the CrBr3 barrier. Motivated by this new type of tunneling mechanism, we investigated the temperature and magnetic field dependence of the magnon spectra within the self - consistent spin - wave - theory. We performed the first - principle calculations of the density of states, optical properties and exchange parameters for better understanding of physical properties of this material.

A

List of publications and author contributions

Publications discussed in this thesis

1. Quantum many - body intermetallics: Phase stability of Fe_3Al and small - gap formation in Fe_2VAl
   O. Kristanovski, R. Richter, I. Krivenko, A. I. Lichtenstein, and F. Lechermann
   Physical Review B **95** 045114 (2017)
   Reprinted on page 46

   This author participated in the development of the algorithms, implemented it, performed the calculations and contributed to analysis and the preparation of the manuscript

2. Oxygen - vacancy driven electron localization and itinerancy in rutile - based Ti_2O
   F. Lechermann, W. Heckel,O. Kristanovski, and S. Mueller
   Physical Review B **95** 195159 (2017)
   Reprinted on page 58

   This author participated in the performing of the calculations and in the analysis of the manuscript

3. Role of non - spherical double counting in DFT + DMFT: total energy and structural optimization of pnictide superconductors
   O. Kristanovski, A. B. Shick, F. Lechermann, and A. I. Lichtenstein
   Physical Review B**97**, 20116(R) (2018)
   Reprinted on page page 74

   This author participated in developing the algorithm, implemented it, performed the calculations, participated in the analysis and in the preparation of the manuscript

4. Magnon - assisted tunneling in van der Waals heterostructures on $CrBr_3$
   D. Ghazaryan, M. T. Greenaway, Z. Wang, V. H. Guarochico - Moreira, I. J. Vera - Marun, J. Yin, Y. Liao, S. V. Morozov, O. Kristanovski, A. I. Lichtenstein, M. I. Katsnelson, F. Withers, A. Mishchenko, L. Eaves, A. K. Geim, K. S. Novoselov, A. Misra

   Nature electronics **1**,344 - 349, June (2018)
   Reprinted on page 84

   This author participated in developing the framework and the algorithms, implemented it, performed the calculations and participated in the analysis of the manuscript

Unrelated work

1. Multiorbital Kondo effect of Co atoms at long Cu chains
   N. Noei, A. Weismann, R. Mozara, O. Kristanovski, A. I. Lichtenstein, and R. Berndt
   arXiv: [cond-mat.mtrl-sci] (2018)
   This manuscript is currently under consideration for publication

This author contributed to the implementation and calculations and participated in the analysis

Bibliography

[AAL97] V. I. Anisimov, F. Aryasetiawan, and A. I. Lichtenstein. First-principles calculations of the electronic structure and spectra of strongly correlated systems: the lda + u method. *Journal of Physics: Condensed Matter*, 9(4):767, 1997.

[AKK+05] V. I. Anisimov, D. E. Kondakov, A. V. Kozhevnikov, I. A. Nekrasov, Z. V. Pchelkina, J. W. Allen, S.-K. Mo, H.-D. Kim, P. Metcalf, S. Suga, A. Sekiyama, G. Keller, I. Leonov, X. Ren, and D. Vollhardt. Full orbital calculation scheme for materials with strongly correlated electrons. *Phys. Rev. B*, 71:125119, Mar 2005.

[AKN+06] V. I. Anisimov, M. A. Korotin, I. A. Nekrasov, A. S. Mylnikova, A. V. Lukoyanov, J. L. Wang, and Z. Zeng. The role of transition metal impurities and oxygen vacancies in the formation of ferromagnetism in co-doped tio2. *Journal of Physics: Condensed Matter*, 18(5):1695, 2006.

[ALG+08] B. Amadon, F. Lechermann, A. Georges, F. Jollet, T. O. Wehling, and A. I. Lichtenstein. Plane-wave based electronic structure calculations for correlated materials using dynamical mean-field the-

ory and projected local orbitals. *Phys. Rev. B*, 77:205112, May 2008.

[And61] P. W. Anderson. Localized magnetic states in metals. *Phys. Rev.*, 124:41–53, Oct 1961.

[APK+97a] V. I. Anisimov, A. I. Poteryaev, M. A. Korotin, A. O. Anokhin, and G. Kotliar. First-principles calculations of the electronic structure and spectra of strongly correlated systems: dynamical mean-field theory. *Journal of Physics: Condensed Matter*, 9(35):7359, 1997.

[APK+97b] V. I. Anisimov, A. I. Poteryaev, M. A. Korotin, A. O. Anokhin, and G Kotliar. First-principles calculations of the electronic structure and spectra of strongly correlated systems: dynamical mean-field theory. *Journal of Physics: Condensed Matter*, 9(35):7359, 1997.

[APS+16] M. Aichhorn, L. Pourovskii, P. Seth, V. Vildosola, M. Zingl, O. E. Peil, X. Deng, J. Mravlje, G. J. Kraberger, C. Martins, M. Ferrero, and O. Parcollet. Triqs/dfttools: A triqs application for ab initio calculations of correlated materials. *Computer Physics Communications*, 204:200 – 208, 2016.

[APV+09] Markus Aichhorn, Leonid Pourovskii, Veronica Vildosola, Michel Ferrero, Olivier Parcollet, Takashi Miyake, Antoine Georges, and Silke Biermann. Dynamical mean-field theory within an augmented plane-wave framework: Assessing electronic correlations in the iron pnictide lafeaso. *Phys. Rev. B*, 80:085101, Aug 2009.

[Ard94] H. K. Ardakani. Electrical and optical properties of in situ "hydrogen-reduced" titanium dioxide thin films deposited by pulsed excimer laser ablation. *Thin Solid Films*, 248(2):234 – 239, 1994.

[AZA91] Vladimir I. Anisimov, Jan Zaanen, and Ole K. Andersen. Band theory and mott insulators: Hubbard u instead of stoner i. *Phys. Rev. B*, 44:943–954, Jul 1991.

[BCV01] R. Bulla, T. A. Costi, and D. Vollhardt. Finite-temperature numerical renormalization group study of the mott transition. *Phys. Rev. B*, 64:045103, Jun 2001.

[BG11] Daniel I. Bilc and Philippe Ghosez. Electronic and thermoelectric properties of fe_2val: The role of defects and disorder. *Phys. Rev. B*, 83:205204, May 2011.

[BHM+87] Jeremy K. Burdett, Timothy Hughbanks, Gordon J. Miller, James W. Richardson, and Joseph V. Smith. Structural-electronic relationships in inorganic solids: powder neutron diffraction studies of the rutile and anatase polymorphs of titanium dioxide at 15 and 295 k. *Journal of the American Chemical Society*, 109(12):3639–3646, 1987.

[BM86] J. G. Bednorz and K. A. Müller. Possible high tc superconductivity in the ba-la-cu-o sytem. *Journal of physics B Condensed Matter*, 64(2):189, Jun 1986.

[BSM+01] P. Blaha, K. Schwarz, G. K. H. Madsen, D. Kvasnicka, and J. Luitz. *WIEN2K, An Augmented*

Plane Wave + Local Orbitals Program for Calculating Crystal Properties. Karlheinz Schwarz, Techn. Universität Wien, Austria, 2001.

[CA80] D. M. Ceperley and B. J. Alder. Ground state of the electron gas by a stochastic method. *Phys. Rev. Lett.*, 45:566–569, Aug 1980.

[Can03] G. Cangiani. *Ab-initio Study of the Properties of TiO2 Rutile and Anatase Polytypes*. PhD thesis, Ecole Polytechnique Fédérale de Lausanne, 2003, 2003.

[CdzS94] M. T. Czyżyk and G. A. Sawatzky. Local-density functional and on-site correlations: The electronic structure of la_2cuo_4 and $lacuo_3$. *Phys. Rev. B*, 49:14211–14228, May 1994.

[CG51] D. C. Cronemeyer and M. A. Gilleo. The optical absorption and photoconductivity of rutile. *Phys. Rev.*, 82:975–976, Jun 1951.

[CHA+06] Eunae Cho, Seungwu Han, Hyo-Shin Ahn, Kwang-Ryeol Lee, Seong Keun Kim, and Cheol Seong Hwang. First-principles study of point defects in rutile Tio_{2-x}. *Phys. Rev. B*, 73:193202, May 2006.

[CK94] Michel Caffarel and Werner Krauth. Exact diagonalization approach to correlated fermions in infinite dimensions: Mott transition and superconductivity. *Phys. Rev. Lett.*, 72:1545–1548, Mar 1994.

[Col03] C. Colinet. Ab-initio calculation of enthalpies of formation of intermetallic compounds and en-

thalpies of mixing of solid solutions. *Intermetallics*, 11(11):1095 – 1102, 2003. Special Issue Dedicated to the International Meeting on "Thermodynamics of Alloys-TOFA 2002.

[Cro52] D. C. Cronemeyer. Electrical and optical properties of rutile single crystals. *Phys. Rev.*, 87:876–886, Sep 1952.

[Czy08] G. Czycholl. *Theoretische Festkoerpphysik - Von den klassischen Modellen zu modernen Forschungsthemen.* New York:Springer–Verlag, 2008.

[DBMP17] Pascal Delange, Silke Biermann, Takashi Miyake, and Leonid Pourovskii. Crystal-field splittings in rare-earth-based hard magnets: An ab initio approach. *Phys. Rev. B*, 96:155132, Oct 2017.

[DBS+98] S.L. Dudarev, G.A. Botton, S. Y. Savrasov, W.M.Temmerman, and A.P.Sutton. 166:429, 1998.

[DLM11] Dat Do, Mal-Soon Lee, and S. D. Mahanti. Effect of onsite coulomb repulsion on thermoelectric properties of full-heusler compounds with pseudogaps. *Phys. Rev. B*, 84:125104, Sep 2011.

[DMC+09] I. DiMarco, J. Minar, S. Chadov, M. I. Katsnelson, H. Ebert, and A. I. Lichtenstein. *Phys.Rev.B*, 79:115111, 2009.

[DRJD02] G. P. Das, B. K. Rao, P. Jena, and S. C. Deevi. Electronic structure of substoichiometric fe-al intermetallics. *Phys. Rev. B*, 66:184203, Nov 2002.

[ERW05] L. A. Errico, M. Rentería, and M. Weissmann. Theoretical study of magnetism in transition-metal-doped Tio_2 and $Tio_{2-\delta}$. *Phys. Rev. B*, 72:184425, Nov 2005.

[FB60] J. M. Foster and S. F. Boys. Canonical configurational interaction procedure. *Rev. Mod. Phys.*, 32:300–302, Apr 1960.

[FW71] A. L. Fetter and J. D. Walecka. *Quantum Theory of Many Particle System.* New York:Springer–Verlag, 1971.

[GM58] V. M. Galitskii and A. B. Migdal. Application of quantum field theory methods to the many body problem. *Soviet Journal of Experimental and Theoretical Physics Letters*, 1:96, 1958.

[GML+11a] E. Gull, A. J. Millis, A. I. Lichtenstein, A. N. Rubtsov, M. Troyer, and P. Werner. Continuous-time Monte Carlo methods for quantum impurity models. *Reviews of Modern Physics*, 83(2):349, 2011.

[GML+11b] E. Gull, A. J. Millis, A. I. Lichtenstein, A. N. Rubtsov, M. Troyer, and P. Werner. Continuous-time monte carlo methods for quantum impurity models. *Rev. Mod. Phys.*, 83:349–404, May 2011.

[GOPS06] Pablo Guillermo Gonzales-Ormeño, Helena Maria Petrilli, and Cláudio Geraldo Schön. Ab initio calculation of the bcc fe–al phase diagram including magnetic interactions. *Scripta Materialia*, 54(7):1271 – 1276, 2006.

[Gri13] D. Grieger. *Charge self-consistency in an LDA+DMFT framework.* PhD thesis, Hamburg, Universitaät Hamburg, 2013.

[Gul08] E. Gull. *Continuous-time quantum Monte Carlo algorithms for fermions.* PhD thesis, ETH ZURICH, 2008.

[Hau07] K. Haule. Quantum Monte Carlo impurity solver for cluster dynamical mean-field theory and electronic structure calculations with adjustable cluster base. *Physical Review B*, 75(15):155113, 2007.

[Hau15] Kristjan Haule. Exact double counting in combining the dynamical mean field theory and the density functional theory. *Phys. Rev. Lett.*, 115:196403, Nov 2015.

[HCNM+17] Bevin Huang, Genevieve Clark, Efren Navarro Moratalla, Dahilia R. Klein, Ran Cheng, Kyle L. Seyler, Ding Zhong, Emma Schmidgall, Michael A. McGuire, David H. Gobden, Wang Yao, Di Xiao, Pablo Jarillo Herrero, and Xiaodong Xu. Layer-dependent ferromagnetism in a van der waals crystal down to the monolayer limit. *Nature*, 546:270–273, 2017.

[Hed65] L. Hedin. New method for calculating the one-particle green's function with application to the electron-gas problem. *Phys. Rev.*, 139:A796–A823, Aug 1965.

[Heu03] Fr. Heusler. Studien über magnetisierbare manganlegierungen. *Verh. Dtsch. Phys. Ges.*, 12(219), 1903.

[HG94] M Henzler and Göpel. *Oberflächenphysik des Festkörpers.* 2nd ed., B.G.Teubner, Stuttgard, 1994.

[HK64] P. Hohenberg and W. Kohn. Inhomogeneous electron gas. *Phys. Rev.*, 136:B864–B871, 1964.

[Hub63] Electron correlations in narrow energy bands. *Proceedings of the Royal Society of London A: Mathematical, Physical and Engineering Sciences*, 276(1365):238–257, 1963.

[IBG07] Mazharul M. Islam, Thomas Bredow, and Andrea Gerson. Electronic properties of oxygen-deficient and aluminum-doped rutile Tio_2 from first principles. *Phys. Rev. B*, 76:045217, Jul 2007.

[imcmcieifbuFB11] Ersoy Şaşıoğlu, Christoph Friedrich, and Stefan Blügel. Effective coulomb interaction in transition metals from constrained random-phase approximation. *Phys. Rev. B*, 83:121101, Mar 2011.

[ISDSAM15] E I. Shreder, A D. Svyazhin, and A A. Makhnev. Evolution of the electronic structure and optical properties of iron-based heusler alloys. 119:969–973, 12 2015.

[JVR+10] A. Janotti, J. B. Varley, P. Rinke, N. Umezawa, G. Kresse, and C. G. Van de Walle. Hybrid functional studies of the oxygen vacancy in tio_2. *Phys. Rev. B*, 81:085212, Feb 2010.

[KHH+06] Yoichi Kamihara, Hidenori Hiramatsu, Masahiro Hirano, Ryuto Kawamura, Hiroshi Yanagi, Toshio Kamiya, and Hideo Hosono. iron-based layered

superconductor: Laofep. *Journal of the American Chemical Society*, 128(31):10012–10013, 2006. PMID: 16881620.

[KNMA00] M. Kato, Y. Nishino, U. Mizutani, and S. Asano. Electronic, magnetic and transport properties of (fe 1- x v x) 3 al alloys. *Journal of Physics: Condensed Matter*, 12(8):1769, 2000.

[KO97] L. Kihlborg and I. Olovsson. Arne Magnéli, 1914–1996. *Acta Crystallographica Section A*, 53(2):103–104, Mar 1997.

[Kof67] P. Kofstad. Note on the defect structure of rutile (tio2). *Journal of the Less Common Metals*, 13(6):635 – 638, 1967.

[Kof72] P. Kofstad. *Nonstoichiometry, diffusion, and electrical conductivity in binary metal oxides / Per Kofstad.* New York (N.Y.) : Wiley-Interscience, 1972.

[KRPS02] Wei Ku, H. Rosner, W. E. Pickett, and R. T. Scalettar. Insulating ferromagnetism in $la_4ba_2cu_2o_{10}$: An ab initio wannier function analysis. *Phys. Rev. Lett.*, 89:167204, Sep 2002.

[KS65] W. Kohn and L. J. Sham. Self-consistent equations including exchange and correlation effects. *Phys. Rev.*, 140:A1133–A1138, 1965.

[KSH+06] G. Kotliar, S. Y. Savrasov, K. Haule, V. S. Oudovenko, O. Parcollet, and C. A. Marianetti. Electronic structure calculations with dynamical mean-field theory. *Reviews of Modern Physics*, 78(3):865, 2006.

[KUW+10] M. Karolak, G. Ulm, T. Wehling, V. Mazurenko, A. Poteryaev, and A. I. Lichtenstein. Double counting in lda+dmft—the example of nio. *Journal of Electron Spectroscopy and Related Phenomena*, 181(1):11 – 15, 2010. Proceedings of International Workshop on Strong Correlations and Angle-Resolved Photoemission Spectroscopy 2009.

[KWHH08] Yoichi Kamihara, Takumi Watanabe, Masahiro Hirano, and Hideo Hosono. iron-based layered superconductor la[o$_{1-x}$f$_x$]feas (x = 0.05 - 0.12) with tc = 26 k. *Journal of the American Chemical Society*, 130(11):3296–3297, 2008. PMID: 18293989.

[LFS05] F. Lechermann, M. Fähnle, and J.M. Sanchez. First-principles investigation of the ni–fe–al system. *Intermetallics*, 13(10):1096 – 1109, 2005.

[LGP+06] F. Lechermann, A. Georges, A. Poteryaev, S. Biermann, M. Posternak, A. Yamasaki, and O. K. Andersen. *Phys.Rev.B*, 74:125120, 2006.

[LK98] A. I. Lichtenstein and M. I. Katsnelson. Ab initio calculations of quasiparticle band structure in correlated systems: Lda++ approach. *Phys. Rev. B*, 57:6884–6895, 1998.

[LR98] Chin-Shan Lue and Joseph H. Ross. Semimetallic behavior in fe$_2$VAl : nmr evidence. *Phys. Rev. B*, 58:9763–9766, Oct 1998.

[LWE+02] F. Lechermann, F. Welsch, C. Elsässer, C. Ederer, M. Fähnle, J. M. Sanchez, and B. Meyer. Density-functional study of fe$_3$Al : lsda versus gga. *Phys. Rev. B*, 65:132104, Mar 2002.

[MDTS91] C.G. McKamey, J.H. DeVan, P.F. Tortorelli, and V.K. Sikka. A review of recent developments in fe3al-based alloys. *Journal of Materials Research*, 6(8):1779–1805, 1991.

[MELFed] B. Meyer, C. Elsässer, F. Lechermann, and M. Fähnle. *FORTRAN 90 Program for Mixed-Basis-Pseudopotential Calculations for Crystals*. Max-Planck-Institut für Metallforschung, Stuttgart, unpublished.

[MV97] N. Marzari and D. Vanderbilt. Maximally localized generalized Wannier functions for composite energy bands. *Physical review B*, 56(20):12847, 1997.

[MYL+08] Arash A. Mostofi, Jonathan R. Yates, Young-Su Lee, Ivo Souza, David Vanderbilt, and Nicola Marzari. wannier90: A tool for obtaining maximally-localised wannier functions. *Computer Physics Communications*, 178(9):685 – 699, 2008.

[NKA+97] Y. Nishino, M. Kato, S. Asano, K. Soda, M. Hayasaki, and U. Mizutani. Semiconductor-like behavior of electrical resistivity in heusler-type fe_2VAl compound. *Phys. Rev. Lett.*, 79:1909–1912, Sep 1997.

[NTY+05] T. Nakama, Y. Takaesu, K. Yagasaki, T Naka, A. Matsushita, K. Fukuda, and Y. Yamada. Transport properties of heusler compounds fe3-xvxal. *Journal of the Physical Society of Japan*, 74(5):1378–1381, 2005.

[OKN+00] H. Okamura, J. Kawahara, T. Nanba, S. Kimura, K. Soda, U. Mizutani, Y. Nishino, M. Kato,

I. Shimoyama, H. Miura, K. Fukui, K. Nakagawa, H. Nakagawa, and T. Kinoshita. Pseudogap formation in the intermetallic compounds $(\mathrm{fe}_{1-x}V_x)_3\mathrm{Al}$. *Phys. Rev. Lett.*, 84:3674–3677, Apr 2000.

[PABG07] L. V. Pourovskii, B. Amadon, S. Biermann, and A. Georges. *Phys.Rev.B*, 76:235101, 2007.

[PBP+04] E. Pavarini, S. Biermann, A. Poteryaev, A. I. Lichtenstein, A. Georges, and O. K. Andersen. Mott transition and suppression of orbital fluctuations in orthorhombic $3d^1$ perovskites. *Phys. Rev. Lett.*, 92:176403, Apr 2004.

[PCM78] J. Pascual, J. Camassel, and H. Mathieu. Fine structure in the intrinsic absorption edge of tio_2. *Phys. Rev. B*, 18:5606–5614, Nov 1978.

[PFA+15] O. Parcollet, M. Ferrero, T. Ayral, H. Hafermann, I. Krivenko, L. Messio, and P. Seth. Triqs: A toolbox for research on interacting quantum systems. *Computer Physics Communications*, 196:398–415, 2015.

[RD02] B.V Reddy and S.C Deevi. Local interactions of carbon in feal alloys. *Materials Science and Engineering: A*, 329-331:395 – 401, 2002.

[RL04] A. N. Rubtsov and A. I. Lichtenstein. Continuous-time quantum monte carlo method for fermions: Beyond auxiliary field framework. *Journal of Experimental and Theoretical Physics Letters*, 80(1):61–65, Ju 2004.

[SKA01] S. Y Savrasov, G. Kotliar, and E Abrahams. Correlated electrons in plutonium within a dynamical mean-field picture. *Nature*, 410:793–795, 2001.

[SKFP16] P. Seth, I. Krivenko, M. Ferrero, and O. Parcollet. Triqs/cthyb: A continuous-time quantum monte carlo hybridisation expansion solver for quantum impurity problems. *Computer Physics Communications*, 200:274 – 284, 2016.

[SM98] D. J. Singh and I. I. Mazin. Electronic structure, local moments, and transport in fe_2VAl. *Phys. Rev. B*, 57:14352–14356, Jun 1998.

[SSJ05] A. V. Smirnov, W. A. Shelton, and D. D. Johnson. Importance of thermal disorder on the properties of alloys: Origin of paramagnetism and structural anomalies in bcc-based $fe_{1-x}al_x$. *Phys. Rev. B*, 71:064408, Feb 2005.

[SSSR71] E. J. Samuelsen, R. Silberglitt, G. Shirane, and J. P. Remeika. Spin Waves in Ferromagnetic $CrBr_3$ Studied by Inelastic Neutron Scattering. *Phys. Rev. B*, 3:157–166, jan 1971.

[STL+01] R. Schaub, P. Thostrup, N. Lopez, E. Lægsgaard, I. Stensgaard, J. K. Nørskov, and F. Besenbacher. Oxygen vacancies as active sites for water dissociation on rutile $tio_2(110)$. *Phys. Rev. Lett.*, 87:266104, Dec 2001.

[Tan03] H. Tang. *Electronic properties of anatase TiO2 investigated by electrical and optical measurements on single crystals and thin films*. PhD thesis, Ecole polytechnique fédérale de Lausanne EPFL, Lausanne (1994), 2003.

[vSKF06] M. van Schilfgaarde, T. Kotani, and S. Faleev. Quasiparticle self-consistent *gw* theory. *Phys. Rev. Lett.*, 96:226402, Jun 2006.

[WCD+06] P. Werner, A. Comanac, L. De'Medici, M. Troyer, and A. J. Millis. Continuous-time solver for quantum impurity models. *Physical Review Letters*, 97(7):076405, 2006.

[WM06] P. Werner and A. J. Millis. Hybridization expansion impurity solver: General formulation and application to Kondo lattice and two-orbital models. *Physical Review B*, 74(15):155107, 2006.

[WP98] Ruben Weht and W. E. Pickett. Excitonic correlations in the intermetallic fe_2VAl. *Phys. Rev. B*, 58:6855–6861, Sep 1998.

[ZQZL15] Wei-Bing Zhang, Qian Qu, Peng Zhu, and Chi-Hang Lam. Robust intrinsic ferromagnetism and half semiconductivity in stable two-dimensional single-layer chromium trihalides. *J. Mater. Chem. C*, 3:12457–12468, 2015.

Eidesstattliche Versicherung

Hiermit versichere ich an Eides statt, die vorliegende Dissertationsschrift selbst verfasst und keine anderen als die angegebenen Hilfsmittel und Quellen benutzt zu haben.

Die eingereichte schriftliche Fassung entspricht der auf dem elektronischen Speichermedium.

Die Dissertation wurde in der vorgelegten oder einer ähnlichen Form nicht schon einmal in einem früheren Promotionsverfahren angenommen oder als ungenügend beurteilt.

Unterschrift:

Datum:

Danksagung/Acknowledgments

First of all I'd like to thank my supervisor, Prof. Alexander Lichtenstein, for giving me the opportunity to study and work in his group and to complete this thesis. I'd like to thank Frank Lechermann for many valuable discussions and scientific input.

I thank PD. Dr. Alexander Chudnovskiy for acting as the second referee of the written dissertation.

I'd like to thank Mikhail Katsnelson for their support and discussions on $CrBr_3$ who contributed physical insight from their far reaching experience with quantum magnetism.

I'd like to thank Frau Ramakers for proofreading parts of this thesis.

Mein Dank gilt der Universität Hamburg und der Deutschen Forschungsgemeinschaft für die finanzielle Unterstützung meiner Dissertationszeit und auch für die Veranstaltung mehrerer Herbstschulen, Klausurtagungen und Konferenzen. Ich danke dem Norddeutschen Verbund für Hoch- und Höchstleistungsrechner (HLRN) für das Bereitstellen der erheblichen Rechenkapazitäten, ohne die ein Großteil der numerischen Arbeit nicht hätte stattfinden können.

Recht herzlich bedanke Ich mich bei meinen Kommilitonen und anderen Mitarbeiter der Arbeitsgruppe in Hamburg, allen voran Viktor Valmispild. Es war mir eine Ehre, mit dir zusammen zu arbeiten. Ich danke Friedrich Krien, Arthur Huber, Roberto Mozara und Sergej Brener für eine wertvolle Arbeitsumgebung und vieles Persönliches darüber hinaus. Außerdem danke ich Daniel Hirschmeier, Burkhard

Sachs,Patryk Kubiczek, Yusuf Mohamed, Maria Valentyuk, Malte Harland und Igor Krivenko für die verschiedensten physikalischen und nicht physikalischen Diskussionen.

Ich danke Bodo Krause-Kyora und Michael Vedmedenko dafür, dass immer alles funktioniert hat technisch oder schnell funktionierend gemacht wurde.

Ganz besonders danke ich natürlich meinen Eltern, die mir das Studium erst ermöglichten und mich jederzeit unterstützten, sowie meiner Schwester, die meiner Arbeit viel Verständnis und Geduld entgegenbrachte.

Am meisten danke ich natürlich meiner Frau, Anna, die mich immer unterstützt hat.